University of Oklahoma

Graduate College

J/ψ meson production in association with a $W^{\pm}$ boson: Cross section ratio measurement with the ATLAS detector using $\sqrt{s}$=8 TeV pp data from the Large Hadron Collider at CERN

A Dissertation

Submitted to the Graduate Faculty

in partial fulfillment of the requirements for the

degree of

Doctor of Philosophy

By

DAVID BERTSCHE
Norman, Oklahoma
2016

J/ψ MESON PRODUCTION IN ASSOCIATION WITH A $W^{\pm}$ BOSON: CROSS SECTION RATIO MEASUREMENT WITH THE ATLAS DETECTOR USING $\sqrt{s}$=8 TeV pp DATA FROM THE LARGE HADRON COLLIDER AT CERN

A DISSERTATION APPROVED FOR THE
HOMER L. DODGE DEPARTMENT OF PHYSICS AND ASTRONOMY

BY

Dr. Braden Abbott, Chair

Dr. Paula Conlon

Dr. Michael Strauss

Dr. Howard Baer

Dr. Michael Santos

“I do not know what I may appear to the world, but to myself I seem to have been only like a boy playing on the seashore, and diverting myself in now and then finding a smoother pebble or a prettier shell than ordinary, whilst the great ocean of truth lay all undiscovered before me.”

★

Sir Isaac Newton (1642–1727)

Acknowledgements

I would like to acknowledge the US Department of Energy for funding this work.

Table of Contents

List of Tables

List of Figures

Abstract

The production mechanism of charmonium particles in hadronic collisions is not fully understood and is an active area of research. These mechanisms can be studied by examining the associated production of charmonium particles in association with vector bosons particles. This thesis examines the associated production of J/ψ mesons (the charmonium particle) along with $W^{\pm}$ boson particles using 20.3 fb^{-1} of data collected using the ATLAS detector at CERN's Large Hadron Collider (LHC) accelerator from $proton - proton$ collisions at center of mass energy $\sqrt{s} = 8$ TeV. A measurement of the prompt $J/\psi + W^{\pm}$ production rate as a ratio to the inclusive $W^{\pm}$ production rate is made and the results used to provide some insights into the double parton scattering processes.

Chapter 1

Introduction and Theoretical Background

Colloquially, particle physics addresses the questions “What is everything made of and what keeps it together?” It is the modern incarnation of the ancient search for the ultimate constituent of matter begun by the Greeks, who coined the word $a - tom$, meaning indivisible [1]. We now know that atoms are in fact divisible and are made of smaller components, such as the protons and neutrons, which are themselves divisible into even smaller components called quarks. The particles that are currently understood as the ultimate constituents of matter are contained in what is called the Standard Model of Particle Physics [2, 3, 4]. But if history is any guide we may find that these ‘elementary’ particles are not so elementary after all.

The second question more broadly deals with all interactions between matter. The four known interactions, or forces, are $strong, weak, electromagnetic$ and $gravitational$. Each force has an associated particle and quantum field. The first three are contained within the Standard Model, while gravity is not. A successful theory of quantum gravity has yet to be formulated [5].

1.1 The Standard Model

The Standard Model is a way to describe the fundamental particles and forces of the universe; its development was contributed to by many physicists throughout the world during the 20th century. It predicts the existence and describes the attributes of 17 fundamental particles, all of which have now been observed. It is known to be incomplete, since it does not explain certain experimental observations, such as gravity, dark matter, and the asymmetry between matter and anti-matter. Much work is currently being undertaken by both theoretical and experimental physicists to expand the model.

The Standard Model is built on three principles of physics: relativity, quantum mechanics and gauge invariance. The last of the three, gauge invariance, is central to particle physics because it ensures that the amplitudes in perturbation expansions are renormalizable. In other words, that the calculated observables are finite and thus physical [6].

This section discusses the particles described by the Standard Model and the mathematical formalisms used to describe and predict their properties and behaviour. A more detailed discussion of the two particles that are the subject of this dissertation follows, namely the J/ψ meson and the $W^{\pm}$ boson.

1.1.1 Standard Model particles

The fundamental particles of the Standard Model are shown in Figure 1.1. They are divided into two types, fermions and bosons. The fermions constitute matter and bosons mediate the forces and interactions between this matter. The fermions are further divided into three generations. The first fermion generation (save neutrinos) constitutes everyday matter, and the photon boson mediates *light* and *electromagnetism*. So these four fundamental particles (up and down quarks, electron and photon) are responsible for the bulk of everyday human experience.

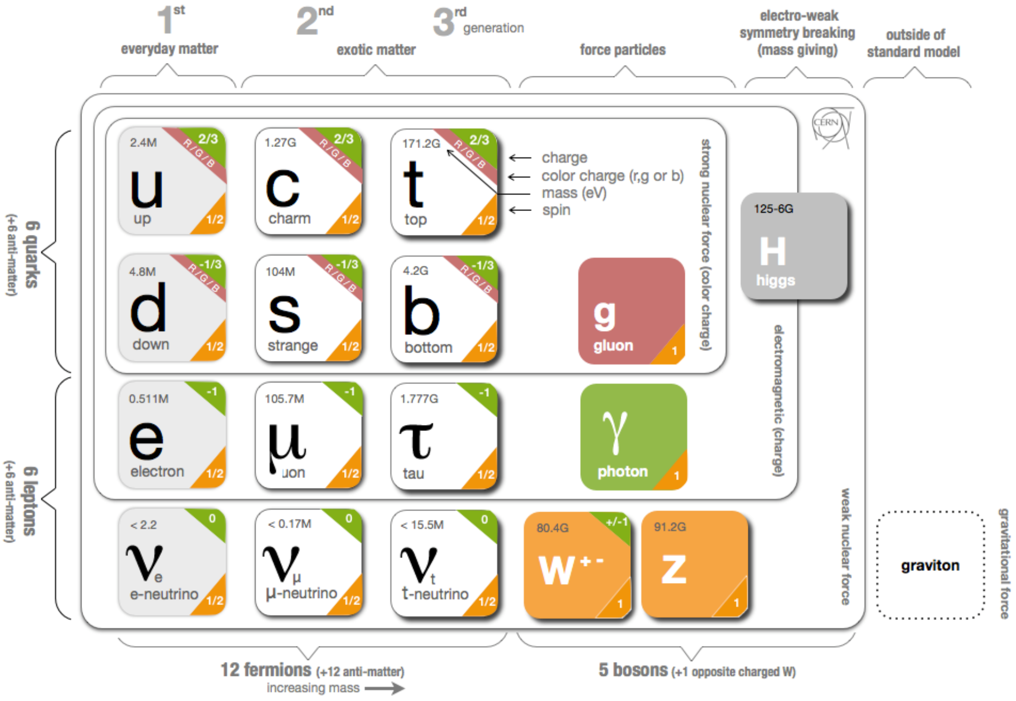

Figure 1.1: The Standard Model of Particle Physics. The matter particles (fermions) are further divided into two groups called quarks and leptons. The force carrying particles are known as bosons.

The second and third generation fermions are heavier copies of the first generation. They can be found in nature as the result of high energy cosmic rays arriving to earth from space and from other processes. But in practice they are produced by particle accelerator experiments in order to be studied in laboratories. There are various experiments set up around to world that detect them. Another way to study these particles is to create them artificially in a laboratory with the use of high energy particle accelerators. The gluon boson mediates the *strong* force, which holds quarks together to form composite particles (such as protons and neutrons). The $W^{\pm}$ and Z^0 bosons mediate the *weak* force, which is responsible for some radioactive decays. The Higgs boson mediates the interaction that gives mass to all particles. The hypothetical graviton mediates the *gravitational* force and has not been observed.

1.1.2 Group Theory formalism of the Standard Model

The Standard Model is comprised of three distinct particle type sectors that contain: spin-one gauge bosons, spin-one-half fermions, and a spin-zero boson[1]. The first sector is responsible for particles that mediate the interactions between all particles and can be written symbolically using group theory notation as:

$$SU(3)_C \otimes [SU(2)_L \otimes U(1)_Y] \tag{1.1}$$

The $SU(3)_C$ group is a symmetry of the *strong* interaction; the $_C$ means that the strong force mediators (known as gluons) only couple to particles with color charge (i.e. quarks and gluons). The $SU(2)_L \times U(1)_Y$ part represents the unified *electroweak* interaction; the $_L$ means that the $SU(2)_L$ group only couples to left hand particles with weak isospin and the $_Y$ means that the $U(1)_Y$ only couples to particles with hypercharge (more on this follows). These interactions are mediated by the massive $W^{\pm}$ and Z^0 bosons (for the *weak* force part) and the massless photon (for the *electromagnetic* force part).

The second sector contains the particles that compose matter. Each of the generations discussed before and shown in Figure 1.1 can be divided into five multiplets.

---

[1] The third particle sector potentially contains multiple spin-zero bosons.

Table 1.1: The five multiplets of the first generation of fermions. r, g, b are the red, green and blue color charges. L and R are the left or right handed particle spin states. Electric charge (Q) is the familliar fundamental quantum number and the multiplet hypercharge (Y) is calculated from Q.

Multiplet	States	Y	Q
Left-handed quarks	$\begin{pmatrix} u^r\ u^g\ u^b \\ d^r\ d^g\ d^b \end{pmatrix}_L$	$+\frac{1}{3}$	$+\frac{2}{3}$ $-\frac{1}{3}$
Right-handed up quarks	$\left(u^r\ u^g\ u^b\right)_R$	$+\frac{4}{3}$	$+\frac{2}{3}$
Right-handed down quarks	$\left(d^r\ d^g\ d^b\right)_R$	$-\frac{2}{3}$	$-\frac{1}{3}$
Left-handed leptons	$\begin{pmatrix} \nu \\ e \end{pmatrix}_L$	-1	0 -1
Right-handed electron	e_R	-2	-1

These multiplet groupings are made according to the charges they carry. The three strong or color charges are *red*, *green* and *blue*; the two weak charges are *up* and *down*. These are analogous to the more familiar electromagnetic charges of *positive* and *negative*. The multiplet hypercharge is calculated by taking twice the average of the electric charges of all the particles in the multiplet. The multiplets of the first generation fermions are shown in Table 1.1.

The first multiplet contains an SU(3) 'triplet' of spin left-handed quarks in one of six states of color and weak charge. The second and third multiplets contain right-handed quarks of three color charges. Those do not feel the weak (i.e. $SU(2)_L$)

interaction since it is felt only by left-handed particles. The fourth multiplet contains the color-chargeless left-handed lepton ‘doublet’. Not having a color charge means it does not feel the strong interaction. However it does feel the weak interaction with the ‘up’ weak charge carried by the neutrino and the ‘down’ weak charge by the electron. The fifth multiplet contains a right-handed electron ‘singlet’ that does not feel the weak or strong interaction.

The third particle type sector contains only the spinless Higgs boson, which gives mass to all particles as a byproduct of spontaneous electroweak symmetry breaking.

1.1.3 Lagrangian formalism of the Standard Model

The equations of motion of a dynamic mechanical system can be derived from the Lagrangian function [7]. For the case of quantum fields it can be generically written down as:

$$L(t) = \int \mathcal{L} d^3x \tag{1.2}$$

In particle physics we deal more frequently with the Lagrangian density function $\mathcal{L}$, and often refer to it directly as the Lagrangian. These equations are used to calculate the particle scattering and decay rates from the interactions of particles.

As an example we look at an equation describing the *electromagnetic* interaction, which is part of the theory of quantum electrodynamics (QED). QED was the first part of the Standard Model to be mathematically formulated and it is the simplest [6]. For a massless electromagnetic field A_μ interacting with a spin-$\frac{1}{2}$ field ψ of bare mass

m the QED Lagrangian is:

$$\mathcal{L} = -\frac{1}{4}F_{\mu\nu}F^{\mu\nu} + \bar{\psi}(i\gamma^{\mu}D_{\mu} - m)\psi \tag{1.3}$$

The electromagnetic field field tensor is given by

$$F_{\mu\nu} = \partial_{\mu}A_{\nu} - \partial_{\nu}A_{\mu} \tag{1.4}$$

and the covariant derivative is

$$D_{\mu} = \partial_{\mu} + ieA_{\mu}Q \tag{1.5}$$

where the unit of electric charge is e and Q[2] is the charge operator. A Lagrangian representation of the full Standard Model, including an explanation of all the terms, can be found in Reference [8].

1.1.4 Summary

In summary, the Standard Model contains 17 fundamental particles based on their mass value and interaction type. However, if one considers a differing spin-handedness and charge color to result in a fundamentally different particle, then the number rises. In addition, for each fermion particle there exists a corresponding anti-particle. These anti-particles have identical mass but opposite spin-handedness, color and electric charges (where applicable) to their particles. So if one considers anti-particles to be fundamentally different particles then the total number of fundamental particles rises even further [1, 5].

---

[2] e.g. for an electron: $Q\psi = -\psi$

1.2 J/ψ particle

When a quark and anti-quark form a bound state with each other they create a composite particle called a meson. A particle formed by a bound state of a quark and its anti-quark is known as quarkonium. The charm and anti-charm ($c\bar{c}$) combination is known as charmonium. Many charmonia states exist and are differentiated by their properties such as mass and spin. The J/ψ meson is an electrically neutral charmonium particle with mass 3.1 GeV, spin 1, orbital angular momentum 0 and odd charge conjunction and parity [9]. The formation of these heavy quarkonium (such as the J/ψ) can be explained using the effective field theory model of nonrelativistic quantum chromodynamics (NRQCD) [10].

J/ψ can decay both hadronically and leptonically. A useful property for making measurements is that almost 12% of J/ψ particles will decay into a pair of oppositely charged electrons or muons. This then results in a very clean and readily identifiable experimental signature [9].

Two experiments independently discovered the J/ψ particle in November 1974 and thus firmly established the quark model as the primary theoretical description of fundamental particles. The group using an electron-positron accelerator and the SPEAR detector at Stanford Linear Accelerator observed a very sharp peak at 3.1 GeV in the decay of this new particle to hadrons and to e^+e^-, with a possible additional signature to $\mu^+\mu^-$ [11]. The group using the AGS experiment at Brookhaven National Lab collided protons into Beryllium nuclei and then measured the e^+e^- mass spectrum with a precise pair spectrometer. They also observed a sharp e^+e^- invariant mass

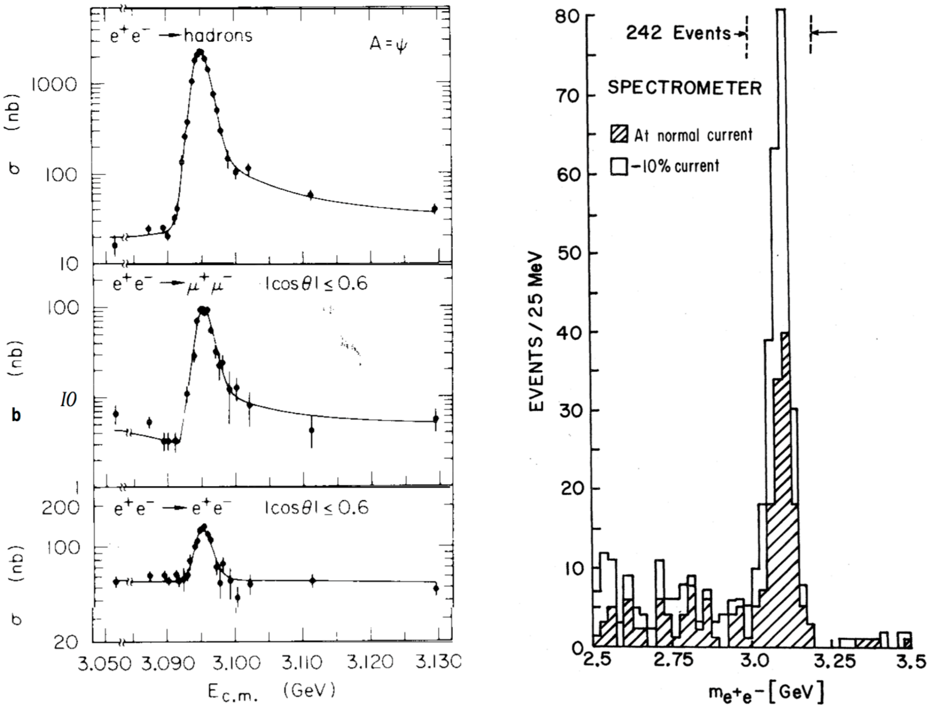

(a) (b)

Figure 1.2: J/ψ particle discovery data from the SPEAR (a) and AGS (b) experiments both showing oppositely charged dielectron mass peaks consistent with a J/ψ at 3.1 GeV.

peak at 3.1 GeV [12].

This discovery of a particle containing the charm quark began the confirmation of the six quark model that was proposed by Kobayashi and Maskawa [13] as an extension to the four quark model originally proposed by Cabibbo [14]. Its discovery implied the existence of many other 'charmed' composite particles that could exist in various excited states. This spurred a busy time of particle physicists competing against each other to discover these new particles and to determine their properties. This work led to much development in the understanding of the strong force between quarks, the sub-branch of particle physics known as Quantum Chromodynamics (QCD) [5].

All six quarks were eventually observed with the discovery of the bottom quark in 1977 at Fermilab [15] and with the discovery of the top quark in 1995 by the CDF and DØ experiments [16, 17].

1.3 $W^{\pm}$ particle

It became clear to theorists that there must be intermediate vector bosons to carry the weak interaction and by the 1970s experimentalists had begun enormous efforts to detect them. Theory predicted and gave approximate masses for two charged bosons ($W^{\pm}$) and one neutral boson (Z^0) so experimentalists set up their equipment with these predictions in mind. In 1983 the discovery of these particles was announced by experiments at the super proton synchrotron (SPS), a $p\bar{p}$ collider at CERN [5].

The $W^{\pm}$ boson particle was verified to have a charge of either +1 or -1, a mass of 80.4 GeV and spin 1. The majority of the time it decays into hadrons and 10.6% of the time it decays into a muon and a neutrino. $W^{\pm}$ bosons are too short lived to be detected directly and their presence must be inferred from their decay products [9].

This discovery was the culmination of many successful experiments that verified the Glashow–Weinberg–Salam electroweak model [5]. Ongoing tests probing the internal consistency of the Standard Model have been greatly aided by making precision measurements of the $W^{\pm}$ boson mass [9].

1.4 Higgs particle discovery

In July 2012 the discovery of the final missing piece of the Standard Model, the Higgs boson, was announced by the ATLAS [18] and CMS [19] collaborations at CERN. Its mass turned out to be approximately 125 GeV. This was a tremendous experimental achievement and the validation of a half century of theoretical work [5].

Chapter 2

Experimental Setup

The data used for this dissertation were gathered from proton-proton collisions by the ATLAS detector at the European Organization for Nuclear Research (CERN), located near Geneva, Switzerland. CERN hosts a large accelerator complex with many experimental areas, as seen in Figure 2.1. The Large Hadron Collider (LHC) is the largest accelerator in the complex, and ATLAS the largest experiment. The LHC gives 'bunches' of protons enormous amounts of kinetic energy, forming them into 'beams', and then directing them into head on collisions with each other. This energy is then available for spontaneous conversion into different types of particles, which are then 'photographed' by the ATLAS detector.

2.1 The Large Hadron Collider

The LHC is the most powerful and one of the newest tools in the world for particle physics research. It occupies a roughly circular tunnel 26.7 km in diameter and between 45 m and 170 m underground. The tunnel has eight straight sections connected by eight circular arcs and was originally constructed to hold the large electron-positron (LEP) accelerator. LEP was decommissioned in 2000 and the LHC first started operations in 2008. The information in this section is summarized primarily from reference [20], with any additional references noted where relevant.

The LHC is able to take advantage of other accelerating infrastructure already built

Figure 2.1: The accelerator complex at CERN. The protons used in this experiment begin at LINAC 2 and are accelerated using the Booster, the PS, the SPS and the LHC before colliding together in ATLAS. There are four main experimental caverns around the LHC tunnel to house the four main experiments (or detectors), namely, ALICE, CMS, LHCb and ATLAS.

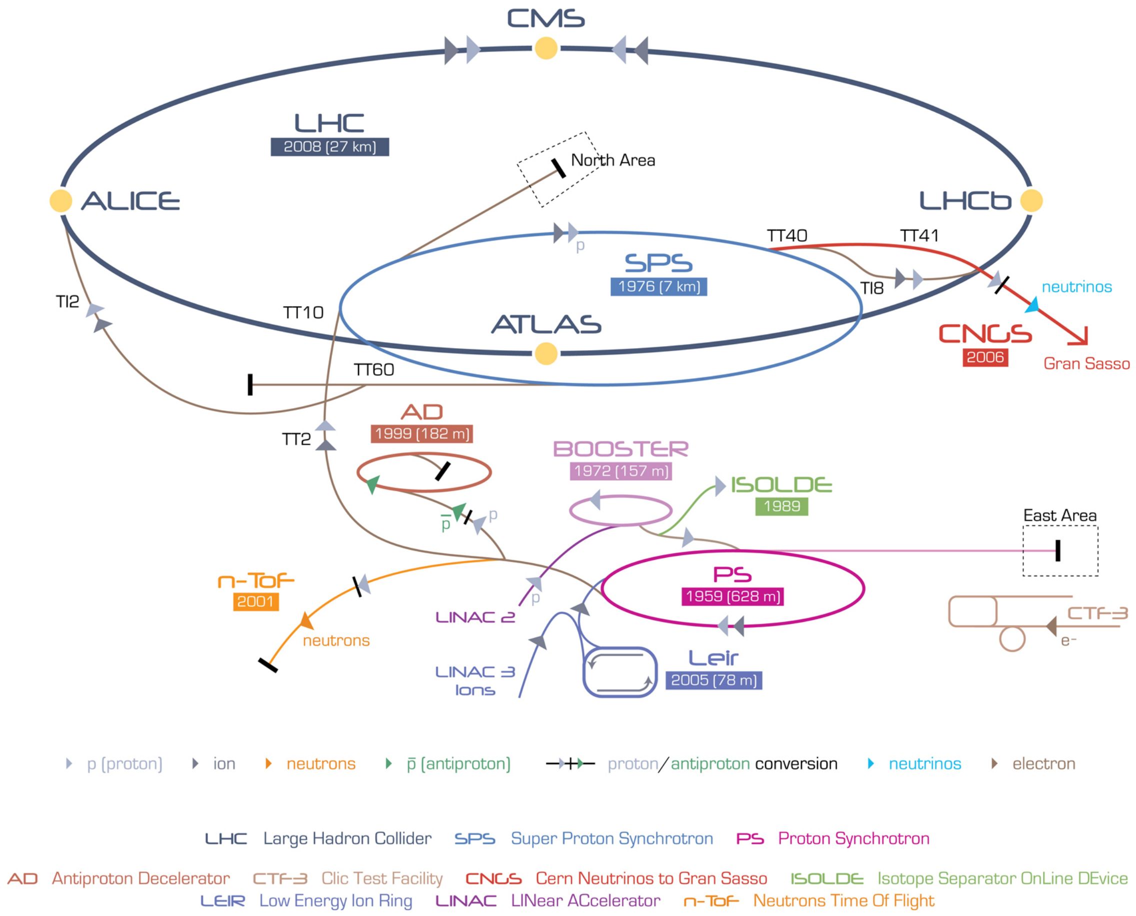

at CERN over previous decades. This provides an injector chain of Linac2 – Proton Synchrotron Booster (PSB) – Proton Synchrotron (PS) – Super Proton Synchrotron (SPS), as shown in Figure 2.1. Beams are injected into the LHC from the preexisting infrastructure at Points 2 and 8 using an injection kicker system. To carry protons in opposite directions around the tunnel, two beam pipes must be used with the magnetic field in each beam pipe pointing in the opposite direction to the other. (In contrast a *proton – antiproton* accelerator can function with only a single beam pipe.) However it would have been extremely difficult to install two magnet rings side by side in the existing LEP tunnel. So a twin-bore magnet design was adopted requiring only one magnet ring to be installed.

2.1.1 Performance

To make new discoveries in high energy particle physics the goal is to generate the largest number of events (or proton-proton collisions) possible per second at the highest possible energy. This is directly related to a quantity called accelerator luminosity by:

$$N_{\text{event}} = L\sigma_{\text{event}} \tag{2.1}$$

where N_{event} is the number of events per second, L is the accelerator luminosity and σ_{event} is the cross section[1] for a given event. Accelerator luminosity for a Gaussian beam distribution is given by:

$$L = \frac{N_b^2 n_b f_{\text{rev}} \gamma_r}{4\pi\epsilon_n\beta^*} F \tag{2.2}$$

---

[1] Cross section is related to the probability that a given event will occur

where N_b is the number of particles per bunch, n_b is the number of bunches per beam, f_{rev} the revolution frequency, γ_r the relativistic gamma factor, ϵ_n the normalized transverse beam emittance[2], β^* the beta star function[3] at the collision point, and F the geometric luminosity reduction factor due to the interaction point (IP) crossing angle:

$$F = \left(1 + \left(\frac{\theta_c \sigma_z}{2\sigma^*}\right)^2\right)^{-\frac{1}{2}} \tag{2.3}$$

θ_c is the full crossing angle at the IP, σ_z the RMS bunch length and σ^* the transverse RMS beam size at the IP. The goal is to maximize beam luminosity by controlling these parameters. For ATLAS the LHC has a peak design luminosity of $L = 10^{34}$ cm^{-2}s^{-1} for proton-proton collisions.

A higher beam energy means more massive particles can be produced in collisions and in general a greater number of particles can be produced per collision. The LHC was designed for proton-proton center of mass energy of 14 TeV.[4]

2.1.2 Operation

The circulating proton beams are each divided into 2,808 bunches of protons with a nominal bunch spacing of 25 ns. Each bunch contains 1.15×10^{11} protons. At maximum energy the dipole magnets (which bend the beams around the ring) must be at a peak magnetic field strength of 8.33 T. This required the development of specialized superconducting magnet technology. The total energy stored in the magnet

---

[2] Emittance characterizes the quality of the beam, it is invariant around the LHC.

[3] The beta star function is a property of the magnet settings at a given point around the LHC and it characterizes the beam envelope.

[4] $1eV = 1.602 \times 10^{-19} J$

system and circulating beams is more than 1 GJ. This energy must be safely and quickly absorbed at the end of each run, especially when the run ends due to a malfunction or emergency.

During normal LHC operations, the luminosity will decay over time, primarily due to beam loss from collisions. The net estimated luminosity lifetime is

$$\tau_L = 14.9\,\text{hours} \tag{2.4}$$

and the LHC is designed to have a usable beam circulating for about 100 hours. After the luminosity drops below the level needed to efficiently collect physics data, the run is ended, the beam is 'dumped' and the LHC magnets are ramped down to a level corresponding to 450 GeV. On average it takes seven hours to re-inject beams into the LHC and bring them back up to full energy.

The integrated luminosity of one run is calculated as

$$L_{int} = L_0 \tau_L \left[1 - e^{-\frac{T_{run}}{\tau_L}}\right] \tag{2.5}$$

where T_{run} is the length of the run. It is measured in units of 'inverse barns'[5] and its value directly corresponds to the amount of data that was collected during that run. The LHC design can theoretically deliver between 80 to 120 fb^{-1} of integrated luminosity per year.

2.1.3 Magnets

The LHC uses superconducting electro-magnets that are at the leading edge of currently available technology. An enormous amount of current is needed in order to generate

---

[5] A barn is a unit of area where 1 b = 10^{28} m^2.

the necessary fields in excess of 8 T. This current would melt conventional cables; NbTi Rutherford cables are cooled with liquid helium to 1.9 K, decreasing their electrical resistance to zero.

Due to space limitations in the LHC tunnel, a two-in-one design with two beam pipes in one magnet as shown in Figure 2.2. The stresses caused by the large opposing magnetic fields in close proximity necessitate a mechanical strength much greater than in previous magnet designs.

2.1.4 Acceleration

Proton beams are injected into the LHC at 450 GeV and are accelerated to a maximum of 7 TeV using a superconducting 400 MHz radio frequency (RF) cavity system, which is located at only one area on the ring (Point 4). This type of system has been used on many previous accelerators and is well understood from an engineering perspective.

2.1.5 Vacuum System

There are three vacuum systems on the LHC: two insulation vacuums (for the cryomagnets and helium distribution) and the beam vacuum. The beam vacuum has the most stringent requirements of the three and is required to be between 10^{-10} and 10^{-11} mbar. While the insulation vacuums need only to be 10^{-1} mbar.

2.1.6 Powering and protection

The LHC has 1,612 different electrical circuits with 3,286 current leads in total for powering the superconducting and normal conducting magnets. The magnets are

Figure 2.2: LHC dipole magnet cross-section showing the two-in-one beam pipe design. The majority of the LHC is composed of this type of magnet, which bend the particle beams around the 26.7 km ring. In certain areas other types of magnets are used for specialized tasks such as beam focusing or injection. (Measurements marked in mm.)

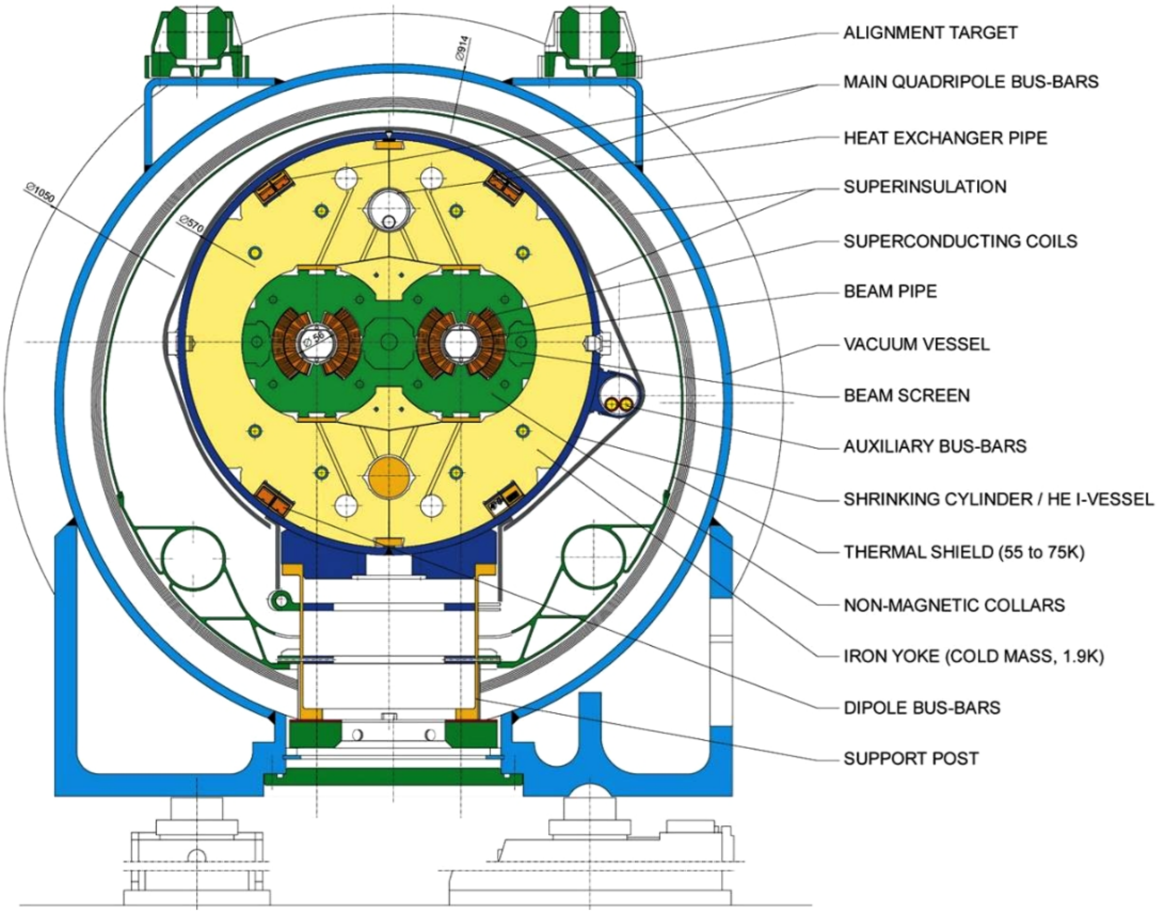

grouped into sections that do not extend over more than one LHC sector, with each having an independent power supply system. This limits the total amount of energy stored in any one continuous section of magnets in the LHC. In the event of a malfunction requiring a rapid energy extraction (quench) this limits the potential for damage. However, the energy stored is still enough to cause significant damage, so it is essential to have a sophisticated protection system. If the protection system is activated the energy stored in the magnets is redirected to a series of resistors called quench heaters, which are located at the surface level. These heat up to 350°C to safely dissipate the energy.

2.1.7 Cryogenic system

To maximize the magnetic field strength of the NbTi windings of the superconducting magnets of the LHC, they are operated at a temperature equal to or below 1.9K. In order to achieve this the 'cold mass' of the LHC, which includes the superconducting magnet windings, are immersed in a pressurized bath of superfluid helium at about 0.13 MPa and maximum temperature of 1.9K. The cold mass comprises 37×10^6 kg and takes up to 15 days to fill and cool with helium.

There were some constraints put on the design and implementation of the cryogenic system by the decision to reuse as much of the existing LEP infrastructure as possible. The LHC has the world's most powerful helium refrigeration system; significant R&D was performed by CERN prior to eight 1.8 K refrigeration units being procured industrially.

2.1.8 Beam instrumentation

The LHC is designed to have a maximum bunch crossing frequency of 40 MHz, or one crossing every 25 ns. The colliding beams are designed to cross at an angle of 150-200 μrad in order to reduce unwanted ‘parasitic’ collisions near the interaction point.

The position and size of the LHC beams are monitored using a variety of instruments including wire scanners and synchrotron light monitors. The wire scanner physically passes through the beam and measures particles scattered by colliding with it. Charged particles caused to accelerate emit bremstrahlung photons or synchrotron light. A beam loss system consisting of ionizing gas chambers outside the magnets detects any particle flux that could be the result of a misdirected beam or a beam collision with a foreign object. A large enough flux will trigger a beam dump.

The nominal LHC luminosity is 10^{34} cm^{2}s^1, for beams of 2,808 bunches of 1.1×10^{11} protons each for interactions at ATLAS (Point 1) and CMS (Point 5). Machine luminosity monitors are installed near the interaction points and measure the flux of neutral particles (neutrons and photons) created in the collisions in order to calculate the instantaneous luminosity.

2.1.9 Control system

The LHC control architecture is based on standard components that are deployed worldwide for the control of accelerators. The two new principles that have been introduced in the LHC era are the consistent use of object-oriented software development and the wide use of industrial control solutions for complete LHC subsystems.

A powerful UNIX server is at the heart of the LHC control system. The CERN Control Center (CCC) has many workstations with Graphic User Interfaces (GUIs) enabling operators to control and monitor the various systems. The computer networks linking the CCC and the various parts of the LHC have no direct connection to the Internet and can be completely isolated if necessary.

An Oracle database solution was selected to house and manage the vast and complex datasets that will be generated during the lifetime of the LHC pertaining to the parameters of its operational history.

2.1.10 Beam dumping

The LHC beams at full energy have great destructive power. In the event that they must be quickly removed from the LHC two dedicated beam dumping systems (one for each beam) located at Point 6 are used. The beams are diffused and swept in an "*e*" pattern while being targeted at a beam dump absorber block (TDE). This diffusion and sweeping process extends the operational lifetime of the TDE core to 20 years. The TDE core is a steel clad carbon cylinder of length 7.7 m and diameter 0.7 m, which is surrounded by 900 tons of concrete and steel radiation shielding blocks. Dismantling the TDE to exchange the core will require strict radiation control and remote handling.

2.2 The ATLAS Detector

2.2.1 Overview

The ATLAS detector is a large multipurpose particle detector installed in LHC experimental cavern point 1 at CERN. Planning for the detector was started in 1980 and construction was done concurrently with the LHC. The information in this section is summarized primarily from this reference [20], with any additional references noted where relevant.

The general physics requirements of the ATLAS detector are a consequence of the particle beams that can be delivered by the LHC. Fast, radiation-hard sensors and electronics that are capable of recording data with high granularity are needed. This is due to the large, overlapping particle fluxes created by the LHC collisions. Thus the detector also needs to have high acceptance, meaning that it has full coverage of the collision point and would detect particles leaving in almost any direction. The detector has good momentum resolution and reconstruction efficiency for charged particles both near and far from the particle beam interaction point. The former allows for good object and interaction point identification and the latter for accurately determining the charge of high momentum muon particles. The detector has very good energy measuring components (calorimeters) for measuring both observed particles and for deducing the presence of unobserved particles. Any so-called ‘missing energy’ could be due to particles that escaped detection. These escaped particles could be either known particles that are hard to detect or new yet to be discovered particles.

Figure 2.3: ATLAS coordinate system

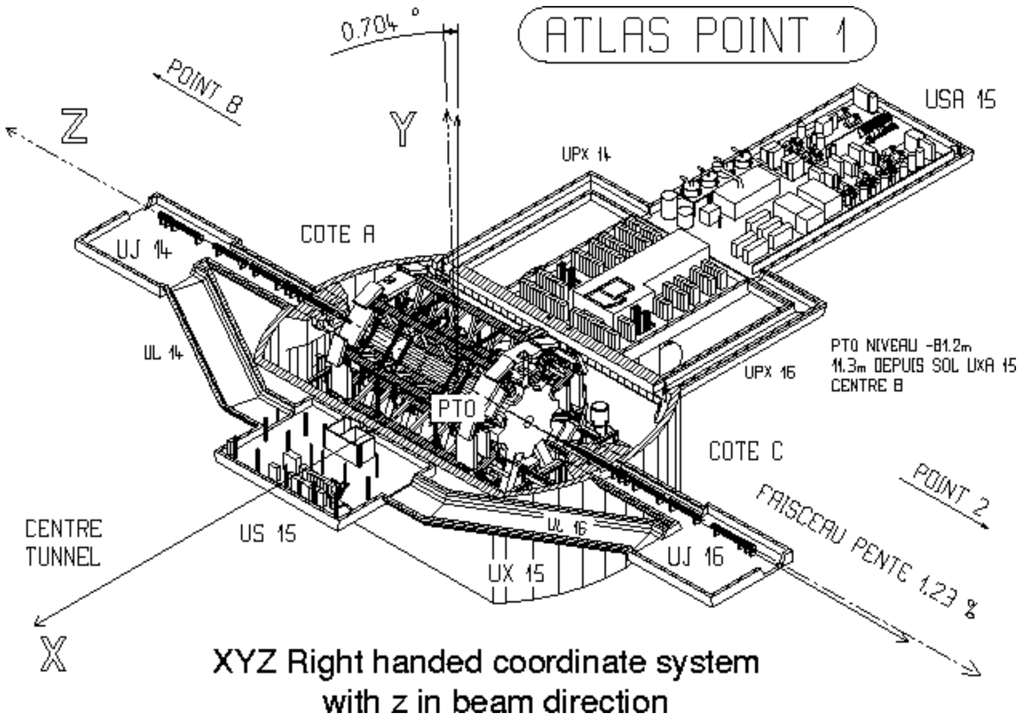

It is only possible to store a small fraction of the data gathered, so highly efficient triggering is needed to identify objects of interest.

The ATLAS detector uses a right-handed cartesian coordinate system with the origin centered on the nominal beam interaction point, shown in Figure 2.3. The beam direction defines the z-axis and the $x - y$ plane is defined transverse to the beam direction. The positive x-axis points towards the center of the LHC ring and the positive y-axis points upwards.

An additional cylindrical coordinate system in superimposed with the origin at the nominal interaction point. The azimuthal angle ϕ is defined around the beam axis, and the polar angle θ is measured from the positive beam axis. The polar angle is

Detector Component	**η coverage**	**Required Resolution**
Inner detector	± 2.5	$\frac{\sigma_{p_\mathrm{T}}}{p_\mathrm{T}} = 0.05\%\, p_\mathrm{T} \oplus 1\%$
EM calorimetry	± 3.2	$\frac{\sigma_E}{E} = \frac{10\%}{\sqrt{E}} \oplus 0.7\%$
Hadronic calorimetry (jets)		
barrel and end-cap	± 3.2	$\frac{\sigma_E}{E} = \frac{50\%}{\sqrt{E}} \oplus 3\%$
forward	$3.1 < \lvert\eta\rvert < 4.9$	$\frac{\sigma_E}{E} = \frac{100\%}{\sqrt{E}} \oplus 10\%$
Muon spectrometer	± 2.7	$\frac{\sigma_{p_\mathrm{T}}}{p_\mathrm{T}} = 10\%$ at $p_\mathrm{T} = 1\,\mathrm{TeV}$

Table 2.1: Pseudorapidity (η) coverage and required resolution of the detector components

commonly transformed into pseudorapidity η, given by:

$$\eta = -ln \tan\frac{\theta}{2} \tag{2.6}$$

The diagram of the ATLAS detector in Figure 2.4 shows that it is forward-backward symmetric about the interaction point. It is comprised of three main sections: the barrel and two end-caps, with most sub-detector systems having components distributed across all three sections. The areas where the barrel and end-cap sections join are known as cracks; detector performance in generally poorer in these areas. Table 2.1 shows the angular coverage in η of each detector component.

The central solenoid magnet encompasses the inner detector systems. The three inner detector systems are made of discrete, high resolution semiconductor pixels; semiconductor strips; and straw tubes. These all provide tracking and momentum measurement functions, with the first also providing particle interaction vertex identification and the last also providing particle identification using the transition radiation effect.[6]

The next layers provide particle energy measurements through the use of calorimeter systems. The first is an electromagnetic sampling calorimeter whose primary function is measuring the energy of photons and electrons. The second is an hadronic calorimeter whose primary function is measuring the energy of hadronic particles, such as protons and neutrons.

The final system is the muon spectrometer, whose primary purpose is to measure the momentum of muons. It contains three layers of tracking chambers arranged around an air-core toroid magnet system. It also contains the trigger chambers that are needed to reduce the amount of data collected to what can feasibly be read out and stored.

---

[6] Electromagnetic transition radiation occurs when a charged particle passes across the boundary between two materials of different dielectric constants.

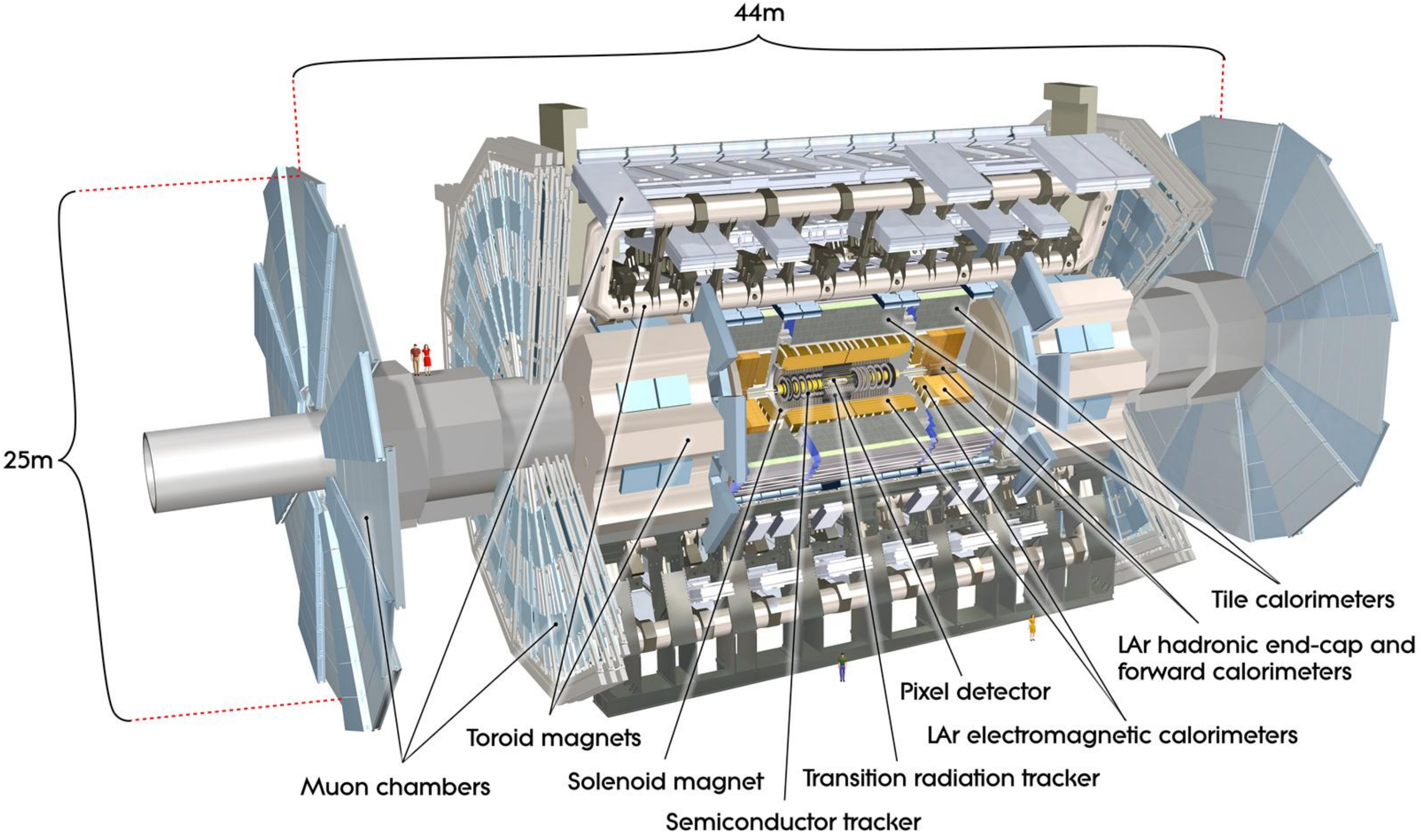

Figure 2.4: A cut-away view of the ATLAS detector. Its mass is approximately 7,000 tons; notice the human figures for scale.

2.2.2 Magnet system

The ATLAS magnet system is the product of 15 years of design, construction and installation work and comprises four unique superconducting magnets: the central solenoid, the barrel toroid and two barrel end-caps. Their magnetic field strengths are 2 T, approximately 0.5 T and 1 T respectively. Together they store 1.6 GJ of energy in their magnetic fields when operational. The fundamental choice of magnet dimensions and strength drove the design of the rest of the ATLAS detector.

2.2.3 Inner Detector

The inner detector provides crucial particle track and vertex identification functions. These functions are even more important in the LHC era when the number and frequency of proton-proton collisions in the accelerator beam pipe is increased from previous experiments. The entire inner detector is immersed in a uniform 2 T magnetic field aligned along the z axis and provided by a central solenoid. The momentum of charged particles is determined from the radius of curvature of their tracks in this magnetic field.

Figure 2.5 shows a detailed view of the barrel section of the three inner detector subsystems: the silicon-pixel detector that has three layers of individual sensor elements of size 50x400 μm^2; the silicon-microstrip tracker (SCT) that has four double layers of pitch 80 μm offset from each other at 40 mrad; and the transition radiation tracker (TRT) of nominally 36 layers of straws of diameter 4 mm filled with a Xe/CO$_2$/O$_2$ gas mixture. The pixel and the SCT have approximately 80.4 million and 6.3 million readout channels respectively. These two semiconductor trackers provide precision measurements of vertex location and impact parameter, which are important for identification of τ leptons and heavy-flavor [7] particles. The TRT has approximately 351,000 readout channels, but its larger size means that it provides a longer measured track length and so it still contributes significantly to momentum measurements. In addition, the TRT contributes to electron identification through the detection of transition-radiation photons in the xenon-based gas mixture.

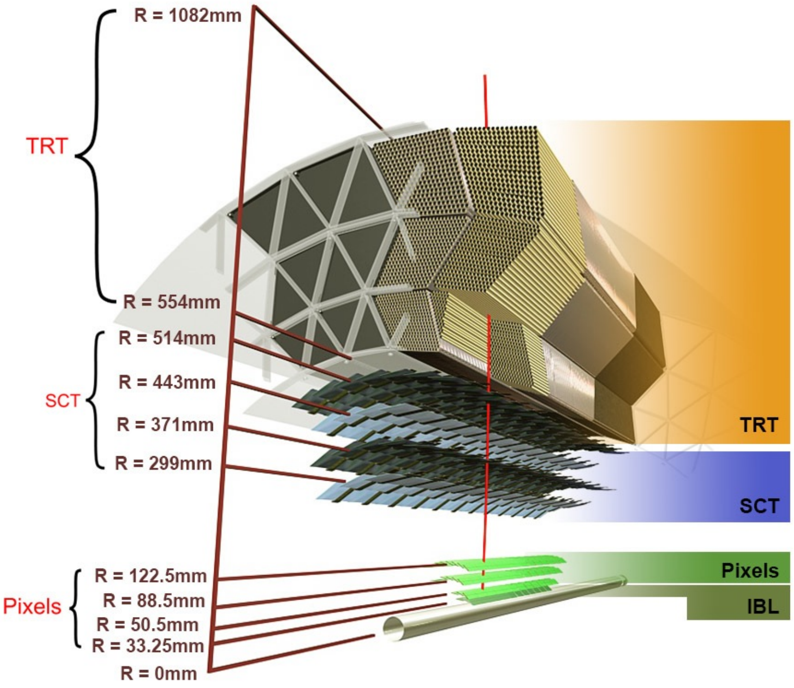

Figure 2.5: A cut-away view of the ATLAS inner detector showing details of the barrel sections of the three sub-systems being traversed by a simulated charged particle (track in red) of $p_{\mathrm{T}} = 10$ GeV and η=0.3.

During the long shut down of 2013 and 2014 an additional Insertable B-Layer

---

[7] In general, heavy-flavor particles are considered as those composite particles which contain a charm or bottom quark. The top quark is not included even though it is the heaviest because it does not exist long enough to form composite particles.

(IBL) of pixel sensors was installed at a nominal distance of 33.25 mm from the beam line. This was accomplished by replacing the existing beam-pipe with one of narrower diameter to which the IBL is mechanically integrated. The IBL greatly enhances primary vertex identification which leads to improved identification of *b*-hadrons (b tagging) and exclusion of secondary proton-proton interactions (pileup background). It has individual sensor elements of size 50x250 $\mu\mathrm{m}^2$ [21].

2.2.4 Calorimetry

The colorimeter systems, shown in Figure 2.6, must contain the electromagnetic and hadronic showers and measure them with adequate granularity. 'Punch-through' of high energy jets into the muon system must be limited, so an important design consideration is the calorimeter depth. In addition, table 2.1 shows that the calorimeter has the largest η coverage of any system, together these provide good missing transverse energy ($E_{\mathrm{T}}^{\mathrm{miss}}$) measurements. Many physics signatures, including searches for physics beyond the Standard Model, depend on accurate $E_{\mathrm{T}}^{\mathrm{miss}}$ measurements.

■ **Electromagnetic calorimeter**

The electromagnetic calorimeter system makes use of several active layers of alternating accordion shaped absorbers and electrodes that are submerged in a bath of liquid argon. The absorbers are made of lead and steel sheets that are approximately 2 mm thick, they cause the primary incident particle (a photon or electron) to electromagneticaly shower into secondary particles that in turn ionize the argon. The ionization electrons are collected at the copper electrodes by means of a 2,000 V

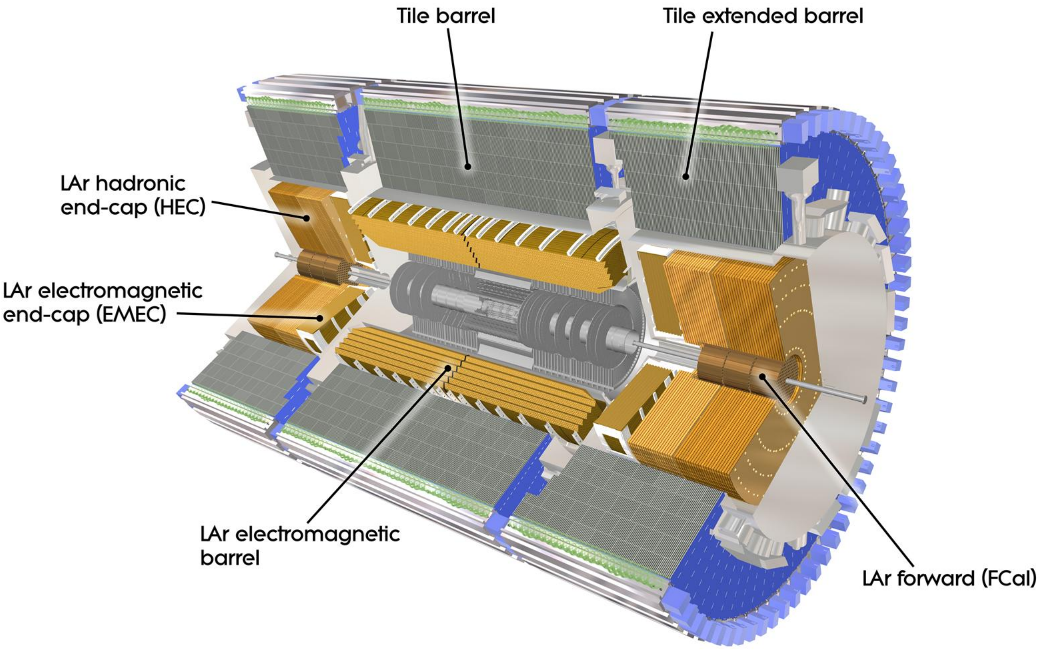

Figure 2.6: A cut-away view of the ATLAS calorimeter systems.

potential difference. The total charge collected is proportional to the energy of the original incident particle.

Thin liquid-argon pre-sampler calorimeters are installed before the main calorimeters. The measurements from these are used to calculate any necessary compensations in the energy calculation due to energy loss from photons and electrons as they travelled through the 'upstream' components of the inner detector. The use of liquid argon requires that the electromagnetic calorimeter components be contained in vacuum sealed cryostats.

■ Hadronic calorimeters

1) Tile calorimeter

The barrel section of the hadronic calorimeter consists of periodically interleaved steel absorbing plates and plastic scintillator tiles with a volume ratio of approximately 4.7:1. Incident hadrons (e.g. protons, neutrons, pions) produce showers of secondary particles that emit photons when traversing the scintillator tiles. These photons are collected by optical fibers and taken to photomultiplier tubes for measurement. The intensity of the collected light is proportional to the energy of the original incident particle.

2) **LAr hadronic end-cap calorimeter**

The hadronic end-cap calorimeter employs a similar technology to the electromagnetic calorimeter. Except the absorbers are made of copper, have a flat-plate design and are much thicker, at 25 mm in the front and 50 mm in the rear. There are three anode sheets in each gap between the copper plates; they are held at a potential difference of 1,800 V.

3) **LAr forward calorimeter**

This calorimeter has both electromagnetic and hadronic functionality. Its main functions are to increase the $E_{\mathrm{T}}^{\mathrm{miss}}$ coverage in η and to decrease the radiation background levels in the muon spectrometer. A modified copper plate and anode structure submerged in a bath of liquid argon is used for this system. Each end-cap has one cryostat that contains and integrates all neighbouring LAr calorimeters.

2.2.5 Muon spectrometer

The ATLAS muon system, shown in Figure 2.7, is the outermost system of the ATLAS detector and defines its overall dimensions. It operates by deflecting charged particles

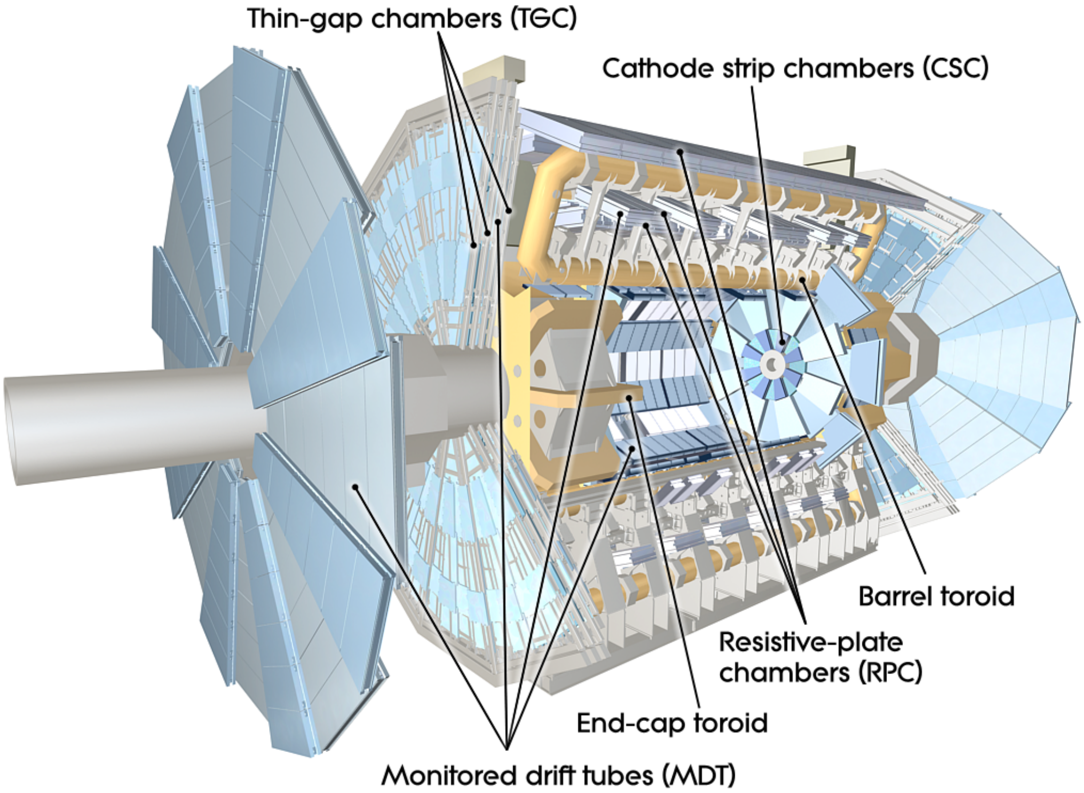

Figure 2.7: A cut-away view of the ATLAS muon system.

(primarily muons) using magnetic fields that are mostly oriented orthogonally to the direction of muon travel as they pass through three layers of tracking chambers. The magnetic field is generated by large superconducting air-core toroid magnets, one system for the barrel and one for each end-cap. The field strength of the toroid magnet system is a function of η and ϕ. Its low density design minimises unwanted multiple scattering interactions.

There are four different types of muon chambers, each utilising a different technology and serving a specialized purpose. Some types act as precision tracking chambers and are used to determine a particle's trajectory (and thus momentum). Some types acts as triggering chambers and are used to identify bunch crossings, determine accurate transverse momentum (p_{T}) thresholds, and to provide an orthogonal muon coordinate to that of the precision tracking chambers. Some types act as both tracking and triggering chambers. Adequate performance of the muon spectrometer depends on relative alignment of the chambers to within 30 μm.

The monitored drift tube (MDT) chambers are found in both the barrel and end-cap sections. Their purpose is to provide precision tracking.They are constructed of tubes filled with Ar/CO_2 gas (93/7) pressurized to 3 bar. Particles traversing a tube ionize the gas mixture and the free electrons travel to a wire running down the center of each tube that is kept at a potential difference of 3080 V. The trajectory of the original incident particle is determined from these electric signals as it crosses many tubes. In the region $2<|\eta|<2.7$ the expected counting rates exceed the safe operating limit of 150 Hz/cm^2 for the MDTs.

Thus, cathode-strip chambers (CSC) are used here in the central inside surface of the end-cap sections instead. They have a safe operating limit of counting rates up to 1,000 Hz/cm^2. CSCs are based on multiwire proportional technology; each filled with Ar/CO_2 gas (4/1) and having four layers of alternating anode wires and cathode strips arranged perpendicularly to each other and spaced evenly apart. Particles traversing a tube ionize the gas mixture and the free electrons travel to the anodes and positive ions to the cathodes. Only the signals from the cathodes are read out and the trajectory of the original incident particle is determined from the amount of charge collected from each anode and the time it takes to arrive at the readout electronics. The purpose of the MDT is to provide precision tracking.

The resistive plate chambers (RPC) are found in the barrel section. They are constructed out of two parallel plastic plates kept insulated from each other at a distance of 2 mm. The space in between is filled with a predominantly Hydrofluorocarbon (HFC) gas mixture and the plates are kept at a potential difference of 9.8 kV. Metallic strips are mounted to the outside of the plates, which capacitively couple to any avalanches created by ionizing particles traversing the chamber. The function of the RPCs is to provide muon triggering in the barrel section of the ATLAS detector.

The thin-gap chambers (TGC) are found in the end-cap sections. They provide triggering in these regions and and also a measurement of the azimuthal coordinate for tracking purposes. TGCs use a multiwire proportional design, chambers have either two or three layers of discrete gas volumes with a row of anode wires in each. The volumes are 2.8 mm wide and filled with a CO_2 n-pentane gas mixture.

2.2.6 Forward detectors

Three smaller detector systems are installed symmetrically along the beam pipe on either side of the ATLAS detector. They cover the very forward region and each serve a specialized function.

- **LUCID**

LUCID (LUminosity measurement using Cerenkov Integrating Detector) is installed at ±17 m from the interaction point and directly on the outside of the beam pipe. It detects inelastic proton-proton scattering in order to monitor instantaneous luminosity and beam conditions and also to measure integrated luminosity. It must be very radiation tolerant, have the ability to count single particles, veto particles not incident from the interaction point and have a 25 ns time resolution. LUCID is based on the principle that the number of inelastic protons collected is directly proportional to the number of interactions per bunch-crossing. Incident protons enter one of 20 aluminium gas vessels filled with C_4F_{10} where they emit Cerenkov light which is collected by a photomultiplier tube.

■ The ALFA detector

The ALFA (Absolute Luminosity For ATLAS) detector is installed at ±240 m from the interaction point. It determines the absolute luminosity by measuring the amplitude of elastically scattered particles and using it to determine the total cross-section and thus the luminosity. It uses a Roman pot method where the sensor elements of the detector can be moved as close as 1 mm to the beam in order to detect particles scattered as little at 3 μrad. ALFA uses a scintillating fiber tracker and photomultiplier tubes.

■ The zero-degree calorimeter

The zero-degree calorimeter (ZDC) is installed at ±140 m from the interaction point, were the two LHC beam pipes merge into one. It is only used when the LHC is colliding heavy ions and is used to detect very forward 'spectator' neutrons of $|\eta| > 8.3$. It consists of layers of quartz rods sandwiched between layers of steel and tungsten. Cerenkov light generated by showers is transferred through the quartz rods to photomultipliers.

2.2.7 Trigger

The ATLAS trigger system is responsible for reducing the amount of data gathered by the detector down to an amount that can feasibly be stored and analyzed based on technological and budgetary constraints. The decision about whether or not to retain an event is made by pre-programed instructions based on what particle signals are interesting for physics analyses, this is called a trigger. There is a minimum bunch spacing of 25 ns (or a maximum event rate of 40 MHz), and all the raw data from each event is stored in buffers for parallel processing. The first, or L1 trigger receives a subset of the raw data from certain sub detectors and decides in less than 2.5 μs which events to keep. Keeping an event is based on the presence of high transverse-momentum muons, electrons, photons, jets and τ leptons. Large total transverse energy and large missing transverse energy are also of interest. Additionally, the L1 trigger identifies interesting features, called Regions-of-Interest (ROI), and passes this information along the trigger chain.

This reduces the event rate down to about 75 kHz and these events are passed on to the second, or L2 trigger. The L2 trigger reads out more of the data about each event and applies a menu of predetermined selection criteria. This takes an average of 40 ms and reduces the event rate down to about 3.5 kHz. The final trigger is an event filter that takes place offline at an average of 4 s per event and reduces the event rate that is permanently stored below 200 Hz at an average size of 1.3 Mbytes per event.

This is necessary because the proton-proton interaction rate provided by the LHC running at the design luminosity of 10^{34} cm^{-2}s^{-1} is approximately 1 GHz, while we are only able to record data at approximately 200 Hz due to technology and resource limitations. This means that only about one in five million proton-proton collisions are recorded by the data acquisition system.

2.2.8 Data acquisition

Data acquisition (DAQ) is closely integrated with triggering since only events that pass L1, L2 and event filter triggers are stored. The DAQ has 1574 read out buffers that can transmit data at up to 160 Mbyte/s from the detector to the triggers. Data that passes all triggers is transferred to mass storage in CERN's central data-recording facility where is it duplicated on hard disks and also copied onto magnetic tape for long term storage. The trigger and data acquisition system are collectively known as the TDAQ.

2.2.9 Radiation shielding

The ATLAS detector makes use of 3,000 tons of shielding material that is integrated throughout the detector to protect various components from unwanted particles that could cause radiation damage and false triggers. They can also radioactively activate certain detector components making maintenance more difficult. The primary sources of radiation are unwanted particles originating at the interaction point, such as charged hadrons, neutrons and photons and exiting the beam-pipe at very shallow angles. Consequently much of the shielding material is arranged conically about the beam-pipe on either side of the interaction point to adsorb these particles.

The shielding materials are arranged in three layers, each layer designed to absorb a certain type of radiation. The first layer is made of high interaction length material such as iron or copper and designed to stop hadrons. The second layer stops neutrons by using a boron doped polyethylene layer rich in hydrogen. The third layer stops photons using a steel or lead shield.

2.2.10 Beam-pipe

A 38 m long section of the LHC beam-pipe traverses the center of the ATLAS detector. It is constructed in seven sections with the outer six made of steel and the the central section made of beryllium. Beryllium is used because it is a light element[8] that is transparent to high energy particles while also being strong enough to hold an ultra-high vacuum. However, beryllium is toxic to humans and must be handled with care.

2.2.11 Control system

The Detector Control System (DCS) integrates and automates the operation of all the detector subsystems. It continuously monitors the operating conditions, logs diagnostic parameters and can automatically make corrections. There is also a human interface that provides full control of the detector from the ATLAS control room. A small set of industry standard software and hardware tools was selected for use on all detector systems in order to streamline their integration into DCS and to simplify the operation of the ATLAS detector.

---

[8] Beryllium's atomic number is 4.

2.2.12 Installation

The components for the ATLAS detector were manufactured by a large number of institutions all over the world and brought to CERN for timely installation. Many of the components are large, costly and fragile in nature necessitating specialised shipping and handling. After arrival most components were assembled and validated on the surface to assure functionality before installation underground.

The supporting civil engineering and infrastructure development was completed before hand and was itself a large undertaking. This included excavating a cavern 92.5 m underground and installing all the necessary stairwells, elevators, electrical supplies, plumbing, gas, cryogenic, fire suppression, cooling and ventilation systems. Fitting together all the components of the detector in a cavern that is not much larger than the final detector dimensions proved particularly challenging. Periodic access for maintenance, upgrades and repairs is anticipated so the detector is designed so that it can be opened up without complete disassembly. The end-caps are on sliding rails and can be removed as a unit from the barrel. Accordion cables and bellows are used where necessary to ensure that critical components remain connected during this operation.

The order of subsystem installation was considered and modelled with CAD software prior to installation and verified against the CAD model after installation. Since the nominal LHC beam line is fixed all components had to be placed relative to it. A basic physics requirement is full hermetic coverage of the interaction point, so alignment of all the sensor components was particularly important.

This required an impressive project management effort of large scale which was aided by the use of industry standard software documentation tools to ensure timely milestone achievement. The ATLAS technical management team coordinated all relevant activities among the member institutes during installation.

The ATLAS detector is periodically calibrated to ensure correct alignment of sensor components within a subsystem and subsystems with each other. A combination of optical sensors and cosmic ray data is used to do this. Cosmic rays that penetrate the experimental cavern can leave tracks in the detector, and any recorded tracks that zig-zag indicate misaligned components. Known misalignments can either be fixed physically or after data collection with calibration software.

Chapter 3

Particle Identification

Particles are detected by the energy that they deposit in the various layers of the detector while transiting through them. Individual points of deposited energy (hits) are joined together in a connect-the-dots fashion to deduce the particle track in three dimensional space. Some particles will interact with the detector material to produce showers of secondary particles until all their energy is dissipated. Some particles will travel entirely through the detector without being absorbed. Common low mass particles have characteristic tracks and showers that are readily identified, as illustrated in Figure 3.1. The information in this section is summarized primarily from this document [20], with any additional references noted where relevant.

3.1 Track and vertex reconstruction

Tracking and vertexing are done by a suite of software tools that attempts to find the best fit between the hits in the detector. One of the statistical methods used for this is a global-χ^2 technique. The known affects on the particles due to the specific detector material through which they transited is also considered during track reconstruction. Tracking begins in the inner detector by taking raw data from the pixel and SCT converting it into a set of 3D space points. Then these points are combined with nearby points to form track seeds, which are then extended and combined with each other to create track candidates. Any outlier points and track seeds are removed. The

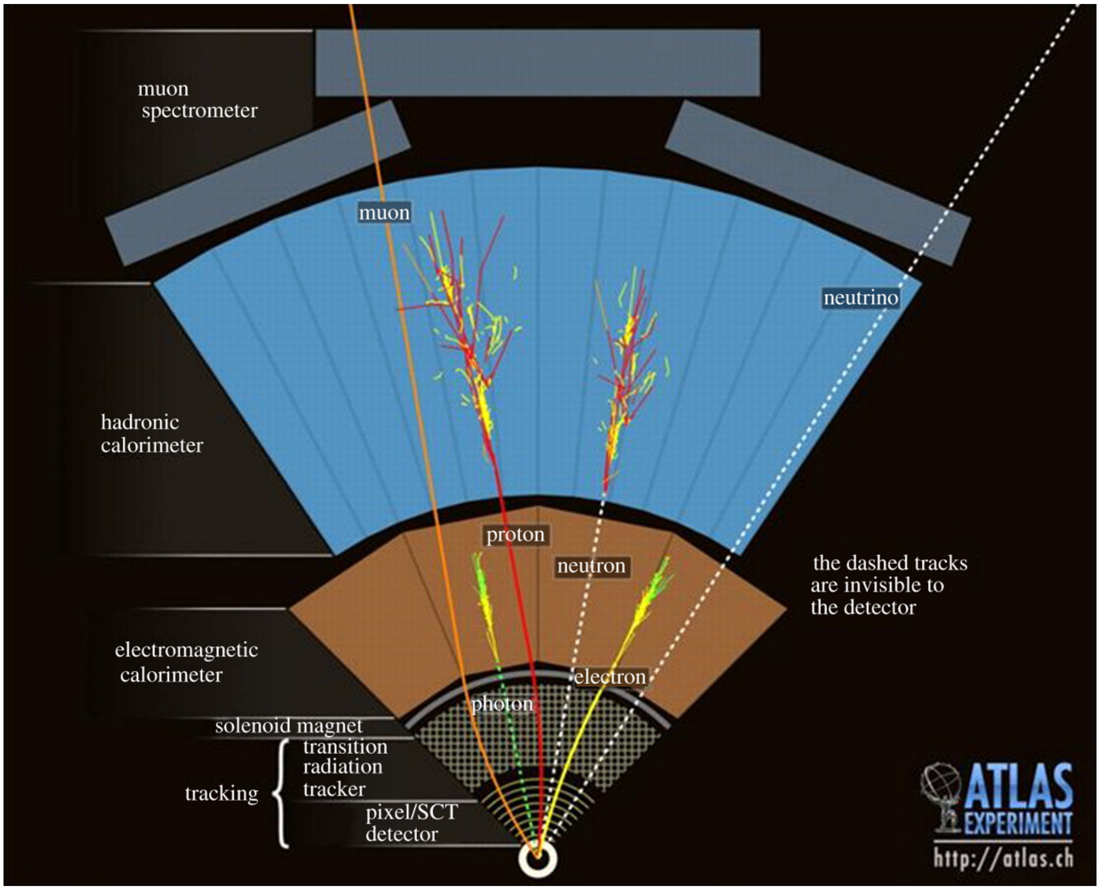

Figure 3.1: Characteristic tracks and showers left by common low mass particles in the ATLAS detector, only charged particles leave tracks. The direction of curvature of the particle track shows the sign of the charge and the radius of curvature is proportional to the momentum.

track candidates are then extended into the TRT and refit with the full hit information from all three sub-detectors to form the tracks. In a final step dedicated software is used to trace the tracks back to the interaction point in order to identify primary and secondary vertices, as shown in Figure 3.2. Tracks that extend outside the inner detector are compared with tracks found by the muon spectrometer and showers found in the calorimeters to look for matches, this is discussed in the next sections.

A particle of charge q moving with a velocity v in a magnetic field of strength B feels a force given by this equation:

$$\vec{F} = q\vec{v} \times \vec{B} = \frac{m\vec{v}^2}{r} \tag{3.1}$$

Where r is the radius of curvature of the particle's trajectory. This leads to an equation relating its radius of curvature to its momentum in the plane transverse to the z-direction (p_{T}):

$$p_{\mathrm{T}} = q|\vec{B}|r \tag{3.2}$$

3.2 Muon Identification

Muon identification makes use of information from all detector subsystems, not just from the muon spectrometer. This allows accurate measurement of muons within a wide η and momentum range. Three track reconstruction methods are used by the tracking software for muons that are in the approximate momenta range of 3 GeV to 3 TeV:

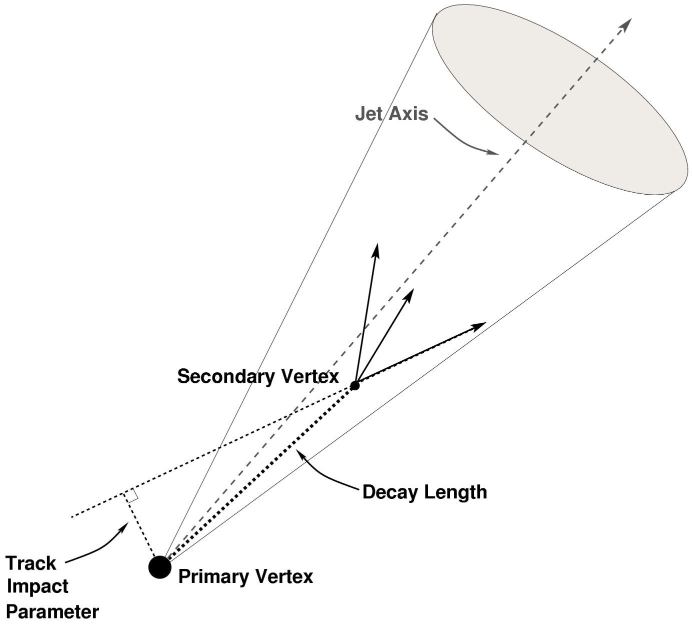

Figure 3.2: The primary vertex is the point where the original proton-proton collision took place. A secondary vertex may occur when an unstable high mass particle is produced and then decays into two or more lower mass particles, this may occur in the beampipe or in the detector volume. When this process happens repeatedly, the individual tracks may be grouped together and called a jet. The distance between the two verticies is called the decay length and the perpendicular projection of that distance is called the track impact parameter.

- Stand-alone: muons of $|\eta| < 2.7$ and only detected in the muon spectrometer.
- Combined: muons of $|\eta| < 2.5$ and detected both in the inner detector and in the muon spectrometer.
- Segment tag: muons detected in the inner detector and in only one inner muon spectrometer segment.

ATLAS software uses two different sets of reconstruction algorithms; both sets use the three strategies outlined above. They are called ‘MuID’ and ‘Staco’ after their respective combined muon reconstruction algorithm names [22]. Both sets of reconstruction algorithms produce very similar results and follow the steps outlined below.

The software proceeds with muon identification in distinct stages: first by pattern matching and segment making within individual chambers of the muon spectrometer, then by connecting segments into track candidates. Inhomogeneities in the magnetic field crossed by the track candidate are considered. The track candidate is propagated back to the interaction point in order to correct its momentum due to energy lost while crossing the inner detector, calorimeters and any inert material. Once a stand-alone muon is found within $|\eta| < 2.5$ then a combination with a track from the inner detector to form a combined muon is attempted. Combined muons have improved momentum resolution for momenta below 100 GeV and lower backgrounds from pion and kaon decays.

If a muon track is identified only in the inner detector, it is extrapolated to the inner layer of the muon spectrometer to see if it matches any track segments there. Segment tagged muons found in this way could have a momentum below 6 GeV and not have reached the outer chambers of the muon spectrometer. Or they could be in an area of poor muon spectrometer coverage, e.g. $1.1 < |\eta| < 1.7$ (the crack), $|\eta| \approx 0$ or in the detector support structures (known as feet).

Additionally, a combined or segment tag muon is said to pass muon combined performance (MCP) cuts if the track satisfies these criteria [23]:

- At least one Pixel hit.
- At least five SCT hits.
- Two of fewer active Pixel or SCT sensors traversed without registering a hit.
- At least nine TRT hits in the region of full TRT acceptance, i.e., $0.1 < |\eta| < 0.9$.

3.3 Electron and photon identification

Electron and photon reconstruction software begins by considering showers found in the electromagnetic calorimeters. It then tries to match these showers with a track found in the inner detector. Electrons are defined as having an associated track and photons are defined as having none. Additional parameters are then considered to refine the identification of electrons: the ratio of the energy as measured by the calorimeter to the momentum as measured by the inner detector, any difference in the coordinates η and ϕ as measured by those two systems and any transition radiation measured by the TRT.

Electron η and ϕ are determined most accurately by the inner tracker and energy is determined most accurately by the calorimeter. Electron transverse momentum is well measured by the inner tracker for energies below 30 GeV. Above this value the track is so straight that measuring a radius of curvature is difficult and the calorimeter energy measurement becomes more important. All photon information is measured by the calorimeter.

3.4 Jet Reconstruction

Many physics processes produce unstable high mass particles as a final state product, which can rapidly decay and re-decay into lower mass particles. In addition, if a bare quark or gluon is produced it pulls additional objects out of the vacuum around it in a process called hadronization or fragmentation. This produces a collimated spray or particles extending away from the interaction point. This is known as a jet. It is not important to identify and measure each particle in this case, but rather to measure the total energy and direction of the jet as a whole. This process can become complicated in the active environment of the LHC which produces many overlapping jets. The two default types of jet-clustering algorithms used by ATLAS software to reconstruct jets are 'seeded fixed-cone' and 'successive recombination'.

In the fixed-cone algorithm, software reconstructs jets by grouping together all the tracks and showers in a three dimensional cone shaped space of radius $\Delta R = \sqrt{\Delta\eta^2 + \Delta\phi^2}$. This is implemented in the high-level trigger, but for jet reconstruction more sophisticated successive recombination algorithms are now used. These do not require jets to have a fixed conical shape, rather they perform an iterative process resulting in jet objects made up of the sum of the tracks or energy clusters that have been assigned to them. The primary recombination algorithm is called anti-k_t, it is more efficient than fixed-cone algorithms for large numbers of objects, does not need a pre-clustering step and makes further improvements by taking into account additional particle fragmentation modes. For more information on this algorithm please see Reference [24].

3.5 Missing transverse energy

Many physics analyses require a very good measurement of missing energy. The colliding proton beams have a known momentum which is assumed to be entirely along the $z-axis$. But the percentage of that momentum that is carried by each constituent parton is unknown. So after an event the total amount of missing energy can not be determined, only the amount of missing energy in the transverse direction ($E_{\mathrm{T}}^{\mathrm{miss}}$), which is the vector sum of the missing transverse energy in the x and y directions:

$$\vec{E}_{\mathrm{T}}^{\mathrm{miss}} = \vec{E}_{\mathrm{Tx}}^{\mathrm{miss}} + \vec{E}_{\mathrm{Ty}}^{\mathrm{miss}} \tag{3.3}$$

Particle physicists use natural units, making energy and momentum equivalent quantities. Since the calorimeters measure energy we use the term 'energy vector' even though energy is really a scalar quantity. The $E_{\mathrm{T}}^{\mathrm{miss}}$ term is constructed by first taking the calibrated energies from all the calorimeter cells and the muon spectrometer. A correction term is added to account for the energy lost by particles that travel through the LAr electromagnetic cryostat to the tile hadronic calorimeter. A final step refines the measurement by using the track based p_{T} measurement of high p_{T} objects to recalibrate the calorimeter cells near them.

The direction of the $E_{\mathrm{T}}^{\mathrm{miss}}$ vector in the azimuthal plane can be determined, but the direction accuracy deteriorates for low values of $E_{\mathrm{T}}^{\mathrm{miss}}$. Fake $E_{\mathrm{T}}^{\mathrm{miss}}$ results from any difference in the true and measured $E_{\mathrm{T}}^{\mathrm{miss}}$ and can come from many sources. These include high energy muons escaping detection by travelling down the beam pipe and and large energy deposits in the crack regions or in inactive materials. These effects have been studied in detail in order to reduce fake $E_{\mathrm{T}}^{\mathrm{miss}}$ measurements.

Chapter 4

Measurement of the $J/\psi + W^{\pm}$ Production Cross Section.

4.1 Theoretical motivation

There are a variety of theoretical models that describe the production of the J/ψ meson with an associated $W^{\pm}$ boson. The extent to which each model contributes to the production cross section is not well known and experimental measurements can shed light on this open question. In addition, measuring the $J/\psi + W^{\pm}$ production is a novel method of examining the double parton scattering process [25], where the two particles in question are produced by two separate pairs of interacting partons within one proton-proton interaction. We present an observation of prompt $J/\psi + W^{\pm}$ and a measurement of the production rate as a ratio to the inclusive $W^{\pm}$ production rate. We use the decay channels $J/\psi \to \mu^{+}\mu^{-}$[1] and $W^{\pm} \to \mu^{\pm}\nu$.[2] We separate out the prompt production components by applying selection criteria to remove background, a two-dimensional J/ψ mass and lifetime fit, subtracting the remaining backgrounds modelled by Monte Carlo (MC) and estimating QCD and pileup backgrounds as described later. We do not distinguish J/ψ events that are produced from decays of heavier charmonium states (such as $\chi_c \to \gamma J/\psi$)[3], as long as they are produced in

---

[1] The $J/\psi \to e^{+}e^{-}$ channel is not used because the ATLAS detector has poor signal efficiency for the J/ψ relevant momentum range.

[2] The $W^{\pm} \to e^{\pm}\nu$ channel does not give as clean of a signal and requires additional corrections, so it was not used.

[3] The χ_c is another charm-anticharm particle that has a higher mass and different spin than the J/ψ.

the initial hard interaction. The models proposed for J/ψ production and then its production in association with W are discussed, followed by the experimental results.

4.1.1 J/ψ production

In spite of being studied for some decades, the production modes of J/ψ are not well understood, as evidenced by observed behavior not explained by the proposed models [26, 27, 28, 29, 30, 31, 32].

The main models used to explain J/ψ (and other heavy quarkonium) production at hadron colliders are the Color Singlet (CS) model and the Color Octet (CO) model [33, 34, 35, 36, 37]. Including the CO model brings greater agreement between theory and data than using the CS model alone. Both the CS and CO models involve gluon gluon fusion and can be written down as:

$$g + g \rightarrow c\bar{c}[J/\psi] + g \tag{4.1}$$

The CS model directly produces a color singlet J/ψ from the gluon gluon fusion. The CS model leaves the $q\bar{q}$ in a color singlet state (i.e., $q\bar{q}^{[1]}$) after the perturbative QCD interaction. This allows for immediate coupling to a final-state meson. The CS model requires either two hard gluons in the initial state, or one gluon splitting to $q\bar{q}$ where one of those quarks radiates a hard gluon.

The CO model leaves the $q\bar{q}$ system in a color octet state (i.e., $q\bar{q}^{[8]}$), which then transitions to the final color-neutral J/ψ meson through low-energy nonperturbative matrix elements using a soft gluon exchange. The cross-sections for hadronic quarkonium production can be predicted using a NRQCD framework given that the

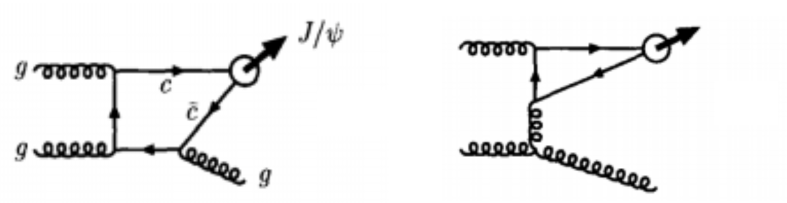

(a) (b)

Figure 4.1: Leading order Feynman diagrams showing J/ψ particle production in the Color Singlet (a) and Color Octet (b) models.

necessary matrix elements have first been determined from other processes. The differences between the two models can be more readily seen in the Feynman diagrams in Figure 4.1.

Both models have their shortcomings because they predict results that do not match with observations. The CS model wrongly predicts cross section numbers and that most J/ψ particles will come from χ_c decays. The CO model correctly predicts the cross section numbers, but wrongly predicts the spin alignment profile.

These two models are focused on in this dissertation since they can be used to show J/ψ + $W^{\pm}$ production. Other models for J/ψ production, such as the Color Evaporation Model [38] have been proposed, but they are not discussed further. It is still not known which model or combinations of models most accurately explain J/ψ production.

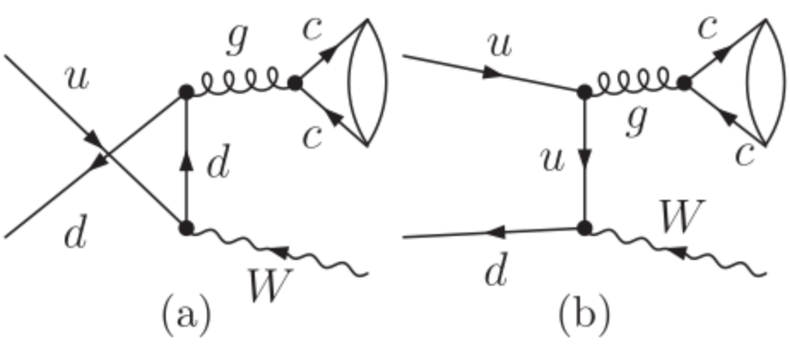

Figure 4.2: Leading order Feynman diagrams showing $J/\psi + W^{\pm}$ production for the Color Octet Model.

4.1.2 J/ψ + $W^{\pm}$ production

J/ψ + $W^{\pm}$ can be produced at the leading order only by CO processes since the $W^{\pm}$ boson does not interact strongly. The lowest order diagram is the CO process $q\bar{q}' \to W^{\pm}g \to W^{\pm}q\bar{q}^{[8]}$ and measuring the cross section provides information on the relevant NRQCD matrix elements [39]. This was originally the dominant mechanism discussed in the literature [40, 41] and observation of the J/ψ + $W^{\pm}$ was used to conclusively confirm the CO model [34, 35]. It can be written down as:

$$u\bar{d} \to c\bar{c}[J/\psi] + W^{+}; \bar{u}d \to c\bar{c}[J/\psi] + W^{-} \tag{4.2}$$

and also expressed as the Feynman diagrams shown in Figure 4.2. In 2013 theorists proposed that second order CS models could actually have contributions comparable to the CO model [42]. One of these uses strange quark - gluon fusion to create a $W^{\pm}$ + charm quark pair, followed by the charm hadronizing into a J/ψ, which can be written down as:

$$s + g \to W + c + J/\psi \tag{4.3}$$

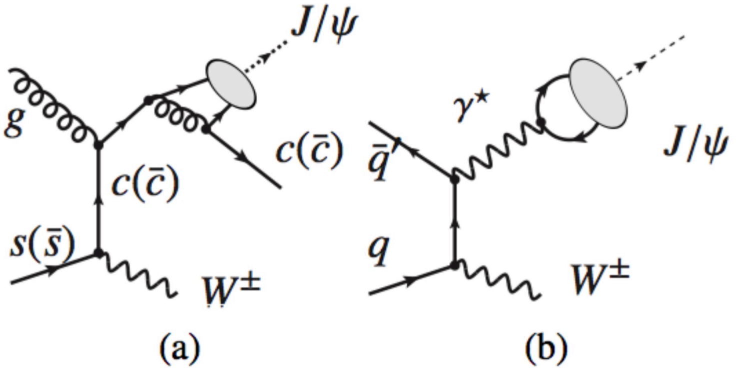

Figure 4.3: Representative Feynman diagrams showing J/$\psi + W^{\pm}$ production for the Color Singlet Model.

Another uses a quark - antiquark interaction to produce a $W^{\pm}$ and off shell photon, where the photon then produces the J/ψ bound state:

$$q + \bar{q}' \to W + \gamma^{*} \to W + J/\psi \tag{4.4}$$

Figure 4.3 shows the Feynman diagrams for these CS model contributions. There is evidence that the CS processes for J/ψ+$W^{\pm}$ production are sizable, if not dominant over the CO contributions [42].

J/ψ can also be produced by radiative decays from higher mass charm-anticharm mesons such as the χ_c. These feed-down decays are taken into account by the CS model calculations.

Measuring $J/\psi + W^{\pm}$ complements the direct and indirect J/ψ production measurements that can also be made at hadron colliders. Such measurements can shed light on the debate over the relative contributions of the CO and CS processes to J/ψ production [26, 27, 28, 29, 30, 31, 32]. Different initial partonic states are selected for

$J/\psi + W^{\pm}$ associated production as compared to J/ψ production meaning that there should be a difference between the relative contributions of the CO and CS process.

The spin alignment profile of J/ψ particles produced in association with a $W^{\pm}$ particle could be different from those produced alone. Understanding this profile for both processes is necessary to better understand the J/ψ production mechanism and better measure its cross-section.

4.1.3 Previous measurements

The cross section ratio measurement presented in this dissertation was performed previously using 4.5 fb^{-1} of data collected from proton-proton collisions by the ATLAS detector at the LHC at a center of mass energy $\sqrt{s} = 7$ TeV during 2011 [43]. $27.4^{+7.5}_{-6.5}$ $W^{\pm}$ plus prompt J/ψ events were observed. The measurement presented in this dissertation uses data collected at a higher center of mass energy of $\sqrt{s}$ 8 TeV aims to improve on the previous one by virtue of having more than four times the available data.

4.2 Analysis strategy

This analysis measures the ratio given by the fiducial and inclusive[4] cross sections of associated prompt $J/\psi + W^{\pm}$ production divided by the cross section of inclusive $W^{\pm}$ production using proton-proton (pp) collisions of center of mass energy $\sqrt{s} =$ 8 TeV at the LHC. In addition we provide the differential cross section ratio as a function of the J/ψ transverse momentum in the case of the inclusive measurement. Prompt production occurs when the J/ψ is produced directly from the pp collision and non-prompt production occurs when it is produced from a secondary vertex, such as a b-hadron decay. This measurement focuses on prompt production because the background from $t\bar{t}$ decays is very large for non-prompt production and it is difficult to extract a signal.

To calculate the cross section ratio, two sets of selection criteria are applied to the 2012 data in sequence. The first set of selection criteria generates the inclusive sample by selecting events containing a candidate $W^{\pm}$ boson. A second set of selection criteria generates the associated sample by starting with the inclusive sample and further selecting events that also contain a candidate J/ψ meson. This generates two data samples that are used to calculate the cross section ratio. The advantage of using this ratio method is that any efficiencies and corrections that would normally be needed when measuring the $W^{\pm}$ boson cancel out, as well as the trigger and luminosity efficiencies.

---

[4] The ATLAS detector cannot detect every single particle created due to technological limitations. The fiducial measurement is made from the particles actually detected. This measurement is then extrapolated to estimate the inclusive measurement, i.e., the result that would have been obtained had the ATLAS detector been able to detect every particle that was generated.

This analysis attempts to further discriminate between single parton scattering (SPS) and double parton scattering (DPS) by providing a measurement with the DPS component subtracted. SPS occurs when the J/ψ and $W^{\pm}$ particles are produced from one pair of proton partons in the pp collision. DPS occurs when the J/ψ and $W^{\pm}$ particles are produced from two different pairs of partons colliding in the same pp collision.

For the associated sample, J/ψ candidates are reconstructed using the $J/\psi \to \mu^+\mu^-$ channel and $W^{\pm}$ candidates are reconstructed in the $W^{\pm} \to \mu^{\pm}\nu$ channel. Pairs of muons are combined into J/ψ candidates and are required to be within the J/ψ mass window of $2.4< m_{J/\psi} <3.8$ GeV. If there is a third muon in the event and it passes the $W^{\pm}$ selection criteria the event is further retained. This associated $J/\psi + W^{\pm}$ sample is fitted with J/ψ mass and pseudo-proper time models using a two-dimensional unbinned maximum likelihood fit. After the fit is performed, an sPlot [44] procedure is used to apply weights according to the likelihood that the events are prompt, non-prompt or one of the backgrounds.

The inclusive $W^{\pm}$ sample is also reconstructed using the $W^{\pm} \to \mu^{\pm}\nu$ channel. It is produced by taking the original full data sample and applying only the $W^{\pm}$ selection criteria to it.

Many adjustments are applied to these samples to remove backgrounds and correct for detector effects; these are discussed in the following sections. Once the final corrected yields are found, then the cross section ratio is calculated. The measurement is performed in two J/ψ rapidity bins, $0 < |y_{J/\psi}| < 1$ for the barrel and $1 < |y_{J/\psi}| < 2.1$

for the endcap. We present separate results for both regions as well as a total combined result for the entire rapidity range.

4.3 Dataset and MC samples

The full 2012 data set of $20.3\,\text{fb}^{-1}$ of data collected by the ATLAS detector with the LHC running at $\sqrt{s} = 8\,\text{TeV}$ is used in this analysis. The muon stream output shown in Table 4.1 was used, which requires at least one muon of $p_{\text{T}} > 24$ GeV to be present in each event.

Muon stream
data12_8TeV.periodAllYear.physics_Muons.PhysCont.AOD.pro14_v01/

Table 4.1: Dataset used

MC samples are generated using PYTHIA8 [45], ALPGEN [46], MC@NLO [47], AcerMC [48] and HERWIG/JIMMY [49, 50] generators. Samples generated include the associated $J/\psi + W^{\pm}$ production signal, the inclusive $W^{\pm}$ production signal and the known physics backgrounds.

Since there is no option to simulate the associated production of electroweak bosons with quarkonia particles through an SPS process in Pythia8, we first generate the J/ψ as a standard charmonium process and then produce the $W^{\pm}$ via a second hard DPS process (see Table 4.2). Another MC sample of non-prompt $J/\psi + W^{\pm}$ was generated, were the J/ψ originates from B decays (see Table 4.3).

Table 4.4 lists the MC samples that are used to model the inclusive $W^{\pm}$ production

J/$\psi \to \mu\mu, W \to \mu, \nu$:208019
mc12_8TeV.208019.Pythia8B_AU2_CTEQ6L1_ JpsimumuWmunu.merge.AOD.e3249_a188_a180_r3549/

Table 4.2: Associated prompt production Monte Carlo sample.

$B \to J/\psi \to \mu\mu, W \to \mu, \nu$:208223
mc12_8TeV.208223.Pythia8B_AU2_CTEQ6L1_bb_ Jpsimu2p5mu2p5_Wmunu_fiducial.recon.AOD.e3249_a188_a180/

Table 4.3: Associated non-prompt production Monte Carlo sample

signal and table 4.5 lists the MC samples that are used to estimate the known physics backgrounds. These tables also show the process and generator identification numbers (DSIDs); the cross-section times branching ratios ($\sigma\times$ BR(pb)), which are related to the relative probability of a process to occur; and the k-factors, which are constants set to get the correct inclusive cross-section and so that the MC generators produce results in agreement with certain computed observables.

4.3.1 MC sample weights

The MC samples must be properly weighted to improve their ability to model real physics data [51]. The ATLAS detector is not perfectly efficient, so some fraction of particles that are generated are not detected; particles that are detected may be mis-identified or mis-measured. This weighting process allows the the MC simulation

Process	DSID	$\sigma\times$ BR(pb)	k-factor	Notes
Alpgen+Herwig/Jimmy W+jets $\rightarrow \mu\nu$	107690	8040.9	1.1760	0-jet
	107691	1581.0	1.1760	1-jet
	107692	477.53	1.1760	2-jet
	107693	133.83	1.1760	3-jet
	107694	35.579	1.1760	4-jet
	107695	10.561	1.1760	5-jet

Table 4.4: Details of the MC samples used to model the inclusive $W \rightarrow \mu\nu$ signal.

to better mimic the actual dataset recorded by the detector. MC generators are developed to include a best guess estimation of all these factors, but the actual performance of the ATLAS detector in not known until after the data is collected. So the MC samples must be weighted after they are generated to account for the actual conditions encountered during data taking.

Depending on the type of weight, it is calculated and applied on a per sample, per event or per variable basis. The MC scale factor is calculated on a per sample basis and is determined from the cross-section, k-factor and generator efficiency (equal to one) for each sample. For each sample, an MC luminosity is calculated, where:

$$\text{MC\_}\mathcal{L} = \frac{\text{number of events}}{\text{cross section * k\_factor * generator efficiency}} \tag{4.5}$$

This is scaled relative to the data luminosity ($20.3\,\text{fb}^{-1}$) to obtain an MC scale factor for each sample, where:

$$\text{MC scale factor} = \frac{\text{data luminosity}}{\text{MC\_}\mathcal{L}} \tag{4.6}$$

For each MC event a Pileup Weight, z Vertex Weight, Trigger Weight and Muon

Process	DSID	$\sigma\times$ BR(pb)	k-factor	Notes
Alpgen+Herwig/Jimmy W+jets → $e\nu$	107680	8036.2	1.1760	0-jet
	107681	1579.5	1.1760	1-jet
	107682	477.31	1.1760	2-jet
	107683	133.89	1.1760	3-jet
	107684	35.614	1.1760	4-jet
	107685	10.545	1.1760	5-jet
Alpgen+Herwig/Jimmy W+jets → $\tau\nu$	107700	8036.2	1.1760	0-jet
	107701	1579.5	1.1760	1-jet
	107702	477.50	1.1760	2-jet
	107703	133.78	1.1760	3-jet
	107704	35.593	1.1760	4-jet
	107705	10.534	1.1760	5-jet
Alpgen+Herwig/Jimmy Z+jets → ee	107650	711.76	1.2290	0-jet
	107651	155.20	1.2290	1-jet
	107652	48.739	1.2290	2-jet
	107653	14.222	1.2290	3-jet
	107654	3.7471	1.2290	4-jet
	107655	1.0942	1.2290	5-jet
Alpgen+Herwig/Jimmy Z+jets → $\mu\mu$	107660	712.06	1.2290	0-jet
	107661	154.78	1.2290	1-jet
	107662	48.884	1.2290	2-jet
	107663	14.196	1.2290	3-jet
	107664	3.8024	1.2290	4-jet
	107665	1.1094	1.2290	5-jet
Alpgen+Herwig/Jimmy Z+jets → $\tau\tau$	107670	711.89	1.2290	0-jet
	107671	155.09	1.2290	1-jet
	107672	48.805	1.2290	2-jet
	107673	14.140	1.2290	3-jet
	107674	3.7711	1.2290	4-jet
	107675	1.1122	1.2290	5-jet
MC@NLO+Herwig $t\bar{t}$	105200	112.94	1.2158	
AcerMC+Pythia Single Top	117360	8.5878	1.1037	
	117361	8.5889	1.1035	
	117362	8.5810	1.1045	
Herwig Diboson WW	105985	12.416	1.6833	semileptonic, filtered for one lepton
Herwig Diboson ZZ	105986	0.99081	1.5496	semileptonic, filtered for one lepton
Herwig Diboson WZ	105987	3.6706	1.9011	semileptonic, filtered for one lepton

Table 4.5: MC backgrounds for the $W \rightarrow \mu\nu$ process.

Efficiency Weight are also determined using ATLAS calibration software. The product of these along with the MC Scale factor is calculated and applied to each MC variable of interest. The p_{T} of each muon is also adjusted or ‘smeared’ on a per variable basis using the calibration software.

4.4 Event selection

This section describes the details of how candidate particles are selected. Figure 4.4 shows an example of a candidate $J/\psi + W^{\pm}$ event that was reconstructed by the ATLAS detector.

4.4.1 Trigger

Candidate events are preferentially triggered by a high p_{T} muon from the $W^{\pm} \to \mu^{\pm}\nu$ decay rather than by muons from the J/ψ decay, which tend to be lower p_{T}. Events are collected by two triggers requiring either at least one tight[5] isolated[6] muon with $p_{\mathrm{T}} > 24\,\mathrm{GeV}$ or at least one tight muon of $p_{\mathrm{T}} > 36\,\mathrm{GeV}$. Their names are *EF_mu24i_tight* and *EF_mu36_tight* respectively. These triggers are highly efficient at collecting $W^{\pm} \to \mu^{\pm}\nu$ decays and are not prescaled[7]. The use of triggers enforces high data quality requirements and excludes events recorded during temporary faults in the detector systems that could compromise the data.

---

[5] A tight muon is one with a three station coincidence in the level one trigger in the muon spectrometer.

[6] An isolated muon is one where the ratio of the total transverse momentum in a cone of radius $\Delta R = \sqrt{\Delta\eta^2 + \Delta\phi^2} = 0.2$ around the muon track to the total muon transverse momentum is less than 0.12, i.e., pTcone20/pT(muon) < 0.12.

[7] Prescaling means only some fraction of the events that pass the trigger are actually recorded.

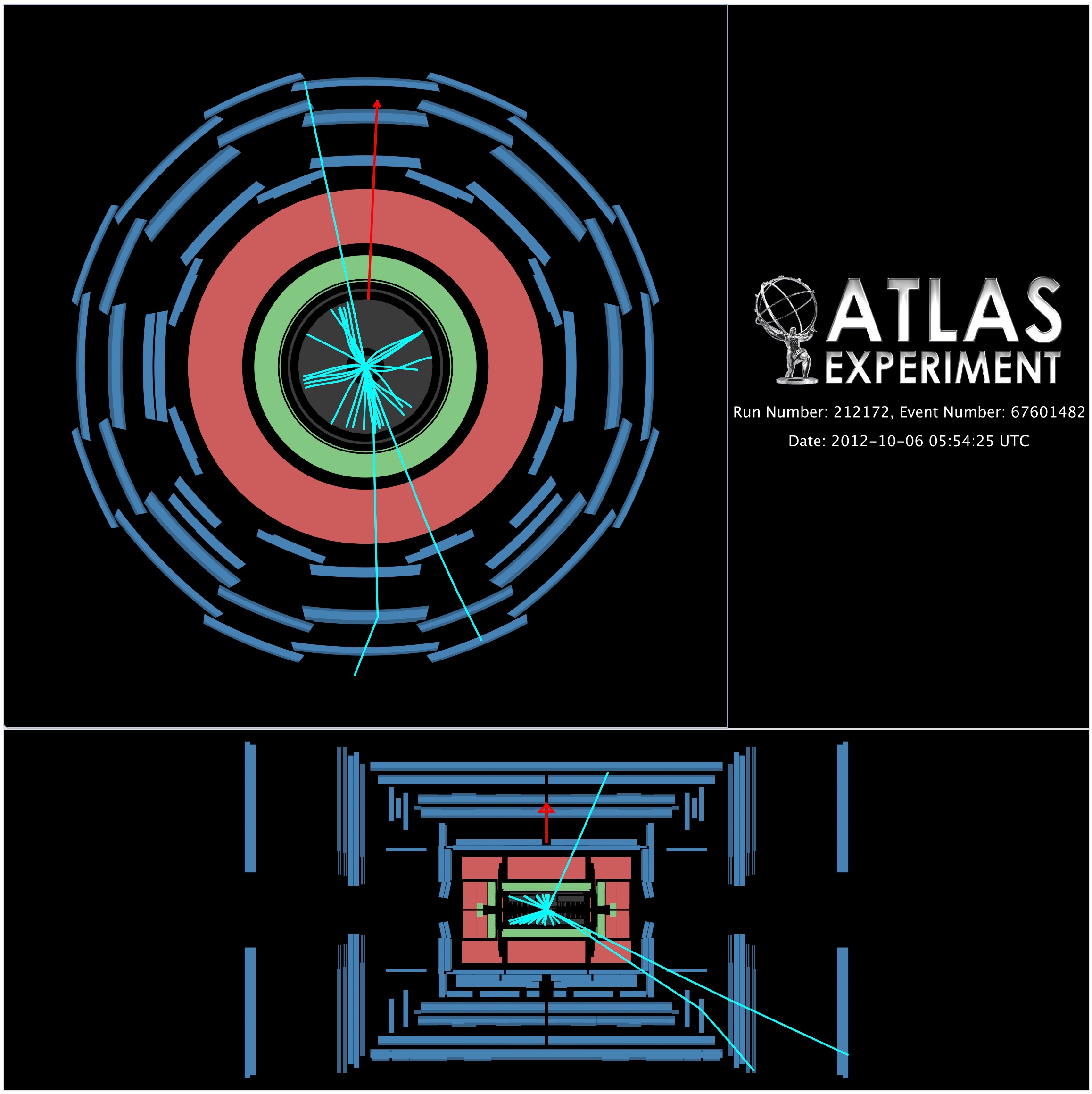

Figure 4.4: A representative $pp \to J/\psi + W^{\pm} \to \mu^{+}\mu^{-}, \mu^{\pm}\nu$ candidate event recorded with the ATLAS detector at $\sqrt{s} = 8$ TeV during data taking in 2012. The muon tracks are shown with solid blue lines and the missing transverse energy vector is shown with a red arrow.

4.4.2 Vertex

The candidate primary hard scattering pp collision vertex is chosen as the reconstructed vertex with the highest total transverse momentum ($\Sigma p_{\mathrm{T}}^{2}$) of associated tracks. The point of closest approach for the J/ψ muon candidate tracks to this vertex is required to be within 10 mm along the beam axis (in the z-direction).

4.4.3 $J/\psi \rightarrow \mu\mu$ requirements

One pair of oppositely-charged muons is required to form a J/ψ candidate. At least one muon must have $p_{\mathrm{T}} > 4\,\mathrm{GeV}$, and at least one must be a combined muon. A vertex fit is performed on the muon tracks to constrain them to originate at a common point, this may slightly modify the track parameters. The invariant mass of the di-muon system calculated with the modified track parameters must be with in the range $2.4 < m_{\mu^+\mu^-} < 3.8\,\mathrm{GeV}$. The J/ψ candidate is required to have transverse momentum satifying $p_{\mathrm{T}}^{J/\psi} > 8.5\,\mathrm{GeV}$ and rapidity satisfying $|y_{J/\psi}| < 2.1$. A full list of the J/ψ candidate selection requirements is given in Table 4.6.

In most events there is no suitable J/ψ candidate found. In the rare case that more than one J/ψ candidate from an event passes all selections[8], then the candidate with the lowest χ^2 value on the fit to the primary vertex is chosen. This maximizes the statistical likelihood of the J/ψ candidate to have originated at the primary vertex.

---

[8] 1% of passed events

J/ψ muon requirements	
Staco muons	
Pass muon combined performance (MCP) criteria	
Transverse momentum	$p_{\mathrm{T}} > 2.5$ GeV if $\|\eta\| > 1.3$
Transverse momentum	$p_{\mathrm{T}} > 3.5$ GeV if $\|\eta\| < 1.3$
Pseudorapidity	$\|\eta\| < 2.5$
Distance from primary vertex in z-direction	$\|z_o\| < 10mm$
Additional di-muon requirements	
Two combined muons or one combined muon and one segment-tagged muon	
Oppositely charged muons	
At least one combined muon with	$p_{\mathrm{T}} > 4$ GeV
Post-vertexing J/ψ Invariant Mass	$\in$ (2.4, 3.6) GeV
J/ψ transverse momentum	$p_{\mathrm{T}} > 8.5$ GeV
J/ψ rapidity	$\|y\| \in$ (0, 2.1)

Table 4.6: Requirements for the J/ψ candidates.

4.4.4 $W^{\pm} \rightarrow \mu^{\pm}\nu$ requirements

For the associated sample, after two muons have been combined to form a J/ψ candidate, any remaining muon that passes all selection criteria is combined with E_{T}^{miss} to form a $W^{\pm}$ candidate. This muon used to reconstruct a $W^{\pm}$ candidate is also required to be the muon that triggered the event, this is because trigger muons already satisfy certain standardized data quality criteria. It is required to have $p_{\mathrm{T}} > 25\,\mathrm{GeV}$ and $|\eta| < 2.4$ in order to be within the acceptance of the trigger. The $W^{\pm}$ muon must approach the primary vertex within 1 mm in the z-direction. The $W^{\pm}$ muon must have a transverse impact parameter significance (i.e. $d_0/\sigma(d_0)$) of less than three. It must also be isolated, where we define calorimetric and track isolation variables by calculating the sum of calorimeter cell E_{T} and track p_{T} respectively within a cone size $\sqrt{(\Delta\eta)^2 + (\Delta\phi)^2} = 0.3$ around the muon direction. The energy deposited by the muon is subtracted from the calorimetric isolation, and only tracks compatible with originating at the primary vertex and with $p_{\mathrm{T}} > 1$ GeV (excluding the muon itself) are considered for the track isolation. A correction depending on the number of reconstructed vertices is made to the calorimetric isolation to account for additional energy deposits due to pileup vertices. For the muon to be considered isolated, the energy and momentum of other objects in the cone around the muon track (as defined above) must both be less than 5% of the muon p_{T}. In the rare case that more than one $W^{\pm}$ candidate passes all selection criteria[9], the $W^{\pm}$ reconstructed from the muon with the highest p_{T} is selected. This follows the method used by reference [43].

---

[9] 1.83% of passed associated events

The $W^{\pm}$ boson transverse mass is defined as

$$m_{\mathrm{T}}(W) \equiv \sqrt{2p_{\mathrm{T}}(\mu)E_{\mathrm{T}}^{\mathrm{miss}}(1-\cos(\phi^{\mu}-\phi^{\nu}))} \tag{4.7}$$

and must be greater than 40 GeV, where $E_{\mathrm{T}}^{\mathrm{miss}}$ must be greater than 20 GeV and ϕ^{μ} and ϕ^{ν} represent the azimuthal angles of the muon and the $E_{\mathrm{T}}^{\mathrm{miss}}$(neutrino) from the $W^{\pm}$ boson decay respectively. We calculate the $W^{\pm}$ transverse mass because we do not have the complete information available to reconstruct the invariant mass. For reasons discussed in Section 3.5, only the transverse component of the missing energy, and thus the neutrino, is known. A full list of $W^{\pm}$ selection requirements is listed in Table 4.7.

To generate the inclusive sample, the same unfiltered data set that is used for the associated production is processed in parallel only applying the $W^{\pm} \rightarrow \mu^{\pm}\nu$ boson selection criteria listed in Table 4.7.[10] All but one of the known physics backgrounds for this physics process can be modeled using MC samples. The exception being the QCD/Multijet background which is too computationally intensive. The MC samples for the backgrounds and for the signal are processed in the same way as the data to get a complete model. Figure 4.5 shows how the inclusive $m_{\mathrm{T}}(W)$ derived from data and the model derived from MC samples compare with each other. The invariant $W^{\pm}$ mass would be expected to peak around the known value of 80.4 GeV [9]. Since we reconstruct the transverse mass it peaks at a lower value, as expected. The large spread in the figure is due to the poor E_{T}^{miss} resolution because of a large number of multiple proton-proton interactions (pileup).

---

[10] More than one $W^{\pm}$ candidate passes all cuts on 0.58% of passed inclusive events.

Subtracting the modelled backgrounds from the data yields $(5.21285 \pm 0.00135)\times 10^7$ events in the inclusive $W^\pm$ sample, where the statistical uncertainty has been determined by propagating the statistical errors from each histogram when performing the subtraction.

The agreement between the data and the model shows some disagreement, in particular for high values of $m_{\mathrm{T}}(W)$. This disagreement has been observed for some time and has been traced to the calculation of E_{T}^{miss}. ATLAS software uses many methods to calculate E_{T}^{miss} and we have used the method that gives the best match, and a method that gives a better one has not been identified. A systematic uncertainty is determined to account for this disagreement between the model and the data. It is a small effect compared to other larger sources of uncertainty, such as the unknown J/ψ spin alignment. This and other sources of uncertainty are discussed later.

4.4.5 J/ψ pseudo-proper time

In order to distinguish prompt J/ψ candidates from those originating from B hadron decay (non-prompt), we separate the primary vertex and the J/ψ decay vertex using pseudo proper time:

$$\tau \equiv L_{xy}\frac{m_{\mu^+\mu^-}}{p_{\mathrm{T}}^{J/\psi}} \equiv \frac{\vec{L}\cdot\vec{p}_{\mathrm{T}}^{J/\psi}}{p_{\mathrm{T}}^{J/\psi}}\cdot\frac{m_{\mu^+\mu^-}}{p_{\mathrm{T}}^{J/\psi}} \tag{4.8}$$

where $\vec{L}$ is the displacement of the J/ψ decay vertex from the event primary vertex and $m_{\mu^+\mu^-}$ is the invariant mass of the J/ψ candidate. Prompt J/ψ candidates will have a pseudo proper time consistent with zero.

$W^{\pm} \to \mu^{\pm}\nu$ muon requirements	
Fire trigger: *EF_mu24i_tight* OR *EF_mu36_tight*	
Trigger muon and $W^{\pm} \to \mu^{\pm}\nu$ candidate muon are the same	
Staco muon	
Combined muon	
Pass muon combined performance (MCP) criteria	
Transverse Momentum	$p_{\mathrm{T}} > 25\,\mathrm{GeV}$
Pseudorapidity	$\lvert\eta\rvert < 2.4$
Distance from primary vertex in z-direction	$\lvert z_0\rvert < 1\ mm$
Impact parameter significance	$\lvert d_0\rvert < 3\,\sigma_{d_0}$
Track isolation momentum in cone of $\Delta R < 0.3$	$< 0.05\,p_{\mathrm{T}}$
Calorimeter isolation energy in cone of $\Delta R < 0.3$	$< 0.05\,p_{\mathrm{T}}$
Neutrino (E_{T}^{miss}) Requirements	$E_{\mathrm{T}}^{miss} > 20\,\mathrm{GeV}$
$W^{\pm}$ Transverse Mass	$M_{\mathrm{T}}(W) > 40\,\mathrm{GeV}$

Table 4.7: Requirements for the $W^{\pm}$ Boson

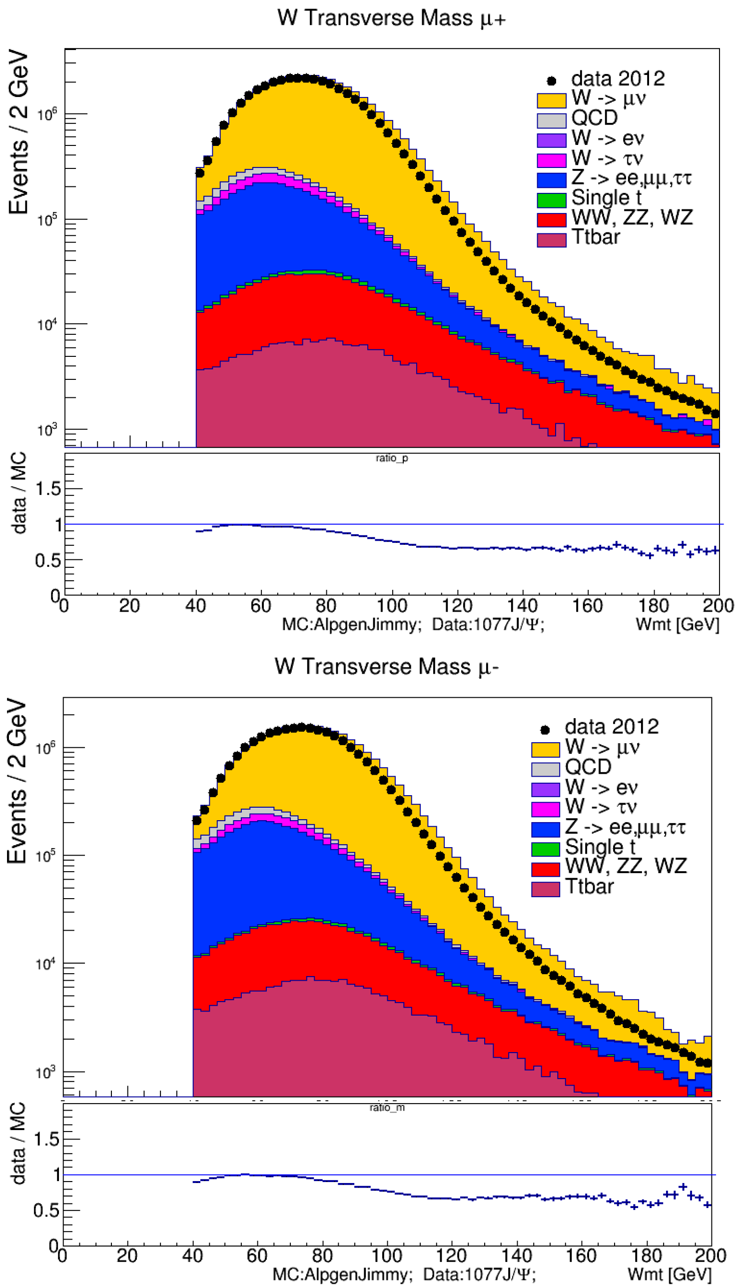
W Transverse Mass μ+

W Transverse Mass μ-

Figure 4.5: W transverse mass for (a) positive and (b) negative W boson candidates. Where the $W \rightarrow \mu\nu$ is MC signal and the other samples are backgrounds. The QCD sample is generated using a data driven method and the other backgrounds are from MC.

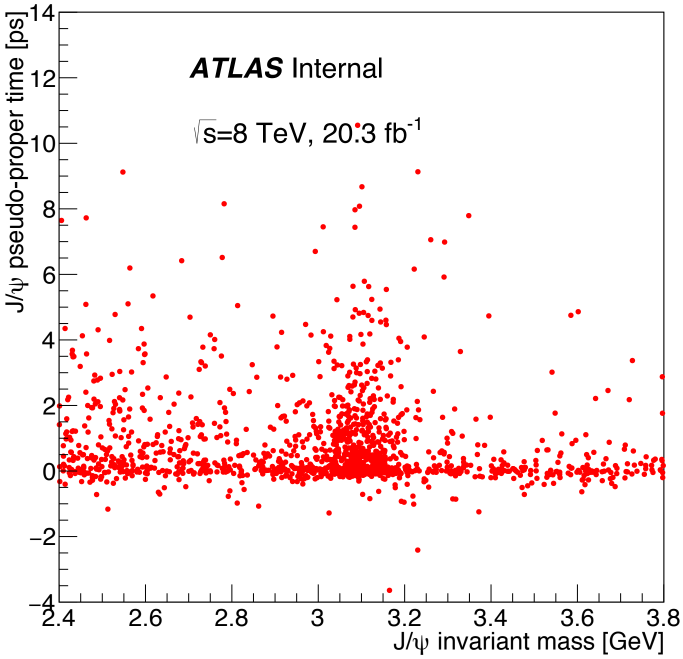

Figure 4.6: Distribution of J/ψ candidates after selection criteria.

4.4.6 $J/\psi + W^{\pm}$ signal extraction

As previously discussed, each candidate muon in an event is combined with each muon of opposite sign in the same event to make J/ψ candidates. This is first performed without any other selection criteria, so this results in many misidentified J/ψ candidates from random combinations of muons (combinatorics). After the selection criteria in Table 4.6 are applied, the remaining candidates are distributed as shown in Figure 4.6.

These remaining candidates are assigned weights in order to distinguish true J/ψ events from the combinatorics. The discriminating variable for this process is the J/ψ invariant mass, with true J/ψ events having an invariant mass consistent with the J/ψ

mass peak. Candidates are simultaneously separated into those originating from the primary vertex (prompt) and those originating from a subsequent decay (non-prompt). The discriminating variable for this separation is the J/ψ pseudo-proper time, where prompt candidates have a pseudo-proper time consistent with zero.

Using this *simultaneous* two-dimensional mass and lifetime fit, the J/ψ candidates are placed into one of four groups: prompt events, prompt background events, non-prompt events and non-prompt background events. The fit model used is a two-dimensional unbinned extended maximum likelihood fit in J/ψ mass and pseudo-proper time. To perform the fits and normalize the probability density functions to unity we use the Roofit statistical toolkit [52], which takes into account the uncertainties on the mass and lifetime of the candidates. To assign weights to the prompt J/ψ, non-prompt J/ψ and their backgrounds we use the sPlot procedure [44].

Events that fall into the prompt event group (and not in the prompt background group) are considered signal candidates. A total event weight is calculated for each prompt J/ψ signal candidate using the formula

$$\text{Weight} = \frac{1}{J/\psi\text{acceptance} \times \mu^{+}\text{efficiency} \times \mu^{-}\text{efficiency}} \tag{4.9}$$

The maps used to to find the acceptance and efficiency weights are shown in Figures 4.8 and 4.9. The methods used to generate them are discussed in Sections 4.4.7 and 4.4.8.

After the fit is performed, the sPlot tool is used in order to extract per-event weights according to the parameters of the fit model. These weights can be further applied to other variables like the $W^{\pm}$ transverse mass and the J/ψ transverse momentum.

4.4.7 J/ψ spin-alignment and acceptance

J/ψ particles can be produced with various polarizations, leading to an angular distribution of spin alignments, which affects their acceptance. In general the spin-alignment profile for associated quarkonia production at the LHC is unknown, so we do not know what fraction of J/ψ mesons is produced in each different polarization state. It has been measured for inclusive J/ψ production, but there is not enough data to measure it for $J/\psi + W^{\pm}$ production. There is no reason to assume that it would be the same in these two cases. Since this is unknown, we simulate the probability that a J/ψ of a given transverse momentum and rapidity is reconstructable for five different spin alignment scenarios and generate an acceptance map for each scenario. Each J/ψ candidate is given a nominal weight based on its transverse momentum and rapidity, and then four alternate weights. The maximum difference between the results obtained by using the nominal map and one of the alternate maps contributes to the total systematic uncertainty. The nominal model assumes isotropic alignment, while the alternate maps cover other alignment perturbations.

The angular distribution for the $J/\psi \rightarrow \mu^+\mu^-$ decay in the J/ψ decay frame is:

$$\frac{d^2N}{d\cos\theta^{\star} d\phi^{\star}} \propto 1 + \lambda_{\theta}\cos\theta^{\star 2} + \lambda_{\phi}\sin\theta^{\star 2}\cos 2\phi^{\star} + \lambda_{\theta\phi}\sin 2\theta^{\star}\cos\phi^{\star}, \tag{4.10}$$

where the angular variables are defined in Figure 4.7. The terms $\lambda_{\theta}, \lambda_{\phi}$ and $\lambda_{\theta\phi}$ are the coefficients of each angular term. They can take values in $\in (-1, 1)$, which covers the whole allowed phase space.

We take the following polarization states into account:

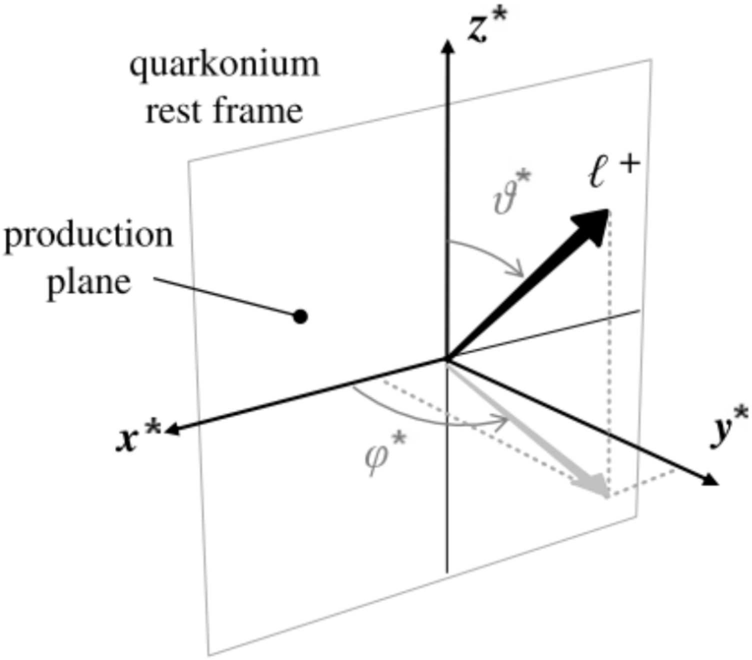

Figure 4.7: Defines the J/ψ spin alignment angles in the J/ψ decay frame. The $z^* - axis$ is the J/ψ line of flight and the $x^* - z^*$ plane is the J/ψ production plane. θ^* is the angle between the direction of the positive muon momentum and the J/ψ line of flight. ϕ^* is the angle between the J/ψ production plane and the decay plane formed by the direction of the J/ψ and the positive muon. [43]

1. Isotropic distribution, independent of $\theta^\star$ and $\phi^\star$, with $\lambda_\theta = \lambda_\phi = \lambda_{\theta\phi} = 0$. This is used for the nominal measurement.

2. Full longitudinal alignment with λ_θ =-1, $\lambda_\phi = \lambda_{\theta\phi} = 0$.

3. Transverse-0 alignment with λ_θ =+1, $\lambda_\phi = \lambda_{\theta\phi} = 0$.

4. Transverse-M alignment with λ_θ =+1, λ_ϕ =-1, $\lambda_{\theta\phi} = 0$.

5. Transverse-P alignment with $\lambda_\theta = \lambda_\phi$ =+1, $\lambda_{\theta\phi} = 0$.

The acceptance maps generated using these five conditions are shown in Figure 4.8. They are used to find the polarization weight for a given J/ψ candidate. Studies show that J/ψ acceptance can fall below 30% for $p_{\mathrm{T}}^{J/\psi} < 8.5$ GeV or $|y| > 2.1$. So we require J/ψ candidates of p_{T} >8.5 GeV and $|y| < 2.1$ to remove large corrections from our measurement.

4.4.8 J/ψ muon reconstruction efficiency

The transverse momentum and pseudo rapidity of the two muons combined to form J/ψ candidates effects their reconstruction efficiency, so a weight is applied to each muon based on its η and p_{T} to correct for this. The maps used for these weights are derived from a data-driven tag and probe [53] method and are shown in Figure 4.9. The method first searches for an Inner Detector track, called the probe, and then matches it with a well reconstructed muon, called the tag. This allows the generation of an unbiased sample of muons. The systematic uncertainty in this weight is estimated

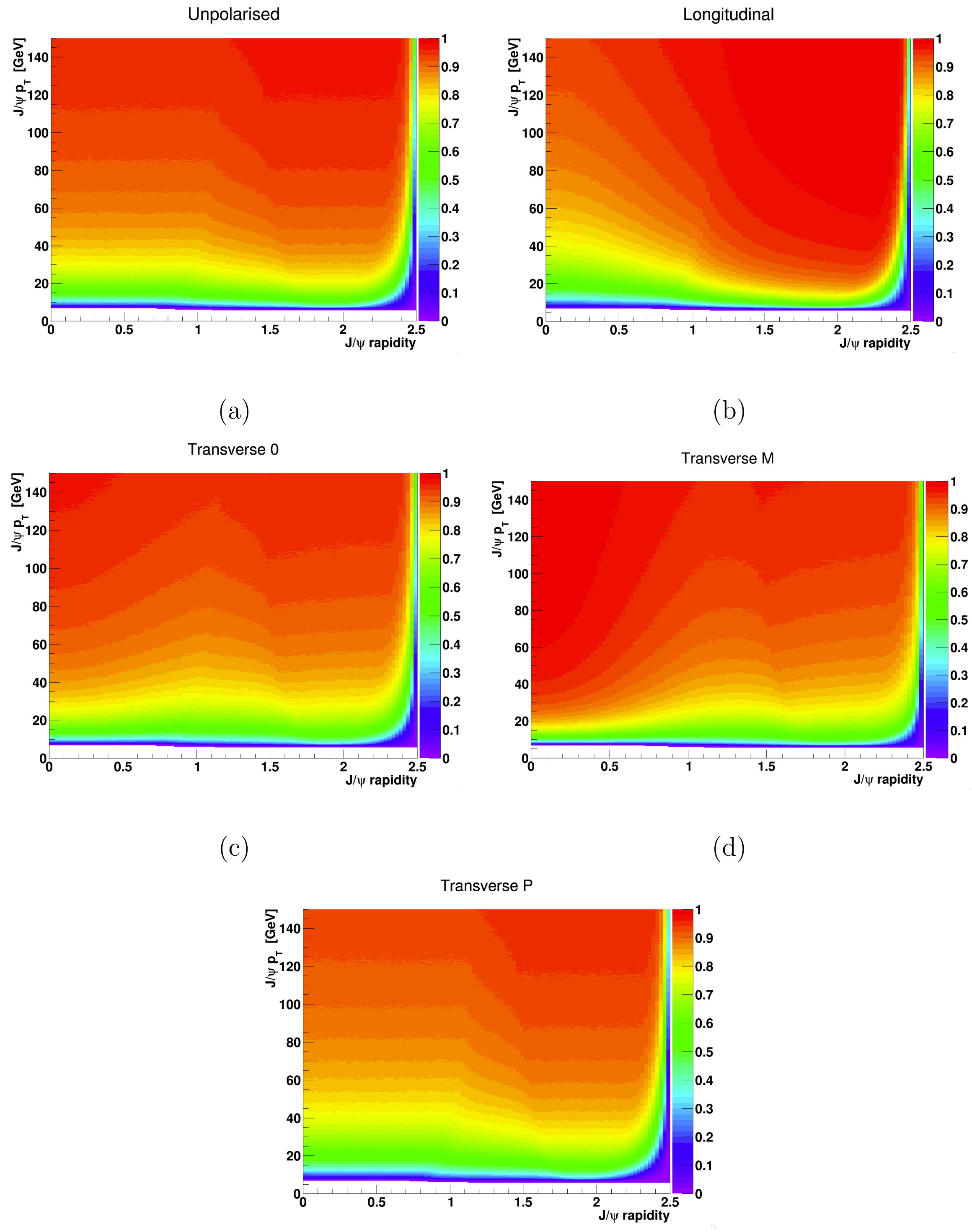

Unpolarised

Longitudinal

Transverse 0

Transverse M

Transverse P

(a)

(b)

(c)

(d)

(e)

Figure 4.8: Simulated J/ψ polarization maps for (a) unpolarized (b) longitudinal (c) transverse O (d) transverse M and (e) transverse P scenarios.

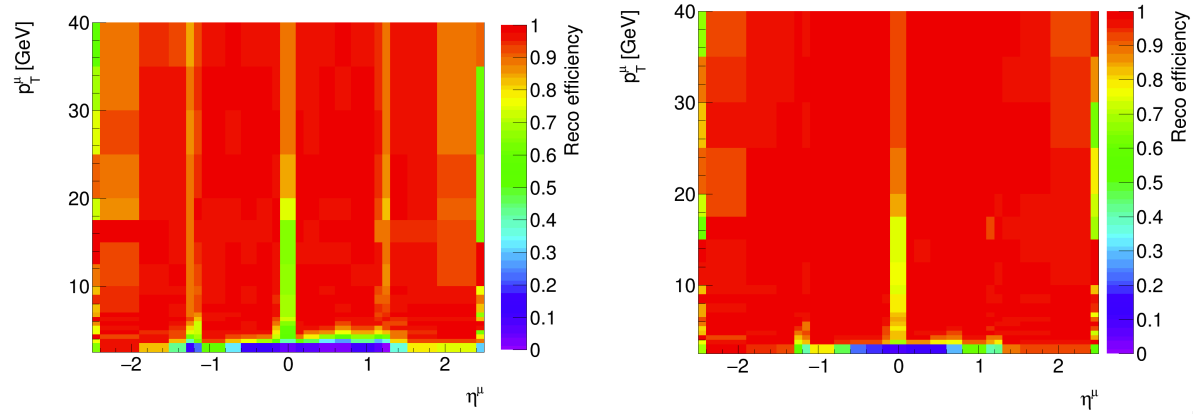

(a) (b)

Figure 4.9: Muon efficiency maps for (a) combined muons and (b) segment-tagged muons.

by randomly sampling a gaussian distribution about the nominal weight, which contributes to the total systematic uncertainty.

4.5 Backgrounds

All but one of the known physics backgrounds in the inclusive $W^\pm$ selection are determined by processing the MC samples listed in Table 4.5 in the same way as data. These events are then scaled (as described previously) and subtracted from the data. For the QCD/Multijet background a data driven ABCD method is used. For the backgrounds in the associated $J/\psi + W^\pm$ selection either the MC samples for a process are not available, or another method of background removal is more effective. The methods used for background estimation and removal are described below.

Region	$E_{\mathrm{T}}^{\mathrm{miss}}$	$m_{\mathrm{T}}(\mathrm{W})$	Lepton Isolation Criteria
A	$< 20\,\mathrm{GeV}$	$< 40\,\mathrm{GeV}$	isolated
B	$< 20\,\mathrm{GeV}$	$< 40\,\mathrm{GeV}$	anti-isolated
C	$> 20\,\mathrm{GeV}$	$> 40\,\mathrm{GeV}$	isolated
D	$> 20\,\mathrm{GeV}$	$> 40\,\mathrm{GeV}$	anti-isolated

Table 4.8: ABCD method categories.

4.5.1 QCD/Multijet

A muon from a hadronic QCD or multijet process can be misidentified as coming from a $W^{\pm} \to \mu^{\pm}\nu$ process. Hadronic decays not well modelled with Monte Carlo methods, so a data driven ABCD method is used to estimate this background. This ABCD method alone is used to estimate the background in the inclusive $W^{\pm}$ production and a modified ABCD + sPlot method for the associated $J/\psi + W^{\pm}$ production. Because an isolation trigger is used in the analysis this has the effect of providing an upper limit on the QCD background estimation rather than an absolute value because the ABCD method employs comparative ratios.

To begin with, the data are separated into four regions based on three orthogonal selection criteria seen in Table 4.8.

In general this method assumes that the following ratios of the number of events in each region are equivalent: $\frac{D}{B} \equiv \frac{C}{A}$. Then the QCD contamination of the signal region (C) is given by

$$\frac{A \times D}{B}. \tag{4.11}$$

However, because our data selections require an isolated muon in the trigger we need to use a modified formula. A test shows that 99% of muons pass both the *EF_mu24i_tight* and *EF_mu36_tight* triggers, so almost all of the muon candidates already have an isolation cut applied to them due to the trigger used. This has the effect of modifying the number of events in regions B and D by factors F_b and F_d respectively due to the isolation cut. Giving the new relationship $\frac{D \times F_d}{B \times F_b} \equiv \frac{C}{A}$ and the new formula for the QCD contamination as

$$\frac{A \times D}{B} \times \frac{F_d}{F_b}. \tag{4.12}$$

Figure 4.10 shows the ratio of the number of events in isolated to anti-isolated regions as a function of $m_{\mathrm{T}}(W)$. Because the curve is not flat we see that the isolation trigger removes more events from region B than from region D, and conclude that $F_d > F_b$. Thus this method gives an upper limit or overestimation of the QCD contamination.

We do not assume that the QCD contamination is independent of $\mu_{p_{\mathrm{T}}}(W^{\pm})$. The $W^{\pm}$ muons are binned by transverse momentum and the QCD contamination is calculated independently for each bin. For the inclusive $W^{\pm}$ sample this bin size is 5 GeV. For the associated $J/\psi + W^{\pm}$ sample variable bin sizes that sufficient statistics in each bin are used.

For the inclusive $W^{\pm}$ sample, this QCD background is added to the rest of the MC generated backgrounds, see Figure 4.5. Then all the backgrounds are subtracted from data events. This provides the final corrected number of inclusive $W^{\pm}$ bosons.

To determine the QCD background in the associated $J/\psi + W^{\pm}$ sample, a modified ABCD+sPlot method is used. $m_{\mathrm{T}}(W)$ prompt events from Region D data are separated

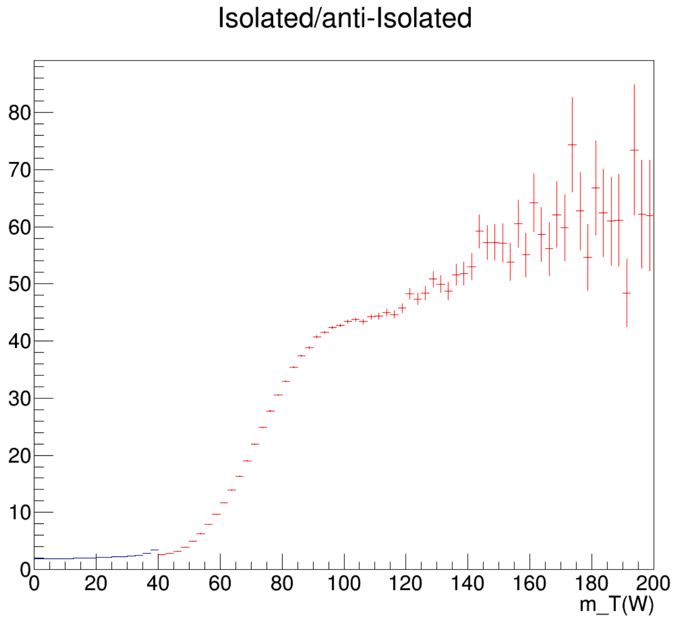

Figure 4.10: The ratio of isolated to anti-isolated regions. Region 0< $m_T(W^{\pm})$ <40 shows A/B (in blue) and region 40< $m_T(W^{\pm})$ <200 shows C/D (in red).

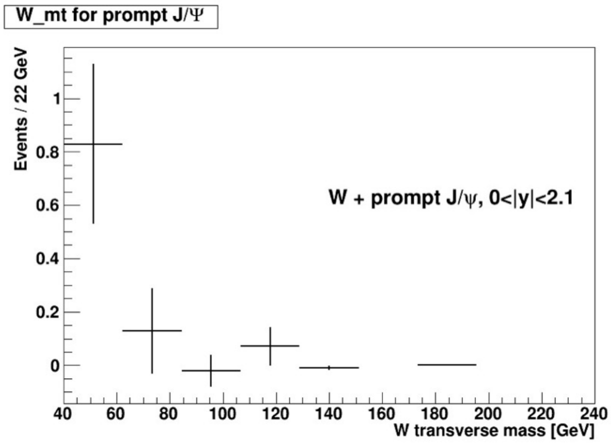

Figure 4.11: $m_{\mathrm{T}}(\mathrm{W})$ candidates from Region D data associated with prompt J/ψ events.

using sPlot into those associated with prompt or non-prompt J/ψ particles (and their backgrounds), an example is seen in Figure 4.11. Then Equation 4.13 is used to give an estimation of the percentage of $W^{\pm}$ bosons arising from QCD events that are contaminating the signal sample. This percentage is $0.8^{+0.4}_{-0.8}\%$, corresponding to $3.5^{+1.7}_{-3.5}$ events.

$$\text{QCD fraction} = \frac{\#\text{ of events in region A}}{\#\text{ of events in region B}} \times \frac{\#\text{ of events in region D}}{\#\text{of signal events}} \tag{4.13}$$

These background events must be subtracted from the prompt J/ψ candidate events, but the background events are not evenly distributed in $p_{\mathrm{T}}^{J/\psi}$, as seen in Figure Figure 4.12. So weighting by the bin size and this p_{T} distribution gives Table 4.9, i.e. the fractional distribution of these 3.5 QCD events across the $p_{\mathrm{T}}^{J/\psi}$ bins.

Even the maximum estimated background is so negligible that the uncertainty that this introduces is outweighed by uncertainties from other sources such as the unknown J/ψ spin alignment. A template method was also explored to estimate the QCD background in the inclusive $J/\psi + W^{\pm}$ sample. The results given by this method are

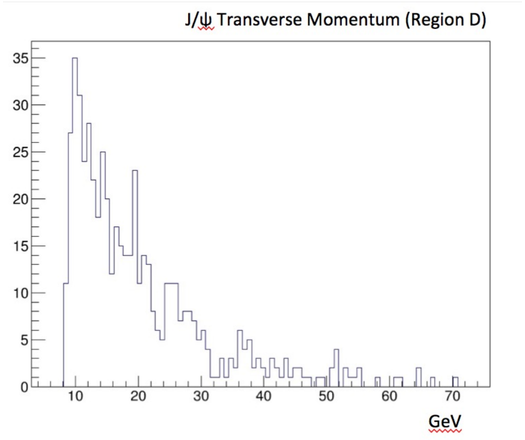

Figure 4.12: The transverse momentum distribution of J/ψ events in data region D.

$p_{\mathrm{T}}^{J/\psi}$ Bin	QCD Fraction Distribution
8.5 - 10	0.135
10 - 14	0.194
14 - 18	0.138
18 - 30	0.279
30 - 60	0.214
60 - 150	0.041

Table 4.9: The fractional distribution of the QCD background events across the $p_{\mathrm{T}}^{J/\psi}$ bins, the table adds up to 1. The total number of events due to QCD contamination (3.5) is divided up according to this table to give the number of candidate events to be subtracted from each $p_{\mathrm{T}}^{J/\psi}$ bin before the final cross section is calculated.

consistent with those from the ABCD method, but they have such large uncertainties that this second method is not implemented.

4.5.2 $t\bar{t}$ decays

Top decays almost exclusively to $W^{\pm}$ and b, and b can decay into $J/\psi + X$. Since these J/ψ candidates tend to be non-prompt they are separated out from the prompt signal by using the two-dimensional mass and lifetime fit. Tests verified that the fit removes all of these backgrounds from the prompt sample and the estimated $t\bar{t}$ contamination is zero.

4.5.3 Pileup

We are interested in events where the J/ψ and $W^{\pm}$ are produced in the same pp collision, not in two different collisions (these are called pileup interactions). The number of pileup interactions increased in 2012 compared with previous runs due to the higher luminosity. The J/ψ and $W^{\pm}$ candidates are already constrained to be close to the primary vertex, meaning they are also close to each other, thus reducing the effect of pileup.

A statistical method also used by a related analysis [54] is used to estimate additional pileup background not removed by the $z-$vertex cut. We start with direct measurements of the $J/\psi \rightarrow \mu^{+}\mu^{-}$ cross-section [43] performed by another analysis. However, the cross-sections in some p_{T} and y ranges were not measured. So first we extrapolate the values for these ranges from the measured results. For the range

$8.5 < p_{\mathrm{T}} < 10\,\mathrm{GeV}$ with $0.75 < y < 2.00$ both a double and triple exponential fit are used, with the difference between them giving a systematic error. The same method is used for the range $110 < p_{\mathrm{T}} < 150\,\mathrm{GeV}$ with $0.00 < y < 2.00$. These plots are seen in Figures B.2 and B.3. For the range $8.5 < p_{\mathrm{T}} < 150\,\mathrm{GeV}$ with $2.00 < y < 2.10$ a value of 10% of the value of the range $0.00 < y < 2.00$ is used. This seems a reasonable extrapolation because the cross section is almost flat in y as shown in Figure B.1. The extrapolated values are all listed in Tables B.1, B.2 and B.3.

Next, a luminosity-weighted distribution of $<\mu>$ (the mean number of collisions per bunch crossing) from the standard MC pileup reweighting mechanism is needed. This is generated by sampling a distribution of a toy Monte Carlo to estimate pileup events in rapidity and p_{T} bins of interest. Figures B.4 and B.5 illustrate this process and arrive at an average number of extra vertices, $n^{\mathrm{extra}}_{\mathrm{vertex}} \approx 2.3 \pm 0.2$.

The yield of the inclusive $W^{\pm}$ sample is also used. The calculation of the estimated number of pileup events in each J/ψ p_{T} bin is shown in Table 4.10. Column two values are mostly direct measurements, with some extrapolations. Column three is derived by multiplying column two by $n^{\mathrm{extra}}_{\mathrm{vertex}} \approx 2.3 \pm 0.2$ and dividing by the inclusive cross section ($0.73{\times}10^{-8}$ b). Column four is derived by dividing column three by the absolute rapidity width. Column five shows the average acceptance × efficiency from inclusive J/ψ in each bin. Column six is the product of columns three, five and the inclusive W yield. The total estimated number of pileup events are is subtracted from the yield.

Bin $\mid y \mid \times p_{\mathrm{T}}$	$\sigma(J/\psi \to \mu\mu)\,\mathrm{nb}$	$n_{\mathrm{vertex}}^{\mathrm{extra}}\sigma_{\mathrm{bin}}/\sigma_{\mathrm{incl}}(10^{-8})$	$\frac{1}{\sigma_{\mathrm{bin}}}\frac{\mathrm{d}^2\sigma}{\mathrm{d}y\mathrm{d}p_{\mathrm{T}}}(10^{-8})$	$\langle\epsilon \times A\rangle$	Expected yield
$(0,1) \times (8.5,10)$	5.985 ± 0.166	18.364 ± 1.359	6.121 ± 0.453	0.23	2.202 ± 0.163
$(0,1) \times (10,14)$	4.585 ± 0.092	14.070 ± 1.044	1.759 ± 0.130	0.39	2.860 ± 0.212
$(0,1) \times (14,18)$	0.956 ± 0.020	2.933 ± 0.218	0.367 ± 0.027	0.53	0.810 ± 0.060
$(0,1) \times (18,30)$	0.434 ± 0.008	1.331 ± 0.098	0.055 ± 0.004	0.65	0.451 ± 0.033
$(0,1) \times (30,60)$	0.050 ± 0.001	0.154 ± 0.011	0.003 ± 0.000	0.73	0.058 ± 0.004
$(0,1) \times (60,150)$	0.002 ± 0.000	0.008 ± 0.001	0.000 ± 0.000	0.84	0.003 ± 0.000
$(1,2.1) \times (8.5,10)$	6.008 ± 0.119	18.436 ± 1.366	2.095 ± 0.155	0.39	3.748 ± 0.278
$(1,2.1) \times (10,14)$	5.232 ± 0.097	16.055 ± 1.184	1.824 ± 0.135	0.49	4.101 ± 0.303
$(1,2.1) \times (14,18)$	0.996 ± 0.018	3.056 ± 0.225	0.347 ± 0.026	0.63	1.004 ± 0.074
$(1,2.1) \times (18,30)$	0.425 ± 0.006	1.304 ± 0.095	0.049 ± 0.004	0.73	0.496 ± 0.036
$(1,2.1) \times (30,60)$	0.043 ± 0.001	0.133 ± 0.010	0.002 ± 0.000	0.74	0.051 ± 0.004
$(1,2.1) \times (60,150)$	0.002 ± 0.000	0.006 ± 0.000	0.000 ± 0.000	0.81	0.002 ± 0.000
				Total:	15.788 ± 0.502

Table 4.10: Pileup background estimation.

4.5.4 B$_c$ decays

The $B_c^{\pm} \rightarrow J/\psi l^{\pm} \nu X$ process can mimic our associated signal, where X is any neutral particle. To examine the possible $B_c \rightarrow J/\psi \mu \nu X$ decay background, the invariant mass of the three leptons used to form the J/ψ and $W^{\pm}$ candidates is calculated and shown Figure 4.13. The first bin not consistent with zero has 6 ± 2.45 events of mass 6.65 ± 0.7 GeV. The mass of B_c is 6.277 ± 0.006 GeV. For this background to be present our three lepton mass must be less than the B_c mass in order to account for the missing transverse energy and X particle mass. So we conclude that the B_c background is unlikely to be present.

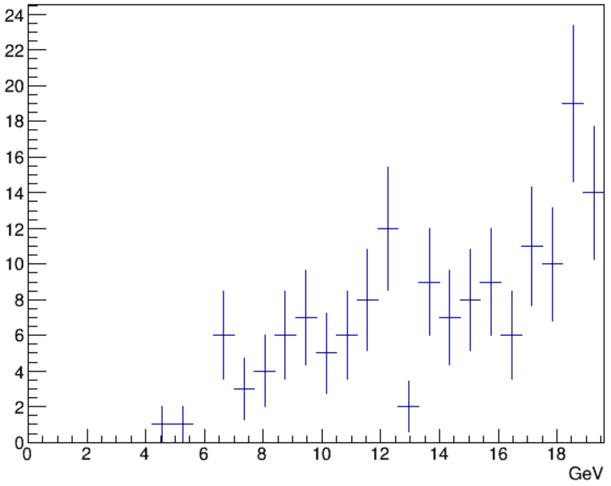

Figure 4.13: The invariant mass of the W muon and the two J/ψ muons.

4.6 Double parton scattering estimation

An interesting question is to ask what number of events is caused by double parton scattering (DPS) as opposed to single parton scattering (SPS). Additionally, this is a useful exercise since we include DPS as part of the signal. The method outlined below estimates that $8.8 \pm 1.5\%$ of the signal yield in the associated-production $W +$ prompt J/ψ sample is due to DPS interactions.

We use a method very similar to the method for estimating background accounted for by pileup interactions. To make this estimation we use the effective cross-section for double parton interactions measured by ATLAS for $W + 2-$jet events, $\sigma_{\text{eff}} = 15 \pm 3\,(\text{stat.})^{+5}_{-3}\,(\text{sys.})$ mb [55], as well as the cross-sections for $pp \to J/\psi$ prompt and non-prompt. Based on the assumptions that the two hard scatters are uncorrelated and that σ_{eff} is process-independent, then the probability that a J/ψ and $W^{\pm}$ boson are both produced in the same event is

$$P^{ij}_{J/\psi|W} = \frac{\sigma_{J/\psi}}{\sigma_{\text{eff}}}. \tag{4.14}$$

Table 4.11 shows the method used for estimating this contribution. Column one shows the bin in $|y| \times p_{\text{T}}$ space of the J/ψ. Column two values are mostly direct measurements, with some extrapolations. Column three shows the probability that a J/ψ is produced in a particular $|y|$ and p_{T} bin, in association with a hard scattering that produces a W boson. The cross section σ_{eff} used in column 3 is taken from the ATLAS measurement of W + 2 jets, and is approximately equal to 15 mb. Column four shows the values of column three normalized by the size of the bin in the $|y| \times p_{\text{T}}$

space. Column five shows the average acceptance × efficiency from inclusive J/ψ in each bin. Column six shows the expected yield of DPS events. It is calculated from the product of the W candidates from our inclusive W sample, times the $< \epsilon \times \mathcal{A} >$, times the $\sigma_{\text{bin}}/\sigma_{\text{eff}}$. Uncertainties from the J/ψ cross-section at $\sqrt{s} = 8$ TeV, the number of inclusive $W^{\pm}$ events and the DPS effective cross-section contribute to the total uncertainty.

Bin $\mid y \mid \times p_{\mathrm{T}}$	$\sigma(J/\psi \to \mu\mu)$ nb	$\sigma_{\mathrm{bin}}/\sigma_{\mathrm{eff}}(10^{-8})$	$\frac{1}{\sigma_{\mathrm{bin}}}\frac{d^2\sigma}{\mathrm{d}y\mathrm{d}p_{\mathrm{T}}}(10^{-8})$	$\langle \epsilon \times A \rangle$	Expected yield
$(0,1) \times (8.5,10)$	5.985 ± 0.166	39.898 ± 15.446	13.698 ± 5.149	0.23	4.784±1.852
$(0,1) \times (10,14)$	4.585 ± 0.092	30.569 ± 11.836	3.821 ± 1.479	0.39	6.215±2.406
$(0,1) \times (14,18)$	0.956 ± 0.020	6.373 ± 2.468	0.797 ± 0.308	0.53	1.761±0.682
$(0,1) \times (18,30)$	0.434 ± 0.008	2.891 ± 1.119	0.120 ± 0.047	0.65	0.980±0.379
$(0,1) \times (30,60)$	0.050 ± 0.001	0.334 ± 0.129	0.006 ± 0.002	0.73	0.126±0.049
$(0,1) \times (60,150)$	0.002 ± 0.000	0.016 ± 0.006	0.000 ± 0.000	0.84	0.007±0.003
$(1,2.1) \times (8.5,10)$	6.008 ± 0.119	40.053 ± 15.507	4.552 ± 1.762	0.39	8.143±3.153
$(1,2.1) \times (10,14)$	5.232 ± 0.097	34.881 ± 13.503	3.964 ± 1.534	0.49	8.910±3.449
$(1,2.1) \times (14,18)$	0.996 ± 0.018	6.640 ± 2.570	0.755 ± 0.292	0.63	2.181±0.844
$(1,2.1) \times (18,30)$	0.425 ± 0.006	2.833 ± 1.096	0.107 ± 0.042	0.73	1.078±0.417
$(1,2.1) \times (30,60)$	0.043 ± 0.001	0.290 ± 0.112	0.004 ± 0.002	0.74	0.112±0.043
$(1,2.1) \times (60,150)$	0.002 ± 0.000	0.012 ± 0.005	0.000 ± 0.000	0.81	0.005±0.002
				Total:	34.301 ± 5.706

Table 4.11: Double parton scattering estimation.

4.7 Systematic uncertainties

Most of the systematic uncertainty associated with the $W^{\pm}$ boson and luminosity cancel out because we are measuring the ratio of two processes involving the $W^{\pm}$ in the same fiducial region. The systematic uncertainty on the inclusive $W^{\pm}$ yield number due to MC correction factors is investigated and found to be negligible at 0.0015%.The one systematic uncertainty on the inclusive $W^{\pm}$ yield number is discussed below, followed by the systematic uncertainties associated with the J/ψ.

4.7.1 Inclusive $W^{\pm}$ yield

The method used for determining the inclusive $W^{\pm}$ yield number relies on comparing data for the $W^{\pm} \rightarrow \mu^{\pm}\nu$ process with the MC for the signal and the known backgrounds. Since there is a mismatch between the data and MC that has to do with the method of determining E_{T}^{miss}, as discussed in Section 4.4.4, we have estimated a systematic uncertainty.

This systematic is determined by considering that the total number of inclusive $W^{\pm}$ candidates in the data sample is 6.23×10^{7} and the total number of inclusive $W^{\pm}$ candidates predicted by the MC model is 6.92×10^{7}. This gives a total discrepancy factor in the $\frac{\text{data}}{\text{model}}$ yield ratio of 0.9. Assuming that the discrepancy factor for only the backgrounds is the same 0.9, then the background model has a systematic uncertainty of 10%. Since the background model is approximately 10% of the total model, when subtracting the background model from the data, this propagates to a total systematic uncertainty due to this effect of 1.9%.

4.7.2 J/ψ mass and lifetime fit model

The choice of fit functions may introduce a systematic uncertainty for the mass and lifetime fits. These uncertainties are calculated by varying the fit model. We use a nominal fit model and alternate fit models for both the mass and pseudo-proper time fits, taking the maximum difference as a systematic uncertainty. See Appendix D for a full discussion of the nominal and alternate fits.

4.7.3 Vertex cut

We require the J/ψ vertex to be within 10 mm of the $W^{\pm}$ vertex. This choice might affect the pseudo-proper time distribution, biasing the measurement of the yield. We determine the impact of this choice by taking the yield difference provided by the nominal cut of 10 mm and a cut of 20 mm and including it as a systematic.

4.7.4 Pileup estimation

The uncertainty due to the pileup background estimation, as determined in Section 4.5.3, is folded into the systematics rather than into the statistical uncertainty.

4.7.5 J/ψ spin-alignment assumption

The nominal result in this note is calculated assuming an isotropic J/ψ spin-alignment scenario. However, since the associated production of $W^{\pm} + J/\psi$ is a new process for study, the spin-alignment profile of the J/ψ is unknown in these events and affects the acceptance for the J/ψ candidates. In order to account for this, we consider four other possible scenarios (longitudinal, transverse 0, transverse positive, transverse negative) and take the maximum difference between the nominal result and the alternate scenarios as a systematic uncertainty (also see Section 4.4.7).

4.7.6 J/ψ muon efficiency uncertainty

The p_{T} efficiencies used for the J/ψ muons are taken from nominal efficiency maps which are derived from data. A systematic is calculated by randomly varying these maps within a gaussian of width equal to the uncertainty of the nominal map. A new measurement is made and this process is repeated 100 times. The difference between the average of these measurements and the nominal measurement is taken as a systematic uncertainty.

The efficiencies of the J/ψ muons are derived from data driven tag-and-probe studies. The values of these efficiencies and their uncertainties depend on the muon transverse momentum and pseudorapidity. The effect of the uncertainty introduced into the cross-section ratio measurement due to the J/ψ muon efficiency uncertainty is treated as a systematic uncertainty. It is estimated by re-measuring the result using a J/ψ muon efficiency for each muon that is randomly sampled from a Gaussian distribution about the nominal value:

$$\mathrm{eff}_{\mathrm{sys}} = \mathrm{Gaussian}(\mu = \mathrm{eff}^{\mathrm{bin}}_{\mathrm{map}}, \sigma = \mathrm{maxerror}^{\mathrm{bin}}_{\mathrm{map}}). \tag{4.15}$$

This is done 100 times and the deviation between the mean of this result and the nominal result is taken as a systematic uncertainty.

4.7.7 Summary

A summary of the systematic uncertainties that are discussed in this section is given in Table 4.12. The systematic due to the spin-alignment uncertainty is dominant.

Source of Uncertainty	Percent Contribution	
	$\lvert y_{J/\psi}\rvert < 1$	$1 < \lvert y_{J/\psi}\rvert < 2.1$
J/ψ mass fit	9.5%	3.9%
Vertex separation	4.5%	8.4%
$\mu_{J/\psi}$ efficiency	1.2%	0.9%
Pileup	0.1%	0.3%
Inclusive W yield	1.9%	1.9%
J/ψ spin-alignment	30.0%	25.4%

Table 4.12: Systematic and spin-alignment uncertainty summary: Listed as a percentage of the nominal inclusive cross section measurement.

4.8 Results

4.8.1 Prompt $J/\psi + W^{\pm}$ production: yields

After the application of the selections to the dataset, the data is fitted and the signal is extracted. The signal extraction and cross section measurement is done in two J/ψ rapidity bins, $|y_{J/\psi}| < 1$ and $1 < |y_{J/\psi}| < 2.1$. This is done because the ATLAS detector performance differs slightly between the barrel and end-cap regions, and the

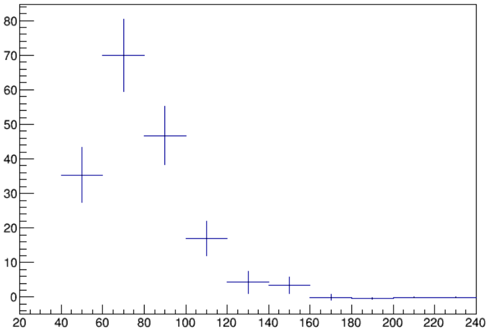

Figure 4.14: The transverse mass distribution of $W^{\pm}$ candidates associated with prompt J/ψ events in rapidity range $0 < |y_{J/\psi}| < 2.1$.

cross section could be rapidity dependent. The final results are presented in the two rapidity bins and also combined into the entire rapidity range.

The results of applying the two-dimensional mass and lifetime fit to the J/ψ candidate events are seen in Figures 4.15 and 4.16.

After the fit is performed, weights are derived using the sPlot tool. This tool assigns a weight, based on a selected normalization component of the fit model. Table 4.13 shows the final yield after the application of the J/ψ acceptance and muon efficiency weights. Pileup and QCD backgrounds are accounted for and subtracted off from the yield numbers before the final cross section calculation.

The transverse mass distribution of $W^{\pm}$ candidates associated with prompt J/ψ events is shown in Figure 4.14.

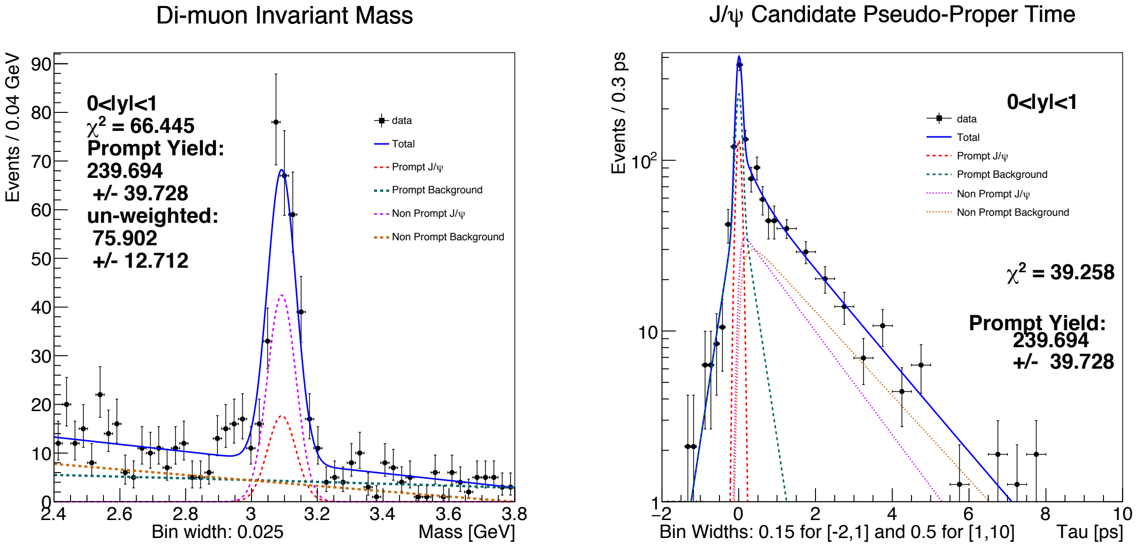

(a) (b)

Figure 4.15: J/ψ candidate (a) mass and (b) pseudo-proper time for rapidity range $|y_{J/\psi}| < 1$.

	$\lvert y_{J/\psi}\rvert < 1$		$1 < \lvert y_{J/\psi}\rvert < 2.1$	
	yield	± uncertainty	yield	± uncertainty
un-weighted	75.9	12.7	81.5	12.7
weighted	239.7	39.7	178.4	30.0

Table 4.13: J/ψ yields, before and after event by event weighting of each candidate based on J/ψ acceptance and J/ψ muon efficiency.

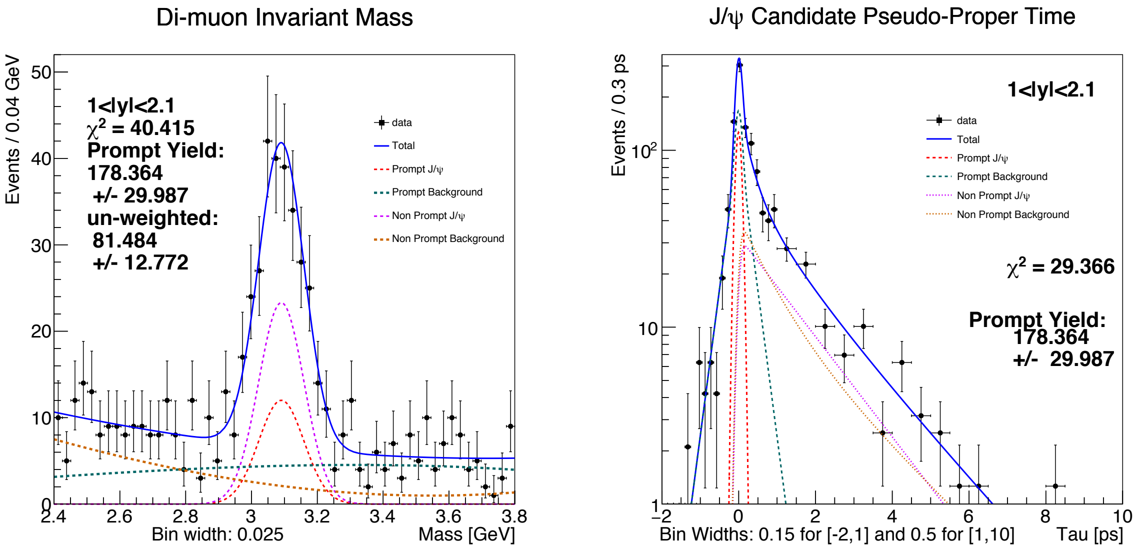

(a)

(b)

Figure 4.16: J/ψ candidate (a) mass and (b) pseudo-proper time for rapidity range $1 < |y_{J/\psi}| < 2.1$.

4.8.2 Cross-section ratio measurement

A final result for the total cross-section ratio is calculated in three different ways: fiducial, inclusive and DPS-subtracted. The explanation of each of these methods follows, and the corresponding cross-section results are presented in Equations 4.17, 4.19 and 4.20. The systematic due to the spin-alignment uncertainty is presented separately in the final results so that it can be corrected in the event that the spin alignment profile of J/ψ muons in association with a $W^{\pm}$ is measured at some point in the future.

4.8.3 Fiducial measurement

A first measurement is made that doesn't take into account the effect of the unknown J/ψ spin polarization. This is what is measured in the fiducial region of ATLAS without J/ψ acceptance corrections and is given by Equation 4.16.

$$R^{\text{fid}}_{J/\psi} = \frac{\mathcal{BR}(J/\psi \to \mu\mu)}{\sigma_{\text{fid}}(pp \to W)} \cdot \sigma_{\text{fid}}(pp \to W + J/\psi) = \frac{N^{\text{eff}}(W + J/\psi)}{N(W)} - R^{\text{fid}}_{\text{pileup}} \tag{4.16}$$

Where $N^{\text{eff}}(W + J/\psi)$ is the yield of W+prompt J/ψ events after corrections for the J/ψ muon reconstruction efficiencies, $N(W)$ is the background subtracted yield of inclusive W events and $R^{\text{fid}}_{\text{pileup}}$ is the expected pileup background contribution in the fiducial J/ψ acceptance. We measure the total result

$$R^{\text{fid}}_{J/\psi} = (3.45 \pm 0.40 \pm 0.25) \times 10^{-6}, \tag{4.17}$$

where the first uncertainty is statistical and the second is systematic.

4.8.4 Inclusive measurement

The full corrected production cross section ratio includes the fiducial acceptance of the muons from the J/ψ decay and is given by equation 4.18.

$$R^{\text{incl}}_{J/\psi} = \frac{\mathcal{BR}(J/\psi \to \mu\mu)}{\sigma_{\text{incl}}(pp \to W)} \cdot \sigma_{\text{incl}}(pp \to W + J/\psi) = \frac{N^{\text{eff+acc}}(W + J/\psi)}{N(W)} - R_{\text{pileup}} \tag{4.18}$$

Where $N^{\text{eff+acc}}(W + J/\psi)$ is the yield of W+prompt J/ψ events after J/ψ acceptance corrections and efficiency correction for both J/ψ decay muons, R_{pileup} is the expected pileup contribution in the full J/ψ decay phase space and the other variables remain as for $R^{\text{fid}}_{J/\psi}$. We measure the total result

$$R^{\text{incl}}_{J/\psi} = (8.02 \pm 0.95 \pm 0.61 \pm 1.63) \times 10^{-6}, \tag{4.19}$$

where the first uncertainty is statistical, the second systematic and the third from the spin-alignment uncertainty. Additionally we measure the inclusive differential cross section in six J/ψ transverse momentum bins. These results are shown in Figure 4.17 and Table 4.14. Next-to-leading-order color-octet (NLO CO) set 1 predictions are extracted via a global fit from various hadroproduction, photoproduction, two-photon scattering and electron-positron annihilation experiments [56]. Set 2 are extracted by fitting the differential cross section and polarization of prompt J/ψ simultaneously at the Tevatron [57]. The DPS contributions estimated using the methods discussed is shown, the portion of the signal it accounts for and the value of $p_T^{J/\psi}$ are inversely proportional. The theory predictions do not include contributions from CS or DPS processes, which could explain why the theory values under-predict the measured values.

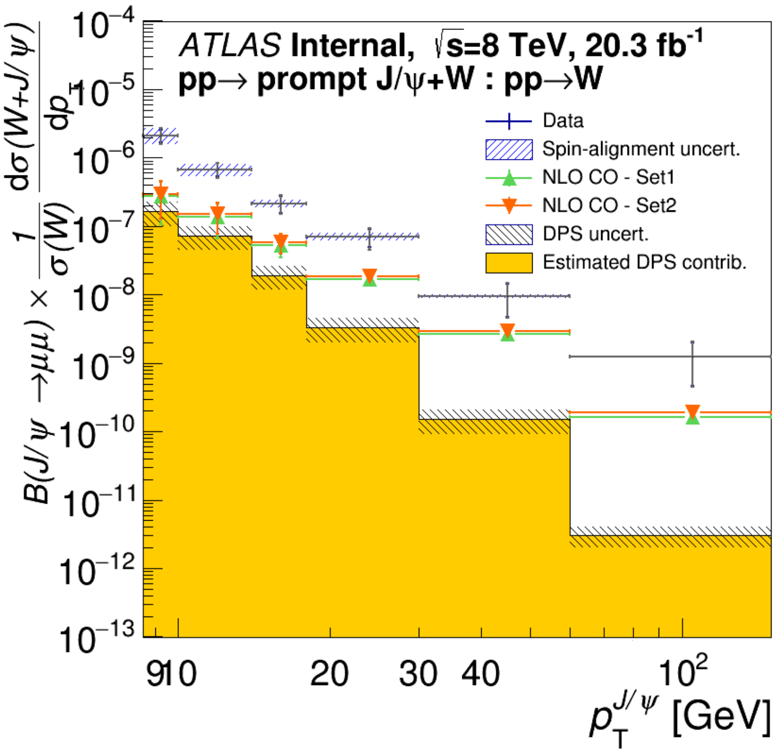

Figure 4.17: Differential cross section ratio measurements and theory predictions presented in six p_{T} bins.

.

$\lvert y^{J/\psi}\rvert \times p_{\mathrm{T}}^{J/\psi}$ [GeV]	Inclusive prompt ratio [$\times 10^{-7}$/ GeV]			Estimated DPS [$\times 10^{-7}$/ GeV]
	value $\pm$ (stat) $\pm$	(syst) $\pm$	(spin)	assuming $\sigma_{\mathrm{eff}} = 15\,\mathrm{mb}$
$(0, 2.1) \times (8.5, 10)$	21.31 ± 4.26	$\pm\ 3.49$	$\pm\ 5.65$	1.65 ± 0.64
$(0, 2.1) \times (10, 14)$	6.80 ± 1.49	$\pm\ 0.81$	$\pm\ 1.39$	0.73 ± 0.28
$(0, 2.1) \times (14, 18)$	2.16 ± 0.63	$\pm\ 0.21$	$\pm\ 0.30$	0.19 ± 0.07
$(0, 2.1) \times (18, 30)$	0.698 ± 0.202	$\pm\ 0.140$	$\pm\ 0.086$	0.033 ± 0.013
$(0, 2.1) \times (30, 60)$	0.0958 ± 0.0480	$\pm\ 0.0165$	$\pm\ 0.0066$	0.0015 ± 0.0006
$(0, 2.1) \times (60, 150)$	0.0125 ± 0.0078	$\pm\ 0.0015$	$\pm\ 0.0006$	0.00003 ± 0.00001

Table 4.14: The inclusive (SPS+DPS) cross-section ratio $\mathrm{d}R^{\mathrm{incl}}_{W+J/\psi}/\mathrm{d}p_{\mathrm{T}}$ for prompt J/ψ. The estimated DPS contributions for each bin are listed.

4.8.5 DPS-subtracted measurement (for theory comparison)

A third measurement is made by subtracting off the estimated DPS contribution from the inclusive measurement. This is used to compare with theory values. The DPS contribution is estimated from the measured $J/\psi \to \mu^+\mu^-$ cross section result performed by this analysis [58]. We use the method described in 4.6 to estimate that the cross sections listed in Table 4.14 are due to DPS events.

We measure the total result

$$R_{J/\psi}^{\mathrm{DPSsub}} = (7.36 \pm 0.96 \pm 0.61 \pm 1.63) \times 10^{-6}, \tag{4.20}$$

where the first uncertainty is statistical, the second systematic and the third from the spin-alignment uncertainty. The results per p_{T} bin are also presented in Figure 4.17.

Theoretical comparison is made with $J/\psi + W^{\pm}$ predictions based on [59]. Theoretical calculations are made using two sets of CO LDME[11] for J/ψ. The first set is extracted via a global fit from various hadroproduction, photoproduction, two-photon scattering and electron-positron annihilation experiments [56]. The second set is extracted by fitting the differential cross-section and polarization of prompt J/ψ simultaneously at the Tevatron [57].

Theoretical calculations include only SPS and CO models and are normalized to NNLO calculations of the $W^{\pm}$ boson fiducial production cross-section (7.072 nb for W^+ and 5.015 nb for W^-). Further comparison with the theory numbers is discussed in Section 4.10.

---

[11] color-octet long-distance matrix element

4.8.6 Discussion of $\Delta\phi(J/\psi, W^{\pm})$ as DPS probe

The opening azimuthal angle between the $W^{\pm}$ and the J/ψ particles, $\Delta\phi(J/\psi, W^{\pm})$, is shown in Figure 4.18. It can be used to identify the total number of SPS and DPS events. This data in this plot was weighted using the sPlot tool so that only events associated with prompt J/ψ candidates are shown. The estimated DPS contribution is shown with a yellow band where the method discussed in Section 4.6 has been used to estimate it. The rest of the events, particularly those close to $\Delta\phi = \pi$, are assumed to come from SPS interactions.

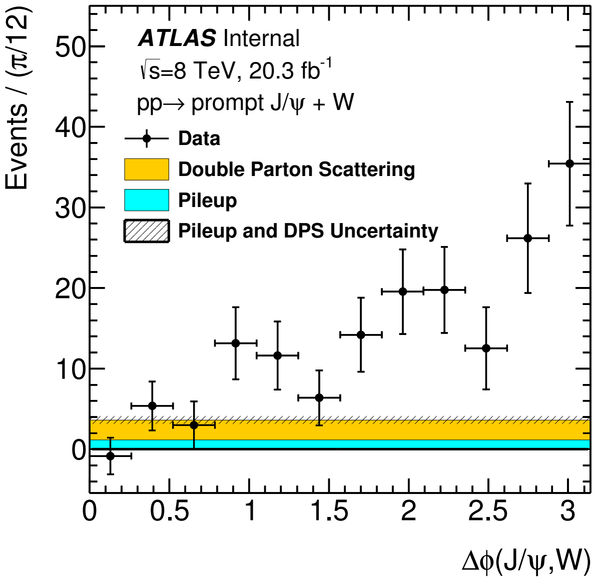

Figure 4.18: $\Delta\phi(J/\psi, W^{\pm})$ for prompt $J/\psi + W^{\pm}$ events.

4.8.7 Measurement summary

The total cross section results of the three measurement methods discussed above are presented in Figure 4.19. The DPS-subtracted measurement is compared with theory predictions and shows that theory under-predicts the measured value, which could be because the theory does not include contributions from CS processes. The total cross section ratio results are also presented in two rapidity regions in Table 4.15.

We also obtain well measured differential cross-section ratio values across the entire range of 8.5< $p_T^{J/\psi}$ <150, shown in Figure 4.17. The theory does not include contributions from CS or DPS processes, which could explain why it under-predicts the measurement.

These results can be used to enhance future theory predictions.

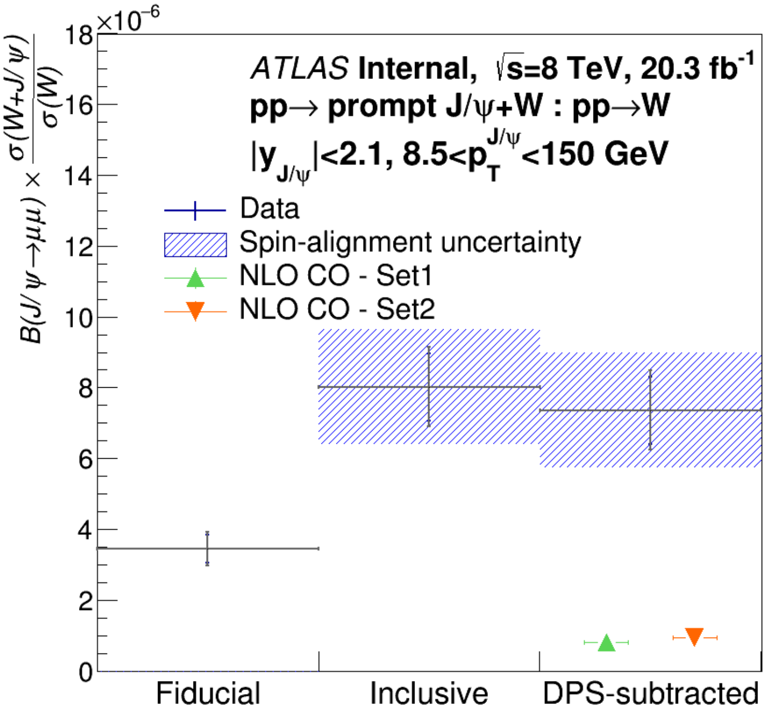

Figure 4.19: Total integrated cross section ratio measurements. The fiducual result does not correct for the unknown J/ψ spin polarization. The inclusive result includes all known corrections discussed previously. The DPS-subtracted result is compared to theory predictions, and shows that the theory underestimates the measurement.

$y_{J/\psi}$	Fiducial $[\times 10^{-6}]$	Inclusive $[\times 10^{-6}]$	DPS-subtracted $[\times 10^{-6}]$
	value $\pm$ (stat) $\pm$ (syst)	value $\pm$ (stat) $\pm$ (syst) $\pm$ (spin)	value $\pm$ (stat) $\pm$ (syst) $\pm$ (spin)
$\lvert y_{J/\psi}\rvert < 1.0$	$1.78 \pm 0.29 \pm 0.23$	$4.60 \pm 0.76 \pm 0.45 \pm 1.38$	$4.33 \pm 0.76 \pm 0.45 \pm 1.38$
$1.0 < \lvert y_{J/\psi}\rvert < 2.1$	$1.67 \pm 0.28 \pm 0.10$	$3.42 \pm 0.58 \pm 0.40 \pm 0.87$	$3.03 \pm 0.58 \pm 0.40 \pm 0.87$

Table 4.15: The fiducial, inclusive (SPS+DPS) and DPS-subtracted differential cross-section ratio $\mathrm{d}R_{Z+J/\psi}/\mathrm{d}y$ as a function of $y_{J/\psi}$.

4.9 Detailed Results

Tables 4.16 and 4.17 show the details of the inclusive differential cross section ratio measurement separated into two J/ψ rapidity and six transverse momentum regions.

$\lvert y^{J/\psi}\rvert \times p_{\mathrm{T}}^{J/\psi}$ [GeV]	Inclusive prompt ratio [$\times 10^{-7}$/ GeV]			Estimated DPS [$\times 10^{-7}$/ GeV]
	value $\pm$ (stat) $\pm$	(syst) $\pm$	(spin)	assuming $\sigma_{\mathrm{eff}} = 15\,\mathrm{mb}$
$(0,1) \times (8.5,10)$	13.3 ± 3.3	± 1.89	± 4.9	0.61 ± 0.24
$(0,1) \times (10,14)$	3.79 ± 1.25	± 0.40	± 1.16	0.30 ± 0.12
$(0,1) \times (14,18)$	0.918 ± 0.439	± 0.140	± 0.199	0.084 ± 0.033
$(0,1) \times (18,30)$	0.412 ± 0.154	± 0.110	± 0.079	0.016 ± 0.006
$(0,1) \times (30,60)$	0.0448 ± 0.0337	± 0.0121	± 0.0050	0.00081 ± 0.00031
$(0,1) \times (60,150)$	0.00957 ± 0.00638	± 0.00116	± 0.00054	0.00002 ± 0.00001

Table 4.16: The inclusive (SPS+DPS) cross-section ratio $\mathrm{d}R^{\mathrm{incl}}_{W+J/\psi}/\mathrm{d}p_{\mathrm{T}}$ for $\lvert y_{J/\psi}\rvert < 1$, including the estimated DPS contributions for each bin.

$\lvert y^{J/\psi}\rvert \times p_{\mathrm{T}}^{J/\psi}$ [GeV]	Inclusive prompt ratio [$\times 10^{-7}$/ GeV]			Estimated DPS [$\times 10^{-7}$/ GeV]
	value $\pm$ (stat) $\pm$	(syst) $\pm$	(spin)	assuming $\sigma_{\mathrm{eff}} = 15\,\mathrm{mb}$
$(1, 2.1) \times (8.5, 10)$	7.99 ± 2.65	± 1.59	± 2.79	1.04 ± 0.40
$(1, 2.1) \times (10, 14)$	3.01 ± 0.81	± 0.40	± 0.76	0.43 ± 0.17
$(1, 2.1) \times (14, 18)$	1.24 ± 0.45	± 0.07	± 0.23	0.105 ± 0.040
$(1, 2.1) \times (18, 30)$	0.286 ± 0.130	± 0.031	± 0.036	0.017 ± 0.007
$(1, 2.1) \times (30, 60)$	0.0510 ± 0.0341	± 0.0045	± 0.0043	0.00071 ± 0.00028
$(1, 2.1) \times (60, 150)$	0.0029 ± 0.0045	± 0.0003	± 0.0001	0.00011 ± 0.00004

Table 4.17: The inclusive (SPS+DPS) cross-section ratio $\mathrm{d}R^{\mathrm{incl}}_{W+J/\psi}/\mathrm{d}p_{\mathrm{T}}$ for $1 < \lvert y_{J/\psi}\rvert < 2.1$, including the estimated DPS contributions for each bin.

4.10 Comparison with the $\sqrt{s} = 7\,\text{TeV}$ result and theory

The results of the prompt $J/\psi + W^{\pm}$ analysis, performed with the $\sqrt{s} = 7\,\text{TeV}$ data [43] are compared with the results of the $\sqrt{s} = 8\,\text{TeV}$ data analysis. We also compare the DPS subtracted total results with the numbers predicted by theory [57].

4.10.1 Differential results

The results of the inclusive differential cross section measurements are shown in Figure 4.20.

4.10.2 Total results

The results of the total DPS subtracted cross section measurements and theory predictions for both 7 and 8 TeV are shown in Table 4.18.

	Theory, Color Octet	Measurement ± stat ± syst ± pol
7 TeV	$(22.68 \pm 3.36) \times 10^{-8}$	$(328 \pm 134 \pm 92^{+172}_{-105}) \times 10^{-8}$
8 TeV	$(81.282 \pm 3.251) \times 10^{-8}$	$(736 \pm 96 \pm 61 \pm 163) \times 10^{-8}$
8 TeV†	$(94.408 \pm 3.776) \times 10^{-8}$	

Table 4.18: Total DPS subtracted cross section ratio numbers. (†Alternate polarization set.)

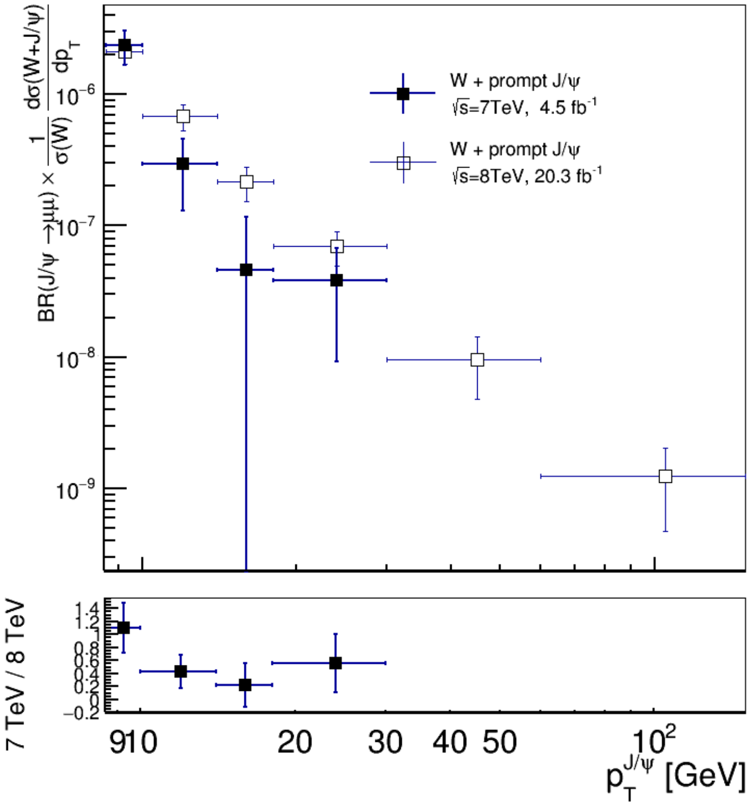

Figure 4.20: Comparison of the 8 TeV with the 7 TeV inclusive differential cross section ratio results. This analysis has made more precise measurements and extended the measurements into two additional $p_{\mathrm{T}}^{J/\psi}$ bins.

Chapter 5

Conclusions

This dissertation has presented a measurement of the prompt $J/\psi + W^{\pm}$ production rate as a ratio to the inclusive $W^{\pm}$ production rate using 20.3 fb^{-1} of data collected from proton-proton collisions at center of mass energy $\sqrt{s} = 8$ TeV.

The measurements presented have shed light on the not fully understood mechanism of charmonium particle production in hadronic collisions, especially on the relative importance of the Color Singlet and Color Octet processes. These measurements have also been able to probe the relative contributions of the single and double parton scattering modes.

The only theoretical predictions available at the time of writing are for the single parton scattering Color Octet production mode. However the measured results are presented is a way that is readily comparable to the results of future theoretical calculations as they become available.

Chapter 6

Postscript

This dissertation was written during an important time of discovery for the field of particle physics. The largest accelerator ever built, the LHC, recently came on-line and almost immediately discovered the long sought after Higgs Boson. In 2015 the it provided beams for the first time at the unprecedented energy of 13 TeV and is preparing for a productive data taking run in 2016.

Physicists are now looking beyond the Standard Model to address known observations that are not explained by the model, such as massive neutrinos [5]. Theories like Supersymmetry (SUSY), Grand Unification and Superstrings are all being explored by theorists, and experimentalists are busy designing and developing the next generation of experiments to test them. Another unknown is the nature of dark matter and dark energy, explanations for their observation are being hotly pursued by many teams all over the world.

Many powerful next generation particle accelerators have been proposed by host sites in many countries. The Future Circular Collider (FCC) is the proposed successor to the LHC, which has a design energy of 100 TeV [60]. If it is built then it will provide the most powerful tool scientists have ever used to probe the fundamental nature of matter and forces in the universe.

References

[1] S Braibant, G Giacomelli, and M Spurio. *Particles and Fundamental Interactions.* Springer, Italy, 1st edition, 2009.

[2] Sheldon L. Glashow. Partial-symmetries of weak interactions, 1961.

[3] Steven Weinberg. A Model of Leptons. *Phys. Rev. Lett.*, 19:1264–1266, Nov 1967.

[4] G. 't Hooft and M. Veltman. Regularization and renormalization of gauge fields. *Nuclear Physics B*, 44(1):189 – 213, 1972.

[5] G Caughlan, J Dodd, and B Gripaios. *The Ideas of Particle Physics.* Cambridge University Press, Cambridge, UK, 3rd edition, 2006.

[6] V. Barger and R. Phillips. *Collider Physics.* Frontiers in physics. Addison-Wesley Publishing Company, 1997.

[7] O. Boyarkin. *Advanced Particle Physics Volume I: Particles, Fields, and Quantum Electrodynamics.* Advanced Particle Physics. CRC Press, 2011.

[8] W.N. Cottingham and D.A. Greenwood. *An Introduction to the Standard Model of Particle Physics.* Cambridge University Press, 2007.

[9] K. A. Olive et al. Review of Particle Physics. *Chin. Phys.*, C38:090001, 2014.

[10] J. Soto N. Brambilla, A. Pineda and A. Vairo. Potential NRQCD: An Effective theory for heavy quarkonium. *Nucl.Phys.*, Science(B566), 2000.

[11] J. E. Augustin et al. Discovery of a Narrow Resonance in e+ e- Annihilation. *Phys. Rev. Lett.*, 33:1406–1408, 1974. [Adv. Exp. Phys.5,141(1976)].

[12] J. J. Aubert et al. Experimental Observation of a Heavy Particle J. *Phys. Rev. Lett.*, 33:1404–1406, 1974.

[13] Makoto Kobayashi and Toshihide Maskawa. CP Violation in the Renormalizable Theory of Weak Interaction. *Prog. Theor. Phys.*, 49:652–657, 1973.

[14] Nicola Cabibbo. Unitary Symmetry and Leptonic Decays. *Phys. Rev. Lett.*, 10:531–533, Jun 1963.

[15] S. W. Herb, D. C. Hom, L. M. Lederman, J. C. Sens, H. D. Snyder, J. K. Yoh, J. A. Appel, B. C. Brown, C. N. Brown, W. R. Innes, K. Ueno, T. Yamanouchi, A. S. Ito, H. Jöstlein, D. M. Kaplan, and R. D. Kephart. Observation of a Dimuon Resonance at 9.5 GeV in 400-GeV Proton-Nucleus Collisions. *Phys. Rev. Lett.*, 39:252–255, Aug 1977.

[16] F. et. al. Abe. Observation of Top Quark Production in $\overline{p}p$ Collisions with the Collider Detector at Fermilab. *Phys. Rev. Lett.*, 74:2626–2631, Apr 1995.

[17] Abbott B. et. al. Abachi, S. Observation of the Top Quark. *Phys. Rev. Lett.*, 74:2632–2637, Apr 1995.

[18] Georges Aad et al. Observation of a new particle in the search for the Standard Model Higgs boson with the ATLAS detector at the LHC. *Phys. Lett.*, B716:1–29, 2012.

[19] Serguei Chatrchyan et al. Observation of a new boson at a mass of 125 GeV with the CMS experiment at the LHC. *Phys. Lett.*, B716:30–61, 2012.

[20] The CERN Large Hadron Collider: Accelerator and Experiments vol. 1. *JINST*, 3 S08001, Aug 2008.

[21] ATLAS IBL Community. Insertable B-Layer Technical Design Report. volume 013, 2010.

[22] B Resende. Muon identification algorithms in ATLAS. Technical Report ATL-PHYS-PROC-2009-113, CERN, Geneva, Sep 2009.

[23] Georges Aad et al. Measurement of the muon reconstruction performance of the ATLAS detector using 2011 and 2012 LHC proton-proton collision data. *Eur. Phys. J.*, C74(11):3130, 2014.

[24] Matteo Cacciari, Gavin P. Salam, and Gregory Soyez. The Anti-k(t) jet clustering algorithm. *JHEP*, 04:063, 2008.

[25] B. A. Kniehl et al. Associated production of heavy quarkonia and electroweak bosons at present and future colliders. *Phys. Rev. D*, 66:114002, 2012.

[26] N. Brambilla et al. Heavy quarkonium physics. 2004.

[27] N. Brambilla et al. Heavy quarkonium: progress, puzzles, and opportunities. *Eur. Phys. J.*, C71:1534, 2011.

[28] J. P. Lansberg. On the mechanisms of heavy-quarkonium hadroproduction.

[29] Mathias Butenschoen and Bernd A. Kniehl. World data of J/ψ production consolidate nonrelativistic QCD factorization at next-to-leading order. *Phys. Rev. D*, 84:051501, Sep 2011.

[30] Mathias Butenschoen and Bernd A. Kniehl. Next-to-leading-order tests of NRQCD factorization with J/ψ yield and polarization. *Mod. Phys. Lett.*, A28:1350027, 2013.

[31] S. P. Baranov, A. V. Lipatov, and N. P. Zotov. Prompt J/ψ production at the LHC: New evidence for the k_T factorization. *Phys. Rev. D*, 85:014034, Jan 2012.

[32] Yan-Qing Ma, Kai Wang, and Kuang-Ta Chao. A complete NLO calculation of the J/ψ and ψ' production at hadron colliders. *Phys. Rev.*, D84:114001, 2011.

[33] John C. Collins, Davison E. Soper, and George Sterman. Heavy particle production in high-energy hadron collisions. *Nuclear Physics B*, 263(1):37 – 60, 1986.

[34] W.E. Caswell and G.P. Lepage. Effective lagrangians for bound state problems in qed, qcd, and other field theories. *Physics Letters B*, 167(4):437 – 442, 1986.

[35] Geoffrey T. Bodwin, Eric Braaten, and G. Peter Lepage. Rigorous QCD analysis of inclusive annihilation and production of heavy quarkonium. *Phys. Rev.*, D51:1125–1171, 1995. [Erratum: Phys. Rev.D55,5853(1997)].

[36] Peter L. Cho and Adam K. Leibovich. Color octet quarkonia production. *Phys. Rev.*, D53:150–162, 1996.

[37] Peter L. Cho and Adam K. Leibovich. Color octet quarkonia production. 2. *Phys. Rev.*, D53:6203–6217, 1996.

[38] J. F. Amundson, Oscar J. P. Eboli, E. M. Gregores, and F. Halzen. Quantitative tests of color evaporation: Charmonium production. *Phys. Lett.*, B390:323–328, 1997.

[39] L. Gang, S. Mao, Z. Ren-You, and M. Wen-Gan. QCD corrections to J/ψ production in association with a W boson at the LHC. *Phys. Rev. D*, 83:014001, Jan. 2011.

[40] Bernd A. Kniehl, Caesar P. Palisoc, and Lennart Zwirner. Associated production of heavy quarkonia and electroweak bosons at present and future colliders. *Phys. Rev.*, D66:114002, 2002.

[41] Gang Li, Mao Song, Ren-You Zhang, and Wen-Gan Ma. QCD corrections to J/ψ production in association with a W-boson at the LHC. *Phys. Rev.*, D83:014001, 2011.

[42] J. P. Lansberg and C. Lorce. Reassessing the importance of the colour-singlet contributions to direct $J/\psi + W$ production at the LHC and the Tevatron. *Phys. Lett.*, B726:218–222, 2013. [Erratum: Phys. Lett.B738,529(2014)].

[43] Georges Aad et al. Measurement of the production cross section of prompt J/ψ mesons in association with a $W^{\pm}$ boson in pp collisions at $\sqrt{s} = 7$ TeV with the ATLAS detector. *JHEP*, 04:172, 2014.

[44] Muriel Pivk and Francois R. Le Diberder. sPlot: A Statistical tool to unfold data distributions. *Nucl.Instrum.Meth.*, A555:356–369, 2005.

[45] Torbjorn Sjostrand, Stephen Mrenna, and Peter Z. Skands. A Brief Introduction to PYTHIA 8.1. *Comput.Phys.Commun.*, 178:852–867, 2008.

[46] Michelangelo L. Mangano, Mauro Moretti, Fulvio Piccinini, Roberto Pittau, and Antonio D. Polosa. ALPGEN, a generator for hard multiparton processes in hadronic collisions. *JHEP*, 07:001, 2003.

[47] Stefano Frixione and Bryan R. Webber. Matching NLO QCD computations and parton shower simulations. *JHEP*, 06:029, 2002.

[48] Borut Paul Kersevan and Elzbieta Richter-Was. The Monte Carlo event generator AcerMC versions 2.0 to 3.8 with interfaces to PYTHIA 6.4, HERWIG 6.5 and ARIADNE 4.1. *Comput. Phys. Commun.*, 184:919–985, 2013.

[49] Stefano Moretti. HERWIG: An Event generator for MSSM processes. In *High energy physics phenomenology. Proceedings, 7th Workshop, WHEPP-7, Allahabad, India, January 4-15, 2002*, 2002. [Submitted to: Pramana(2002)].

[50] First tuning of HERWIG/JIMMY to ATLAS data. 2010.

[51] Gunter Zech. Comparing statistical data to Monte Carlo simulation: Parameter fitting and unfolding. 1995.

[52] W. Verkerke and D. Kirkby. The RooFit toolkit for data modeling. *ArXiv Physics e-prints*, June 2003.

[53] Nicola Orlando. Muon reconstruction efficiency measurement in the ATLAS experiment. *EPJ Web Conf.*, 28:12040, 2012.

[54] Georges Aad et al. Observation and measurements of the production of prompt and non-prompt J/ψ mesons in association with a Z boson in pp collisions at $\sqrt{s}$ = 8 TeV with the ATLAS detector. *Eur.Phys.J.*, C75(5):229, 2015.

[55] ATLAS Collaboration. Measurement of hard double-parton interactions in $W(\rightarrow \nu) + 2jet$ events at $\sqrt{s} = 7$ TeV with the ATLAS detector. *New Journal of Physics*, 15(3):033038, 2013.

[56] Mathias Butenschoen and Bernd A. Kniehl. J/ψ production in NRQCD: A global analysis of yield and polarization. *Nucl.Phys.Proc.Suppl.*, 222-224:151–161, 2012.

[57] Kuang-Ta Chao, Yan-Qing Ma, Hua-Sheng Shao, Kai Wang, and Yu-Jie Zhang. J/ψ Polarization at Hadron Colliders in Nonrelativistic QCD. *Phys.Rev.Lett.*, 108:242004, 2012.

[58] Georges Aad et al. Measurement of the differential cross-sections of prompt and non-prompt production of J/ψ and ψ(2S) in pp collisions at $\sqrt{s} = 7$ and 8 TeV with the ATLAS detector. 2015.

[59] Mao Song, Gang Li, Wen-Gan Ma, Ren-You Zhang, Lei Guo, et al. J/ψ Production Associated with a W-Boson at the 7 TeV Large Hadron Collider. *Chin.Phys.Lett.*, 30:091201, 2013.

[60] M. Bicer et al. First Look at the Physics Case of TLEP. *JHEP*, 01:164, 2014.

Appendix A

Feasibility of measuring $W^{\pm}$ + non-prompt J/ψ

Non-prompt J/ψ's in $J/\psi + W^{\pm}$ events are produced from a secondary vertex, such as a b meson decay. The two-dimensional mass and lifetime fit used in this analysis can very effectively separate prompt and non-prompt events. However there are significantly more physics backgrounds to account for in the non-prompt sample. In particular $t\bar{t}$ is a major background for these events, because it commonly decays to a b and then to a J/ψ. To find the non-prompt signal, the number of background events must be estimated using MC and then subtracted from the data.

An attempt was made to perform an additional measurement using these non-prompt J/ψ candidates, but we are unable to obtain well measured differential cross section ratio values for non-prompt events because the MC backgrounds dominate the signal. We have 354 data events, of which 337.1 are background. Furthermore, accounting for this variation in yield that depends on the $t\bar{t}$ MC generator choice would introduce a large statistical uncertainty. A non-prompt measurement would be more feasible with better modeling of the $t\bar{t}$ background.

A.1 Background contamination of non-prompt signal

Table A.1 shows the final prompt and non-prompt J/ψ yield after the application of the J/ψ acceptance and muon efficiency weights, before and after the subtractions of the backgrounds. Contamination of the non-prompt signal due to backgrounds is seen (dominated by $t\bar{t}$). The $m_{\mathrm{T}}(W)$ for $W^{\pm}$ + non-prompt J/ψ events from the MC background sample is seen in Figure A.1. This shows that there are many real $W^{\pm}$ + non-prompt J/ψ events resulting from background physics processes.

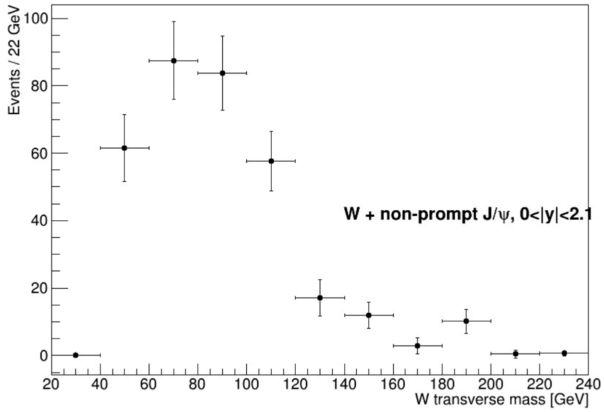

Figure A.1: $m_{\mathrm{T}}(W)$ for the $W+$ non $-$ prompt J/ψ events seen in the MC background samples listed in Table A.1.

A.2 Conclusion

There are real J/ψ events in the non-prompt candidates due to background, dominated by $t\bar{t}$. We are unable to make a good measurement of the cross section ratio for non-prompt J/ψ events because the uncertainties are too large. This measurement would be improved by better modeling of the $t\bar{t}$ background. The two samples examined have a large discrepancy between them (see in Table A.1).

	un-weighted by $J/\psi < \epsilon \times \mathcal{A} >$	
Sample	yield	± error
Data	354	23
MC: W$\rightarrow$eν	0	0
MC: W$\rightarrow\mu\nu$	4	3
MC: W$\rightarrow\tau\nu$	0	0
MC: Z+jets	2.0	1.6
MC: Single t	13	6.4
MC: Diboson	7.70	0.07
MC: $t\bar{t}$	299	3
MC: All backgrounds summed	337.1	0.3

Table A.1: Final non-Prompt $J/\psi + W^{\pm}$ event yields for both data and background MC samples in the range 0< $|\eta|$ <2.1. The signal and background weight extraction proceedure returns slightly different numbers when applied to each individual sample then summing vs summing first then extracting the weights.

Appendix B

Supporting material for pileup background estimation

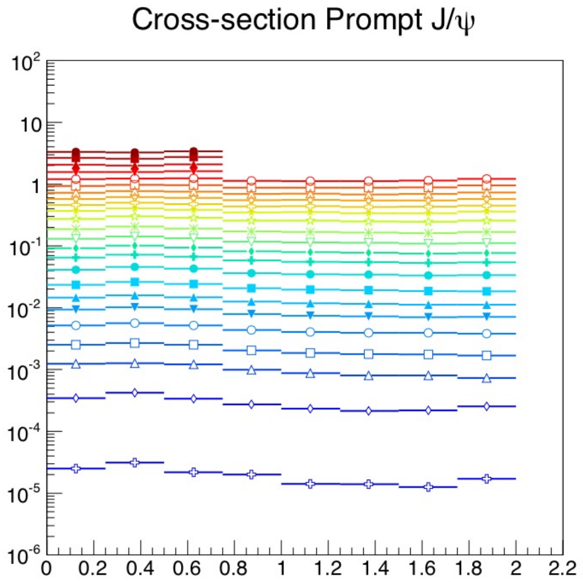

Figure B.1: $J/\psi \to \mu^+\mu^-$ cross section vs y distribution. The colors from red to violet (top to bottom) show J/ψ_{p_T} bins in the widths $8.0-8.5; 8.5-9.0; 9.0-9.5; 9.5-10.0; 10.0-10.5; 10.5-11.0; 11.0-11.5; 11.5-12.0; 12.5-13.0; 13.5-14.0; 14-15; 15-16; 16-17; 17-18; 18-19; 19-20; 20-22; 22-24; 24-26; 26-30; 30-35; 35-40; 40-60; 60-110; 110-150$. [43]

$J/\psi_{(p_T)}$	$0.00 < J/\psi_y < 0.25$	$0.25 < J/\psi_y < 0.50$	$0.50 < J/\psi_y < 0.75$
110-150	$(3.25 \pm 1.47) \times 10^{-10}$	$(3.35 \pm 1.51) \times 10^{-10}$	$(2.53 \pm 1.23) \times 10^{-10}$
	$0.75 < J/\psi_y < 1.00$	$1.00 < J/\psi_y < 1.25$	$1.25 < J/\psi_y < 1.50$
8.5-9.0	(2.11 ± 0.07)	(2.15 ± 0.04)	(2.03 ± 0.04)
9.0-9.5	(1.66 ± 0.04)	(1.71 ± 0.03)	(1.61 ± 0.03)
9.5-10.0	(1.31 ± 0.03)	(1.36 ± 0.02)	(1.28 ± 0.02)
110-150	$(1.73 \pm 1.00) \times 10^{-10}$	$(5.50 \pm 2.17) \times 10^{-10}$	$(3.91 \pm 1.71) \times 10^{-10}$
	$1.50 < J/\psi_y < 1.75$	$1.75 < J/\psi_y < 2.00$	$2.00 < J/\psi_y < 2.10$
8.5-9.0	(2.05 ± 0.04)	(2.09 ± 0.05)	(1.84 ± 0.06)
9.0-9.5	(1.62 ± 0.03)	(1.64 ± 0.03)	(1.44 ± 0.04)
9.5-10.0	(1.28 ± 0.02)	(1.29 ± 0.02)	(1.13 ± 0.03)
110-150	$(3.54 \pm 1.41) \times 10^{-10}$	$(2.00 \pm 0.81) \times 10^{-10}$	$(2.58 \pm 1.13) \times 10^{-10}$

Table B.1: Extrapolated $J/\psi \to \mu^+\mu^-$ cross-section values using a double exponential fit.

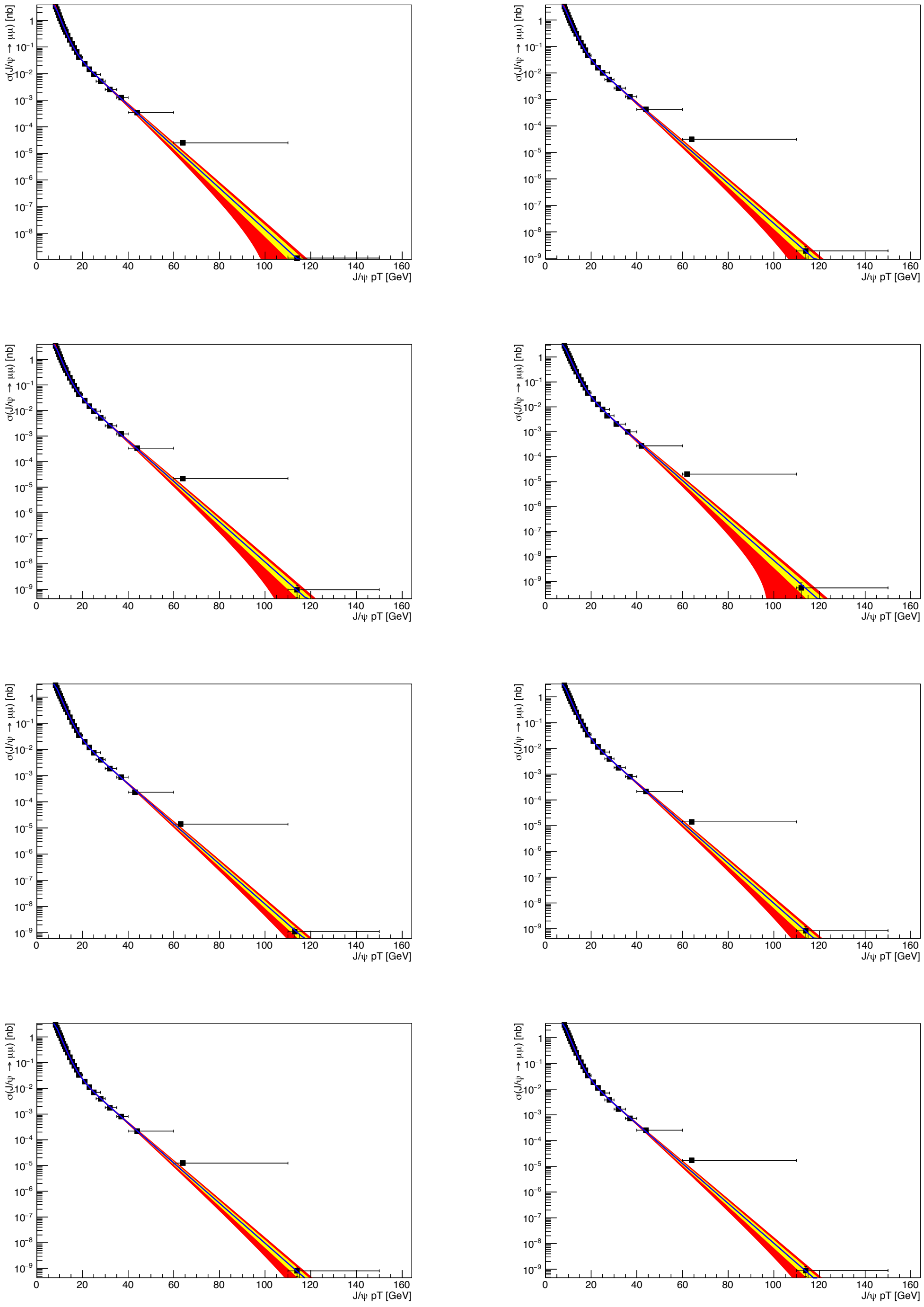

Figure B.2: Prompt $J/\psi \to \mu^+\mu^-$ cross section double exponential extrapolation for rapidity 0.0 to 2.0 divided into eight rapidity bins (of width 0.25 each). The yellow and red bands are the 68% and 95% confidence intervals.

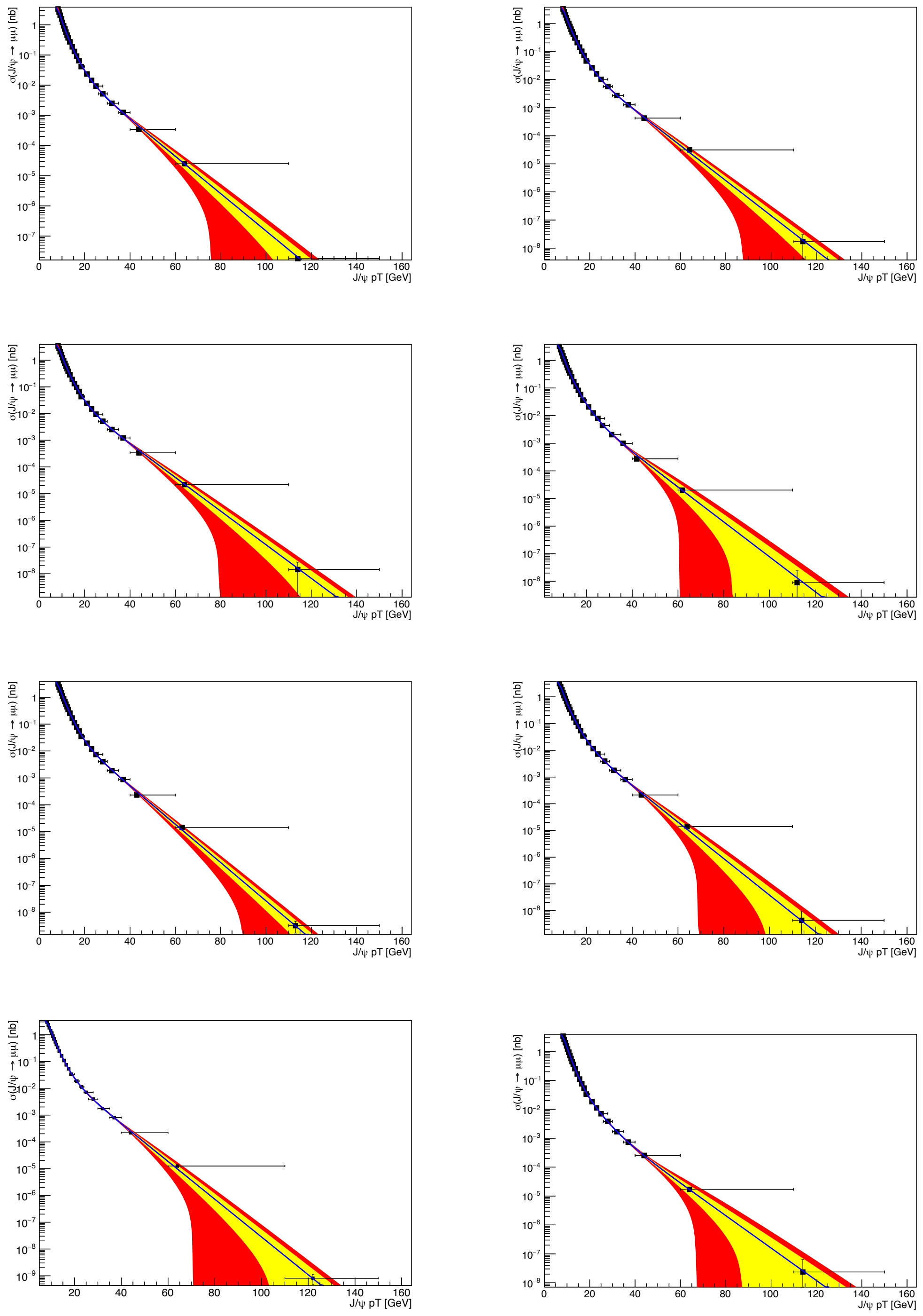

Figure B.3: Prompt $J/\psi \rightarrow \mu^+\mu^-$ cross section triple exponential extrapolation for rapidity 0.0 to 2.0 divided into eight rapidity bins (of width 0.25 each). The yellow and red bands are the 68% and 95% confidence intervals.

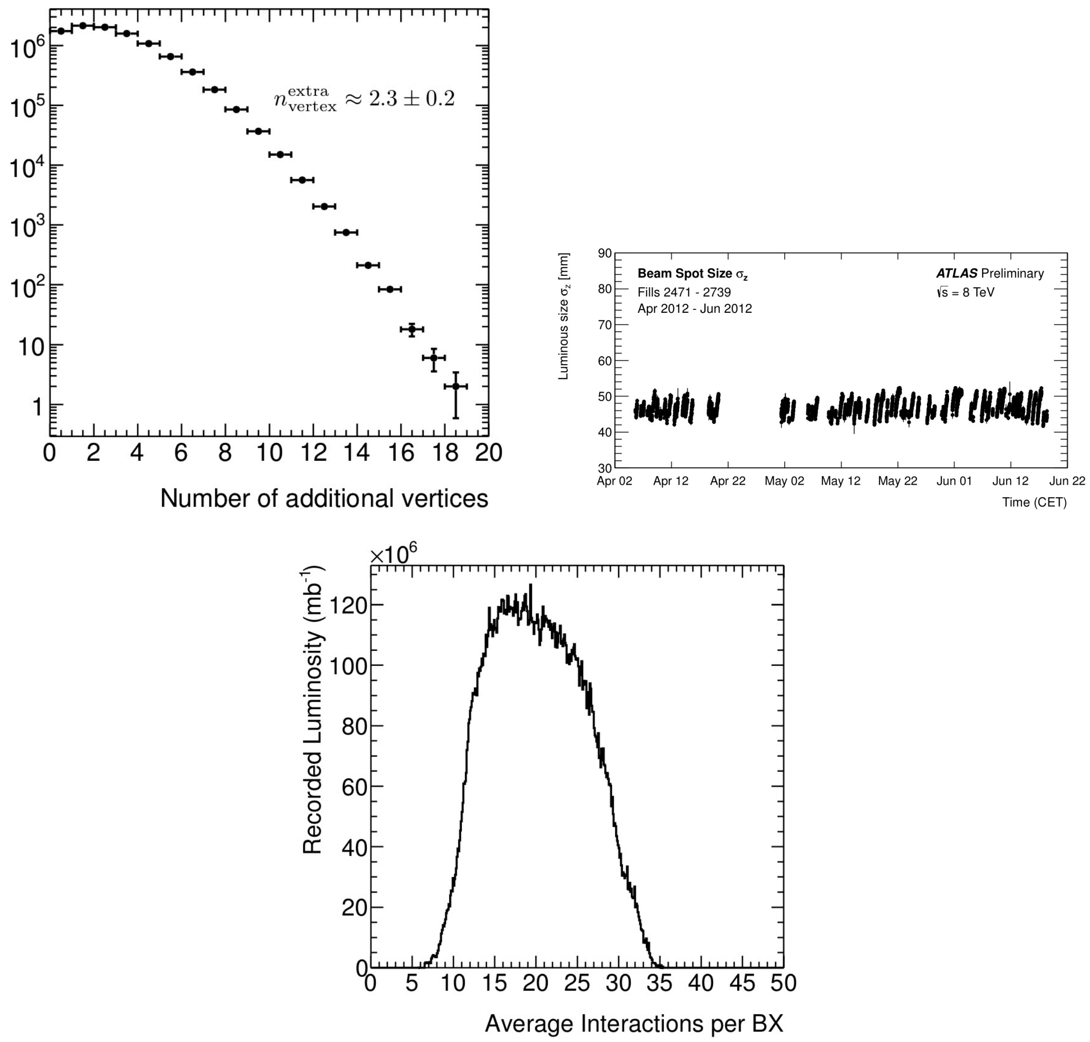

Figure B.4: Plots used to estimate the number of additional pileup verticies. Distibution of additional vertices within 10 mm of the W vertex. Size in z of the luminous region in ATLAS over the course of pp running in 2012 at $\sqrt{s} = 8$ TeV. The data points are the result of a maximum likelihood fit to the spatial distribution of primary vertices collected over ten minutes. Errors are statistical only. The distribution of the average interactions per bunch crossing.[54]

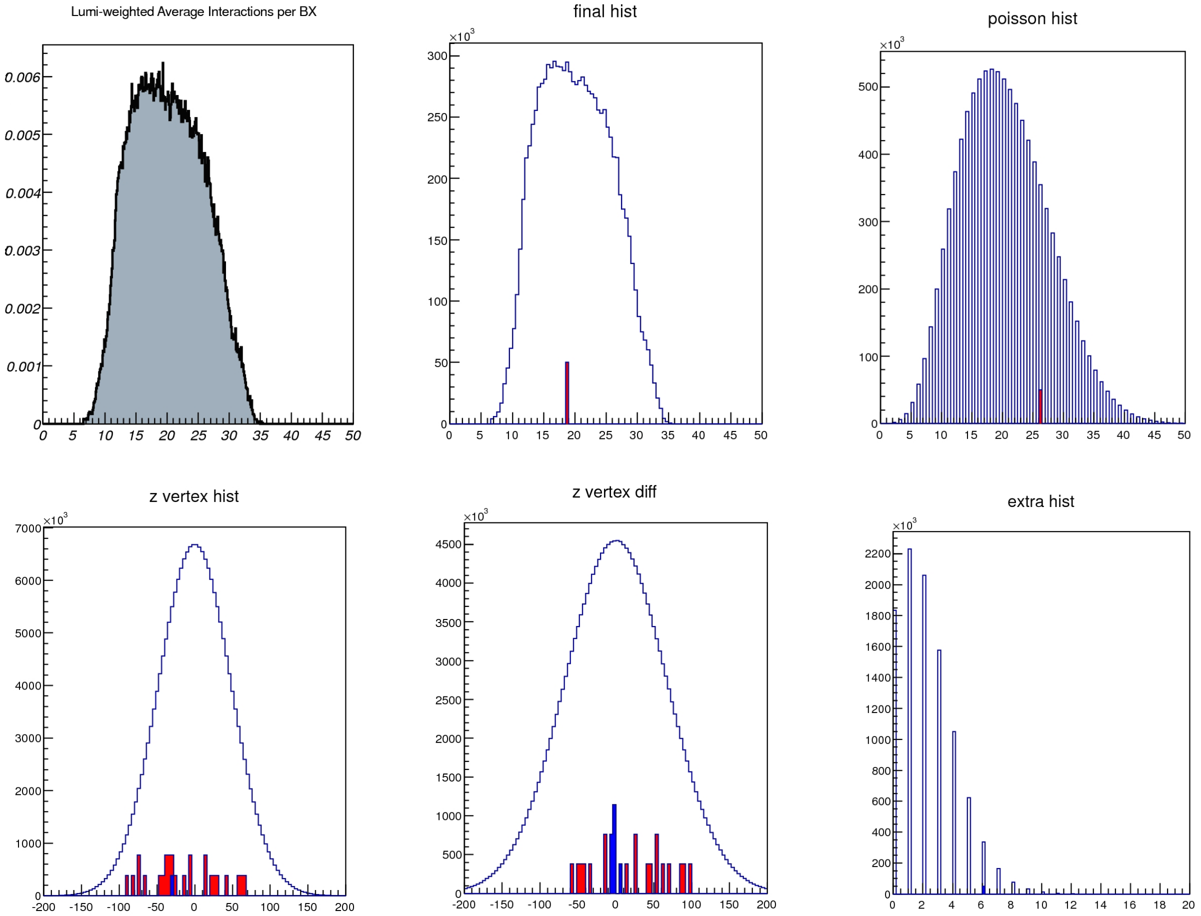

Figure B.5: MC strategy schematic for the estimation of extra pileup vertices, the proceedure follows these steps: Take the luminosity weighted mean number of collisions per bunch crossing from 2012 data. Sample the distribution many times to obtain individual $< \mu >$ values. For each time, sample a Poisson distribution with mean $< \mu >$ to give the number of vertices for this event, N$_{vtx}$. Distribute N$_{vtx}$ in z with Gaussian width given by beam spread $\sigma_z \approx 48 \pm 3$ mm. Select one vertex at random to be the primary vertex and count how many other vertices fall within 10mm of it. The average number of extra vertices within 10 mm of the randomly chosen one, $n^{\text{extra}}_{\text{vertex}} \approx 2.3 \pm 0.2$. [54]

$J/\psi_{(p_T)}$	$0.00 < J/\psi_y < 0.25$	$0.25 < J/\psi_y < 0.50$	$0.50 < J/\psi_y < 0.75$
110-150	$(1.89 \pm 1.95) \times 10^{-9}$	$(2.34 \pm 2.65) \times 10^{-9}$	$(3.17 \pm 3.00) \times 10^{-9}$
	$0.75 < J/\psi_y < 1.00$	$1.00 < J/\psi_y < 1.25$	$1.25 < J/\psi_y < 1.50$
8.5-9.0	(2.11 ± 0.07)	(2.26 ± 0.08)	(2.20 ± 0.17)
9.0-9.5	(1.66 ± 0.05)	(1.77 ± 0.05)	(1.71 ± 0.09)
9.5-10.0	(1.31 ± 0.03)	(1.39 ± 0.03)	(1.33 ± 0.04)
110-150	$(1.73 \pm 1.00) \times 10^{-9}$	$(1.53 \pm 1.08) \times 10^{-9}$	$(1.50 \pm 2.13) \times 10^{-9}$
	$1.50 < J/\psi_y < 1.75$	$1.75 < J/\psi_y < 2.00$	$2.00 < J/\psi_y < 2.10$
8.5-9.0	(2.05 ± 0.04)	(2.28 ± 0.05)	(1.09 ± 0.042)
9.0-9.5	(1.62 ± 0.03)	(1.75 ± 0.03)	(0.85 ± 0.024)
9.5-10.0	(1.28 ± 0.02)	(1.35 ± 0.02)	(0.665 ± 0.013)
110-150	$(3.54 \pm 1.41) \times 10^{-10}$	$(6.32 \pm 2.19) \times 10^{-10}$	$(1.16 \pm 1.13) \times 10^{-9}$

Table B.2: Extrapolated $J/\psi \to \mu^+\mu^-$ cross-section values using a triple exponential fit.

$J/\psi_(p_T)$	$2.00 < J/\psi_y < 2.10$
10.0 - 10.5	(0.941 ± 0.039)
10.5 - 11.0	(0.734 ± 0.029)
11.0 - 11.5	(0.576 ± 0.023)
11.5 - 12.0	(0.455 ± 0.018)
12.0 - 12.5	(0.362 ± 0.014)
12.5 - 13.0	(0.290 ± 0.012)
13.0 - 14.0	(0.212 ± 0.008)
14.0 - 15.0	(0.142 ± 0.006)
15.0 - 16.0	(0.0971 ± 0.0040)
16.0 - 17.0	(0.0678 ± 0.0028)
17.0 - 18.0	(0.0481 ± 0.0020)
18.0 - 20.0	(0.0303 ± 0.0013)
20.0 - 22.0	(0.0170 ± 0.0007)
22.0 - 24.0	(0.0104 ± 0.0005)
24.0 - 26.0	(0.00658 ± 0.00030)
26.0 - 30.0	(0.00361 ± 0.000170)
30.0 - 35.0	(0.00169 ± 0.00008)
35.0 - 40.0	(0.000794 ± 0.000041)
40.0 - 60.0	(0.000230 ± 0.000014)
60.0 - 110.0	$(0.0000157 \pm 0.0000150)$

Table B.3: Extrapolated $J/\psi \to \mu^+\mu^-$ cross-section values determined by taking 10% of the $0.00 < J/\psi_y < 2.00$ value.

Appendix C

Additional Event Displays

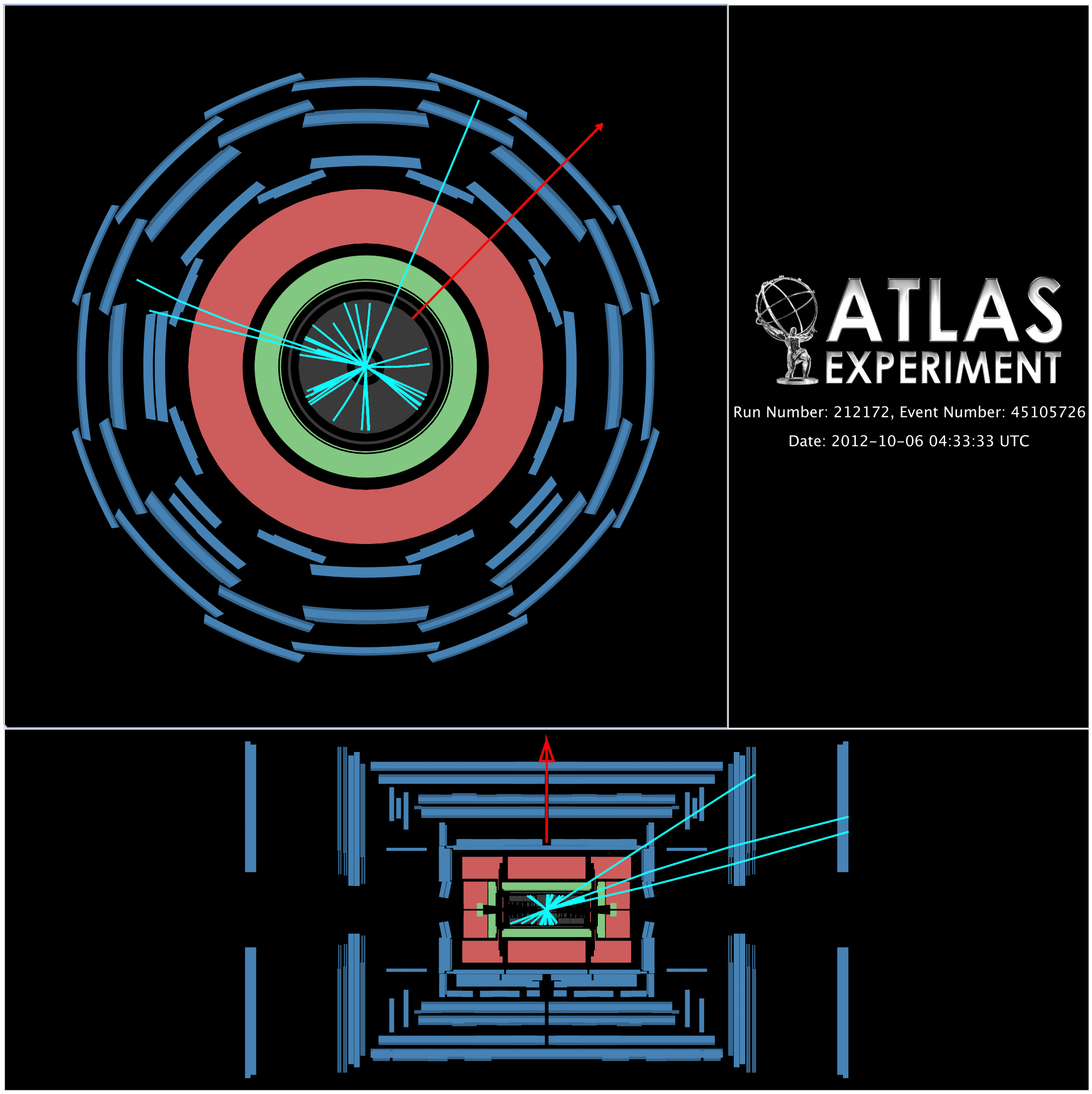

Figure C.1: A representative $pp \to J/\psi + W^{\pm} \to \mu^{+}\mu^{-}, \mu^{\pm}\nu$ candidate event recorded with the ATLAS detector at $\sqrt{s} = 8$ TeV during data taking in 2012. The muon tracks are shown with solid blue lines and the missing transverse energy vector is shown with a red arrow.

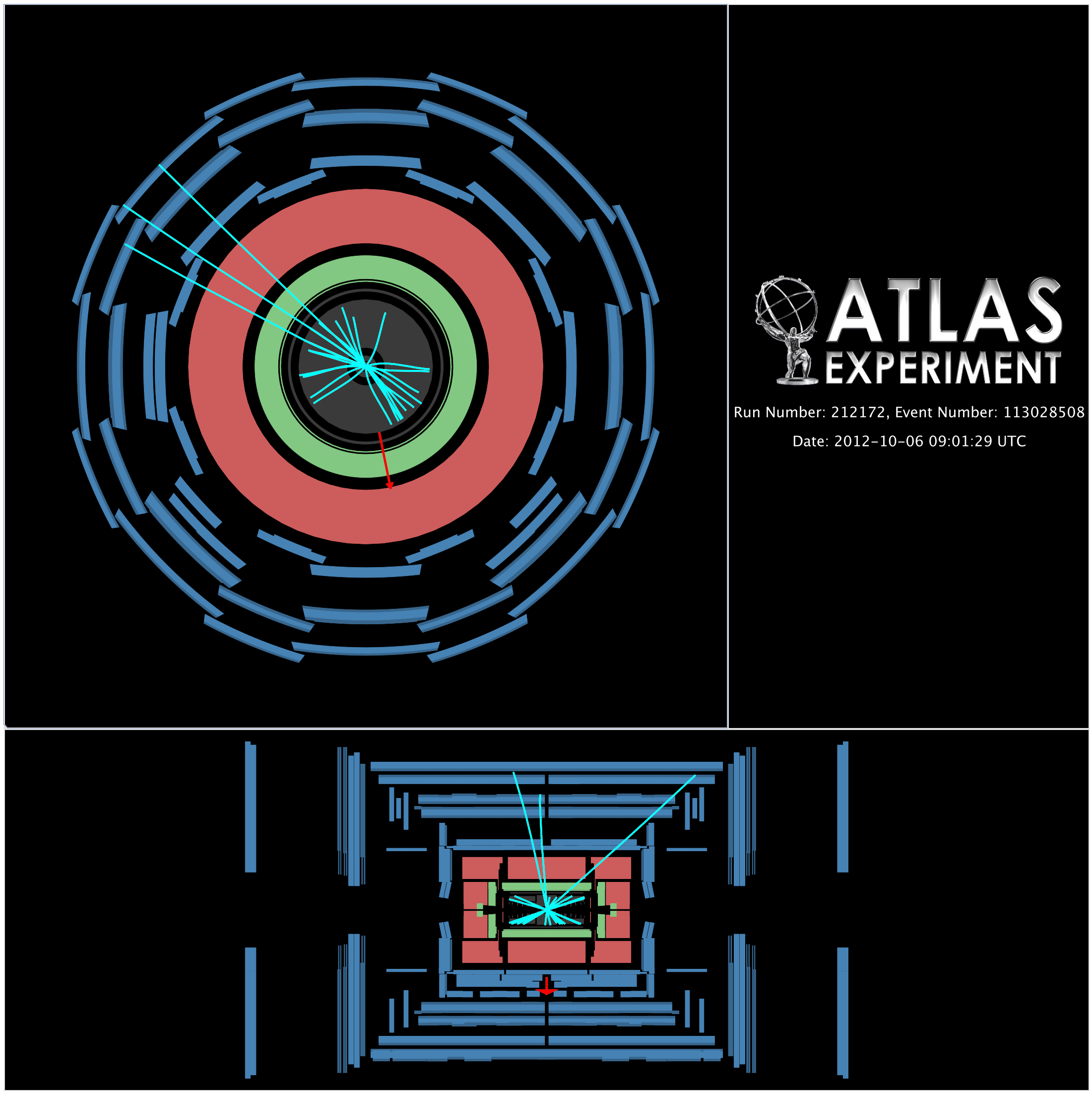

Figure C.2: A representative $pp \to J/\psi + W^{\pm} \to \mu^{+}\mu^{-}, \mu^{\pm}\nu$ candidate event recorded with the ATLAS detector at $\sqrt{s} = 8$ TeV during data taking in 2012. The muon tracks are shown with solid blue lines and the missing transverse energy vector is shown with a red arrow.

Appendix D

J/ψ Mass and Lifetime Fit Model Details

D.1 Nominal fits

The nominal fit for the prompt and non-prompt J/ψ mass peaks is a single gaussian and for their backgrounds it is a second order polynomial. To determine the best mass peak width we need a sample of $J/\psi + W^{\pm}$ orthogonal to the signal dataset, but with high enough statistics. So a dataset of J/ψ plus low quality $W^{\pm}$ candidates was created. This sample is fit to a floating J/ψ mass peak and a $\psi(2S)$ mass peak fixed to the PDG value of 3.68 GeV [9]. The prompt J/ψ mass peak mean and width derived from this method are then applied to the $J/\psi + W^{\pm}$ signal sample to determine the nominal prompt J/ψ yield.

The fit model used for the prompt J/ψ lifetime is a single gaussian and for its background it is a double gaussian. For the non-prompt J/ψ lifetime and its background a single gaussian convoluted with a single sided exponential is used.

D.2 Alternate fits for systematics

Three alternate J/ψ mass fit methods are used one at a time to obtain different prompt J/ψ yield numbers that determined a systematic uncertainty on the measurement. The first method is to introduce the $\psi(2S)$ mass peak into fit model as a third background with the mean value fixed to the PDG value of 3.68 GeV and the width equal to $\frac{M_{\psi(2S)}}{M_{J/\psi}} \times \mathrm{width}_{J/\psi}$. The second method is to let the J/ψ mass peak mean and width float. The third method is to use exponential functions for the J/ψ mass backgrounds.

Appendix E

Cross Checks

Many sanity checks are performed at various points during the analysis. The checks that don't fit neatly into other chapters are collected here.

E.1 Signal contamination of MC backgroud samples

The MC background samples for the $J/\psi, W^{\pm} \to \mu^{+}\mu^{-}, \mu^{\pm}\nu$ are processed in the same way the data is processed, and the prompt component is separated out. We do not expect to see any signal in these background MC samples, and indeed the prompt signal seen in Figure E.1 is consistent with zero.

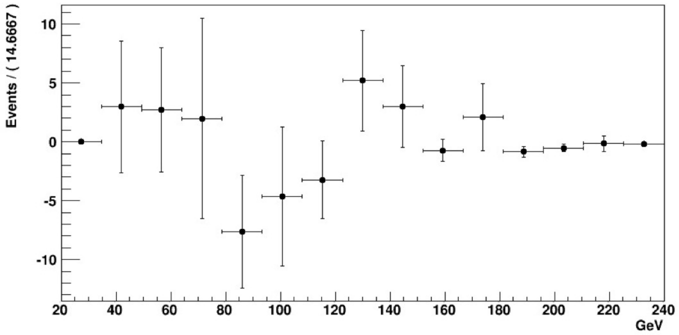

Figure E.1: $m_{\mathrm{T}}(W)$ in prompt MC backgrounds is consistent with zero.

E.2 Signal yield extraction

In figure E.2 we include the pull distributions for the four components of the fit. The result of the signal yield value is shown to be unbiased.

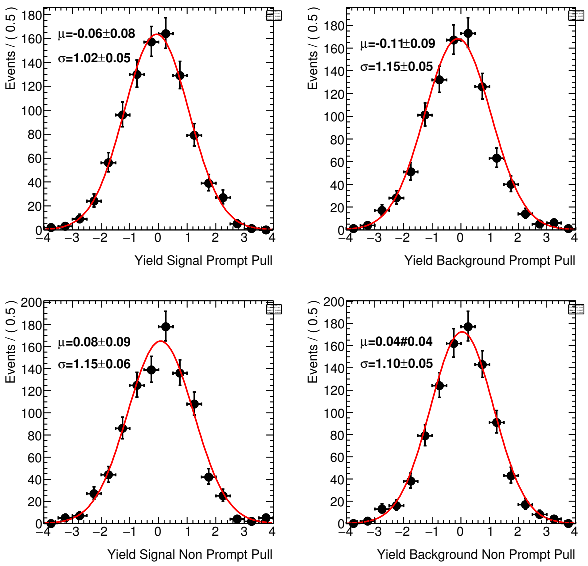

Figure E.2: Pull distributions for the four yield components of the fit.

E.3 $W^{\pm}$ cut efficiency

The cross-section ratio calculations in Equations 4.18 and 4.16 depend on the efficiency of the $W^{\pm}$ cuts being the same for the associated $J/\psi + W^{\pm}$ and Inclusive $W^{\pm}$ samples. A test is performed with MC samples that compares the fraction of $W^{\pm}$ candidates that are vetoed by each cut. The results are seen in Table E.1, showing that the efficiency is the same.

E.4 sPlot performance with associated signal MC samples

The associated prompt and non-prompt signal MC samples (listed in Tables 4.2 and 4.3) were processed in the same way as data. These samples are used to test if sPlot can accurately separate prompt and non-prompt J/ψ events. An MC sample with

Muon cut	$J/\psi + W^{\pm}$ fraction	Inclusive $W^{\pm}$ fraction
Initial	1.000	1.000
Trigger Match	0.875	0.871
muon ID	0.872	0.869
STACO	0.860	0.856
MCP	0.850	0.846
p_{T}	0.805	0.805
η	0.789	0.790
Primary Vertex	0.787	0.775
IP significance	0.784	0.771
E_{T} Cone 30	0.598	0.615
p_{T} Cone 30	0.598	0.615
MET	0.540	0.554
$m_{\mathrm{T}}(W)$	0.529	0.521

Table E.1: Cutflow fraction comparison for $W^{\pm}$ candidates in the $J/\psi + W^{\pm}$ sample and in the inclusive $W^{\pm}$ sample.

a known prompt to non-prompt ratio of 0.547 is processed with sPlot and returns a prompt to non-prompt ratio of 0.549±0.008. So we conclude that the results returned when using this method to separate data events are reliable.

E.5 Kinematic check of MC signal sample

We verify that the kinematics of the $W^{\pm}$ bosons in the associated $J/\psi + W^{\pm}$ MC sample is consistent with the kinematics of the $W^{\pm}$ bosons in the inclusive $W^{\pm}$ MC sample. Figures E.3 and E.4 show that the mean values and standard deviations of the $W^{\pm}$ boson transverse masses are consistent between the two samples.

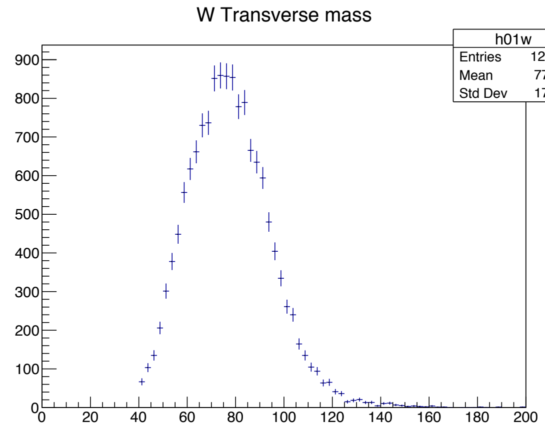

Figure E.3: $W^{\pm}$ boson transverse mass in the associated $J/\psi + W^{\pm}$ MC sample.

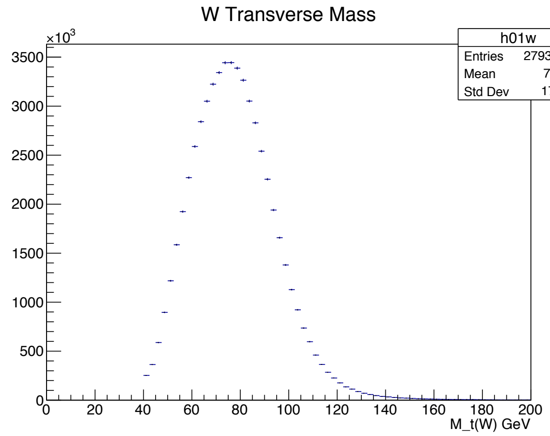

Figure E.4: $W^{\pm}$ boson transverse mass in the inclusive $W^{\pm}$ MC sample.